Alma Mater Studiorum · University of Bologna

School of Science
Department of Physics and Astronomy
Master Degree in Physics

Reconstruction of hadronic showers in the SND@LHC experiment

Supervisor:
Prof. Luigi Guiducci

Submitted by:
Alex Ferrara

Co-supervisor:
Dr. Gaetano Marco Dallavalle
Giulia Paggi
Filippo Mei

Academic Year 2023/2024

Abstract

This thesis is about the SND@LHC experiment, a compact, standalone detector located in the TI18 tunnel (480 m downstream of the ATLAS interaction point).
The experiment is designed to detect and identify neutrinos of all three flavors, produced in LHC proton-proton collisions in the pseudorapidity region $7.2 < \eta < 8.4$, and to study, for the first time in laboratory, neutrino interactions in the energy range between 300 GeV and 1 TeV.
In this thesis, I focused on studying the reconstruction of hadronic showers using test beam data to evaluate the accuracy and sensitivity achievable by the experiment in locating hadronic showers. The method achieved an angular resolution of approximately 30 mRad. The reconstruction of hadronic shower directions is relevant for determining the energy of the incoming neutrino.
All analyses were carried out using C++ code developed specifically for this purpose.

Contents

Introduction

Neutrinos are among the most intriguing particles in the Standard Model of particle physics. On one hand, as part of the Standard Model, they provide unique insights into fundamental physics. On the other hand their non-zero mass points to physics beyond the Standard Model.

The SND@LHC experiment is a compact, standalone experiment located in the TI18 tunnel (480 m downstream of the ATLAS interaction point). It allows for the identification of all three flavors of neutrino produced in LHC proton-proton collisions. It aims to explore neutrino interactions in an energy range between 300 GeV and 1 TeV, which has not been studied before in a laboratory.

The SND@LHC detector consists of three main components: a veto system, to exclude charged particles entering the detector; a neutrino target with tracking capability, with a mass of about 830 Kg; and a hadron calorimeter and a muon tracker. The target is composed by walls of tungsten and nuclear emulsions, interleaved with Scintillating Fibers tracking modules.

In Chapter 1, I discuss various aspects of neutrinos, from their discovery to their implications in physics beyond the Standard Model.

In Chapter 2, I describe the SND@LHC detector, detailing its components and their respective functions. Special attention is given to the test beam, which was used to calibrate the measurement of hadronic energy and determine uncertainties and resolutions.

Finally, in Chapter 3, I present my work. This focuses on the study of hadronic showers, using test beam data, for developing a method to determine their positions and directions.

Chapter 1

Neutrino Physics

1.1 Neutrino experimental observation

Although the existence of neutrinos was postulated in the '30s [1], to explain the electron emission spectrum in beta decays, they were experimentally observed much later, in 1956, at the Savannah River nuclear reactor. The experiment, led by Reines and Cowan [2], aimed to verify the inverse β-decay:

$$\bar{\nu_e} + p \rightarrow n + e^+$$

The decision to conduct the experiment near a nuclear reactor, which provided a huge

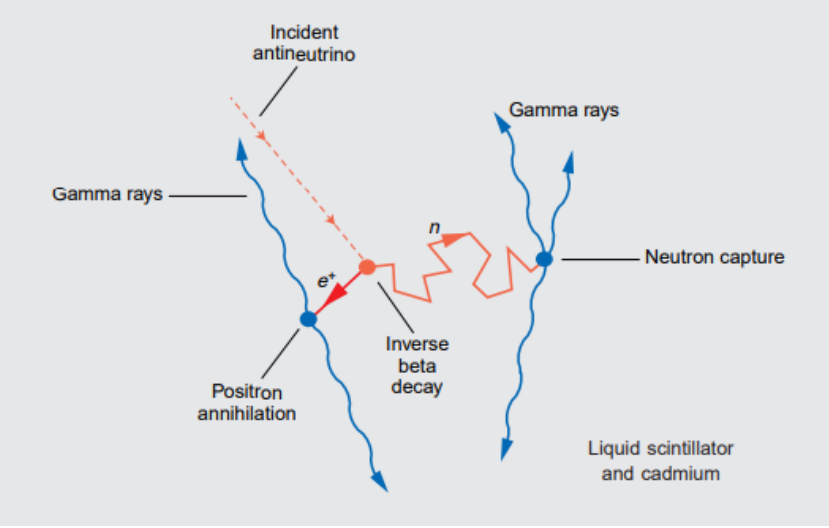

Figure 1.1: Double signature of inverse β-decay.

flux of anti-neutrinos $\Phi \simeq 10^{13}$ cm^{-2}s^{-1}, was relevant to overcome the extremely low cross-section of the process $\sigma \simeq 10^{-38}$ cm^2 [2].

The experimental setup consisted of a water tank, covered by photomultiplier tubes, and filled with a liquid scintillator enriched with Cadmium. The antineutrino interaction process is schematically represented in Figure 1.1. When an antineutrino interacts, the emitted positron annihilates with an electron, typically within a few ns, leading to the emission of two photons traveling in opposite directions. Simultaneously, the neutron undergoes multiple scatterings, following a random path until it becomes thermalized and is subsequently captured by a Cadmium nucleus. Then the Cadmium nucleus de-excites by emitting 9 MeV as gamma rays. The entire neutron capture process needs a few μs to complete.

The key aspect of this experiment is the time delay of a few μs between the two flashes of light, which are collected by the photomultiplier tubes that convert the photons into electric signals. The pulses from all the tubes are combined, counted, processed, and

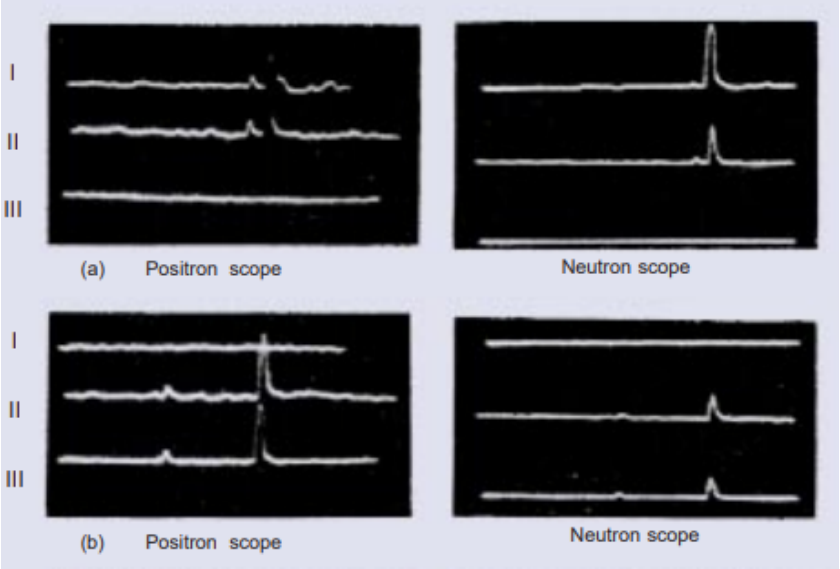

Figure 1.2: Oscilloscope traces from the Savannah River Experiments.

displayed on an oscilloscope screen, as shown in Figure 1.2, where positron and neutron delayed-coincidence signals can be seen [2]. This sequence of two flashes of light, separated by a few microseconds, is the double signature of inverse β decay confirming the existence of neutrinos.

1.2 Neutrino Helicity

In 1958, Goldhaber studied the helicity of neutrinos through measurements on the decay of Europium (J=0), as shown in Figure 1.3, in a two-step process [3]: the first step

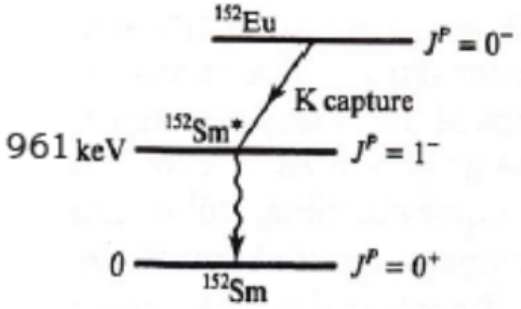

Figure 1.3: Schematic representation of Europium decay. The first step is the electron capture leading to an excited Samarium, the second step is the de-excitation of Samarium.

involves orbital electron capture

$$^{152}\mathrm{Eu} + e^- \rightarrow \ ^{152}\mathrm{Sm}^* + \nu_e$$

which leads to an excited state of Samarium (J=1) and the emission of a neutrino with an energy of 840 keV. The second step is the de-excitation of Samarium via an electric dipole (E1) γ-ray transition:

$$^{152}\mathrm{Sm}^* \rightarrow \ ^{152}\mathrm{Sm} + \gamma$$

emitting a photon of 961 keV, in this way the Samarium goes to the ground state. Requiring the conservation of angular momentum in the first reaction, the excited Samarium and the neutrino must have the same helicity:

$$h(\mathrm{Sm}^*) = h(\nu_e) \ . \tag{1.2.1}$$

In the second step, the helicity of γ-rays is studied through their circular polarization. A ring of Samarium resonantly scatters these photons, and the ones emitted along the recoil direction of the excited Samarium must have the same helicity as the Samarium:

$$h(\gamma) = h(\mathrm{Sm}^*) \ . \tag{1.2.2}$$

Combining the constraints from Equations (1.2.1) and (1.2.2), measuring the helicity of photons allow for a direct measurement of neutrino helicity [4].

Figure 1.4 shows the experimental setup used to measure the helicity of the photons. The Eu source was inserted inside an electromagnet, which was alternately magnetized in the upward or downward direction to select photons with either positive or negative helicity. Depending on their helicity, the photons interact differently via Compton scattering with the electrons contained in the magnetized iron.

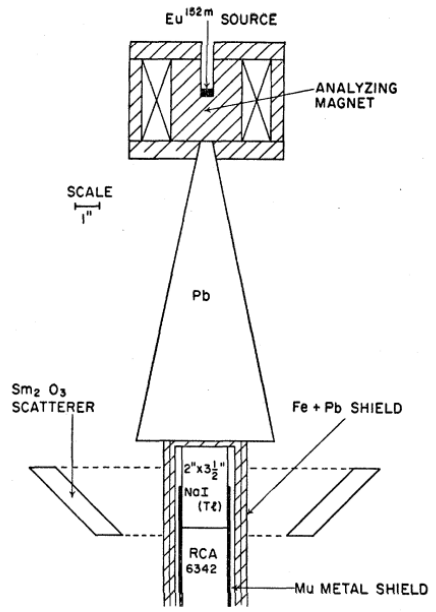

Figure 1.4: Experimental setup for studying the circular polarization of resonant scattered γ rays.

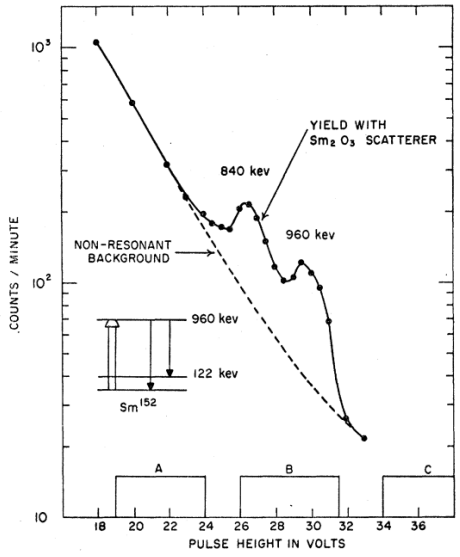

Figure 1.5: Results of Goldhaber experiments that confirm that neutrinos are left-handed. It shows the resonant scattered γ rays of Eu^{152}.

By the recoil of ^{152}Sm nuclei promptly emitted either a 960 keV or a 840 keV gamma ray; the latter emission was not significant to the experimental outcomes. The 960 keV

gamma rays emitted in the direction of stable ^{152}Sm nuclei experienced a Doppler shift, with the degree of this shift dependent on the emission angle of the associated neutrino. For neutrinos emitted away from the ^{152}Sm target, the Doppler shift of the 960 keV gamma ray was positive, leading to an increase in the observed energy. Experimental measurements showed a higher transmission rate when the photon spin was aligned with the electron spin, which was opposite to the direction of the applied magnetic field (B-field). The design incorporated a resonant ring that selectively allowed photons emitted along the recoil trajectory of the excited samarium nuclei to pass through.
As illustrated in Figure 1.5, peaks in transmission were observed when the B-field was oriented downward, favoring the transmission of left-handed photons. This observation strongly supports the conclusion that neutrinos are left-handed, as it aligns with the maximal transmission configuration for left-handed photon interactions.

1.3 Parity violation

CP symmetry refers to the simultaneous application of Charge conjugation (C), which transforms a particle into its antiparticle, and Parity (P), which involves flipping the spatial coordinates (i.e., the direction of motion). To illustrate this, Figure 1.6 shows an example of CP symmetry application [4]. When only P is applied, the particle's direction is reversed, but its spin remains unchanged, obtaining a right-handed neutrino. When only C is applied, the particle becomes its antiparticle, producing a left-handed antineutrino. When both C and P are applied (CP symmetry), the result is a right-handed antineutrino. In the second half of the 20th century it was well established that

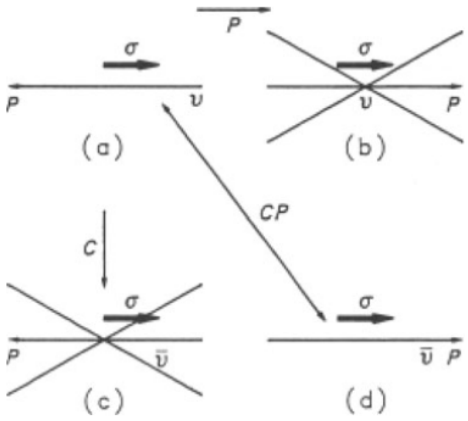

Figure 1.6: Example of application of CP symmetry. Up to now only (a) and (d) states have been observed.

weak interactions violate both Parity and Charge conjugation. One of the most known

experiments, happened in 1956, was the one led by Madame Wu [4], this experiment had the aim to demonstrate the Parity violation in beta decays. The experiment studied the β^- decay of ^{60}Co,

$$^{60}Co \rightarrow \ ^{60}Ni^* + e^- + \bar{\nu}_e$$

This process is a pure Gamow-Teller transition, where the angular momentum changes from 5^+ in Cobalt to 4^+ in Nickel. The excited Nickel then de-excites through photon emission:

$$^{60}Ni^* \rightarrow \ ^{60}Ni + \gamma \ .$$

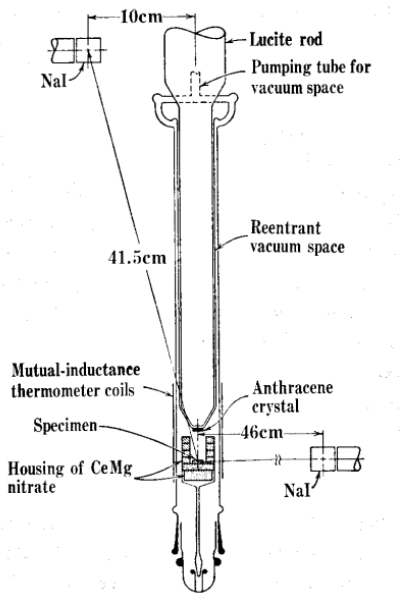

Figure 1.7: Schematic diagram showing the demagnetization cryostat used to polarize the ^{60}Co.

The key feature of the experiment was to polarize the Cobalt nuclei to align their spins in the same direction. To achieve this, a magnetic field $B = 1.2$ T and a cryostat, cooling the sample to 0.01 K, were used. In addition, adiabatic cooling with an orthogonal magnetic field and a paramagnetic salt (Cerium-Magnesium Nitrate) was employed to further reduce the temperature to 3 mK. The experimental apparatus is shown in Figure 1.7. Two photon detectors were used, one along the cryostat axis and another perpendicular to it. An e^- detector along the axis measured electron polarization. The experiment revealed that the emission was not isotropic, as shown in Figure 1.8. The splitting observed in the curves is attributed to the anisotropy of the γ emissions, which disappears as the magnetization vanishes. In contrast, the detection of β particles reflects parity

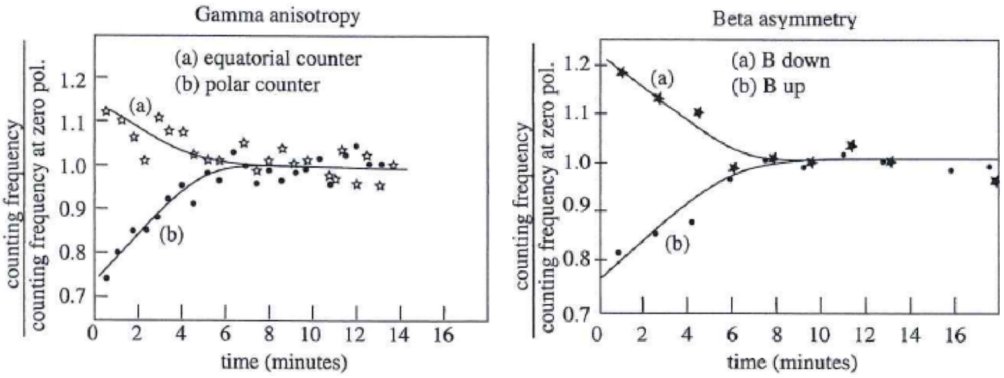

Figure 1.8: Results of the experiment of Madam Wu, showing in the left the counts of photons and in the other the counts of photons with respect to the one of Cobalt.

violation. The observed β asymmetry doesn't change sign with changing the direction of the demagnetization field, indicating that it is not caused by the remanent magnetization in the sample. The asymmetry coefficient sign is negative, thus the emission of β particles is more favored in the direction opposite to that of the nuclear spin [4].

1.4 Neutrino flavors

In the late '50s, begin '60s, an open question in particle physics was whether neutrinos appearing in β decays were the same type as those appearing in muon and pion decays. If they were the same, one might expect to observe the electromagnetic decay of muons via the process:

$$\mu^{\pm} \rightarrow e^{\pm} + \gamma$$

and the expected Branching Ratio for this process would be around $\simeq 10^{-5}$, while the measured value amounted to $< 6 \times 10^{-13}$ [5]. In 1962, at the Brookhaven laboratory's Alternating Gradient Synchrotron (AGS), Schwarz Lederman and Steinberg observed a new type of neutrino. They studied the interactions of neutrinos produced from pion and kaon decays, which were created in proton-beryllium collisions. Since these decays produced muons, they were used as a source of neutrinos.

The idea behind the experiment was simple: if only one flavor of neutrinos existed, then equal amounts of muons and electrons would be produced in charged lepton formation processes. However, if different flavors of neutrinos existed, an excess of muons should be observed, according to the reaction:

$$\nu_{\mu} + N \rightarrow \mu^{-} + X \ .$$

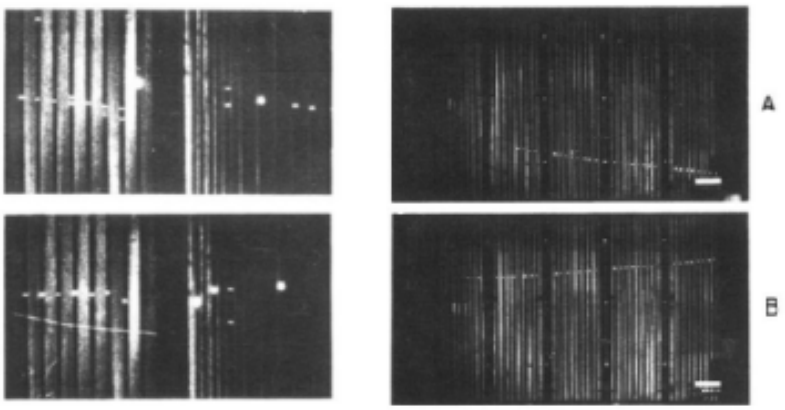

Figure 1.9: Tracks made in the sparks chambers in Schwarz, Lederman and Steinberg experiment. On the left there are electromagnetic showers generated by an electron, on the right there are deep penetrating tracks, ascribable to muon.

To detect neutrino interactions, a 10−ton aluminum spark chamber made of 90 planes was used. The chamber was located 21 m behind the beryllium target and shielded by a 13.5 m steel wall to stop all secondary particles except neutrinos [6]. Figure 1.9 shows the results: on the left, an electromagnetic shower produced by an electron is seen, while on the right, a long penetrating track, produced by a muon, is visible.

The experiment recorded 34 muon events and only 6 electron showers, confirming the existence of distinct neutrino flavors [7].

In 1975, the discovery of the third charged lepton, the τ, led to the hypothesis of the existence of a third neutrino flavor. This was confirmed in 2000 by the DONUT and OPERA experiments, which directly observed charged current interactions of tau neutrinos. The key challenge was identifying the τ lepton, which has a decay length of only few mm.
Both experiments used nuclear emulsions to detect tau neutrinos. Charged particles leave a track in the layers of emulsion, allowing to reconstruct their direction.

In the DONUT setup τ neutrinos were produced by colliding 800 GeV protons from Fermilab with a tungsten target, producing D_S mesons, which decay into τ and $\bar{\nu_\tau}$ [8], as shown in Figure 1.10. After interacting with the tungsten, the decay products passed through a magnet and thick shielding layers made of concrete, iron and lead, in order to filter out all particles except the neutrinos. The data analysis reconstructed the interaction vertex and identified the tau lepton's decay. Only four events were ultimately selected, with a probability of these being background noise at 4×10^{-4}. This confirmed the existence of τ neutrino charged current interactions [8]. The observed tau decays

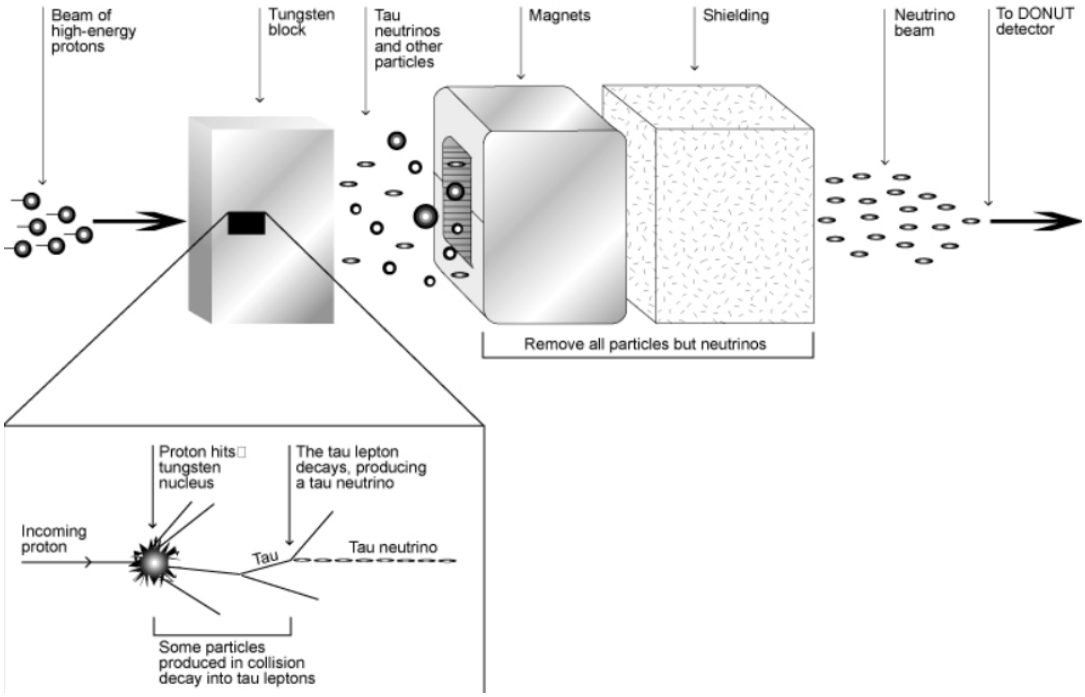

Figure 1.10: Schematic representation of ν_τ formation, from proton beam against tungsten and the selection of neutrino beams by magnets and a thick shielding layer.

followed two processes:

$$\tau \to h + \nu_\tau + X \tag{1.4.1}$$

$$\tau \to e + \nu_\tau + \nu_e \tag{1.4.2}$$

The events are shown in Figure 1.11, where the first and fourth images depict tau decays into electrons (process 1.4.2), and the second and third show tau decays into hadrons (process 1.4.1).

On the other side OPERA, located in Gran Sasso Laboratories, used neutrinos beams sent directly from CERN, 732 km away, with an energy of 17 GeV [9]. Tau neutrinos in the beam were expected due to neutrino flavor oscillations (see Section 1.8). OPERA observed 10 events ascribable to the production of a τ with a statistical significance of 6.1σ. In Figure 1.12 is reported the decay of a τ, the vertex in which the neutrino interacts is in the left of the image, the short line numbered as 4 (in red) is the trace of the lepton, that decays in a charged pion, (the number 8 trace, the sky-blue one) and a neutral pion, whose trace is given by the two photons γ_1 and γ_2 in which it decayed

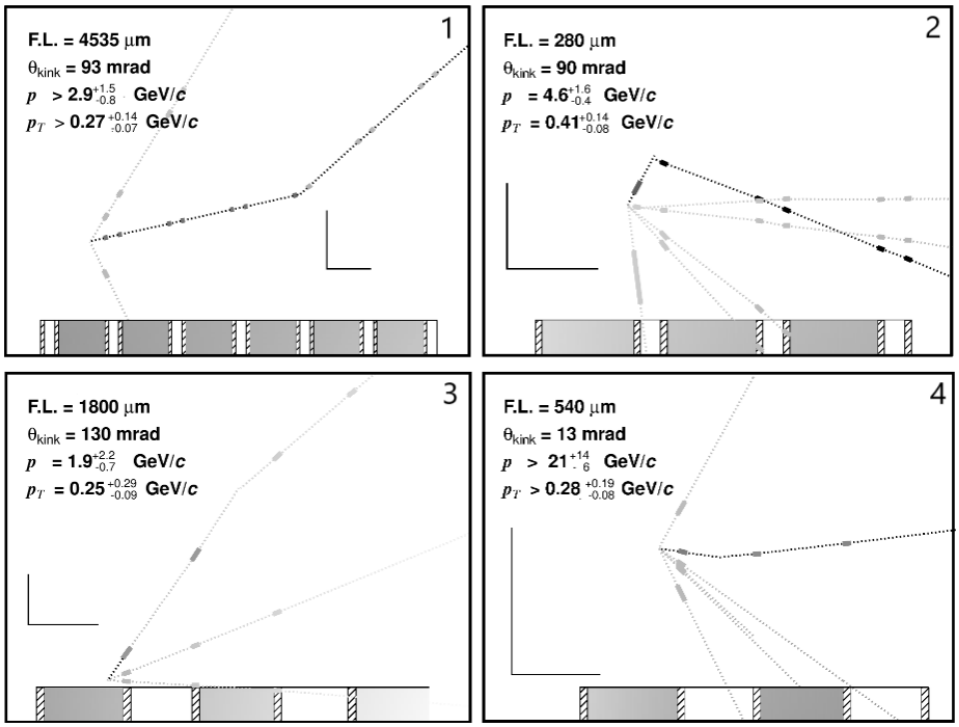

Figure 1.11: ν_τ charged current interactions. The first and fourth images show τ lepton decays into an electron (process 1.4.2), while the second and third show τ decays into hadrons (process 1.4.1).

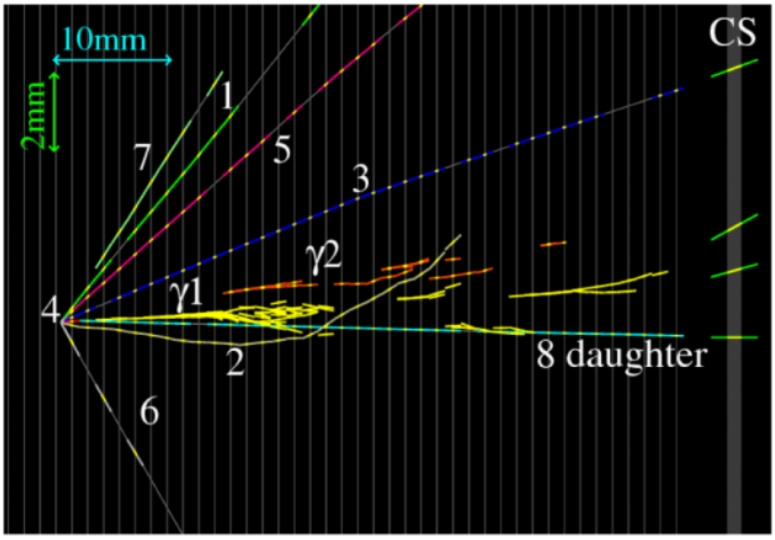

Figure 1.12: Reconstruction of a τ decay in the OPERA experiment.

shortly after, visible as showers in yellow and in orange.
As reported in Figure 1.13, OPERA was made by two modules, each one was composed of 75000 bricks of lead distributed along 27 walls, each one was covered with photographic films (nuclear emulsion), thick 300 μm. In the void space between two walls there are plastic scintillators both in vertical and horizontal directions 200 μm thick.

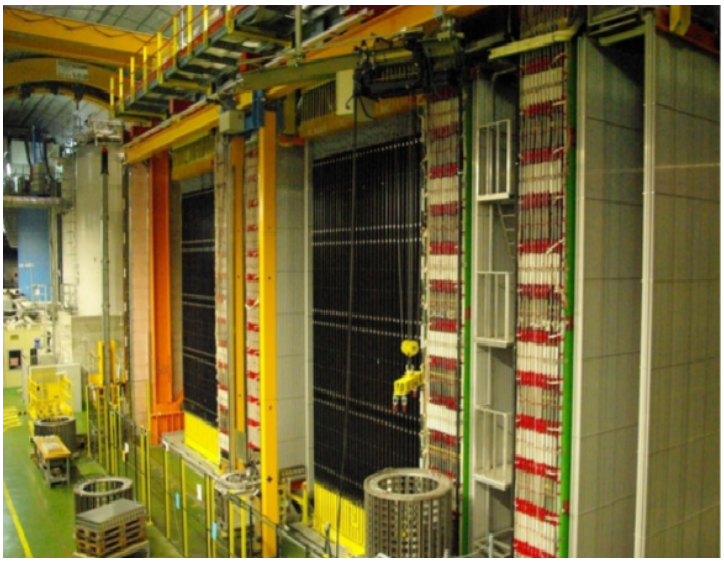

Figure 1.13: OPERA experiment in Gran Sasso Laboratories, it can be seen the two modules of the experiments, made by 27 walls, composed by 75000 bricks of lead covered by photographic films.

1.5 Fermi's theory

In 1934, Fermi proposed a theory to explain β decay processes, by modeling them as current-current interaction taking as reference the structure of Quantum Electrodynamics (QED), but with additional hypotheses [10]. The process is described as a point-like interaction between particles, where vector-like currents can change the nature of the particles involved, as shown in Figure 1.14.
The currents involved in beta decay, as shown in Figure 1.14, are:

$$J_\mu(p) = (\bar{u}_p \gamma_\mu u_n) \quad \text{and} \quad J_\mu(e) = (\bar{u}_e \gamma_\mu u_\nu) \ .$$

These give rise to the matrix element:

$$M_{fi} \approx G_F \cdot (\bar{u}_p \gamma^\mu u_n)(\bar{u}_e \gamma_\mu u_\nu \ .) \tag{1.5.1}$$

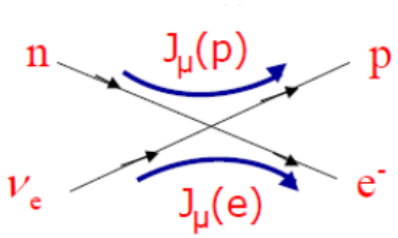

Figure 1.14: Feynman diagram representing the process $\nu + n \rightarrow p + e^-$.

G_F is called Fermi coupling constant and has a value of $\simeq 1.166 \times 10^{-5}$ GeV^{-2}. Fermi's theory was remarkably successful in predicting with good precision various experimental observables, such as decay rates and mean lifetimes, using Fermi's Golden Rule (Equation (1.5.2)), which calculates the transition probability from an initial state to a final state:

$$W = \frac{2\pi}{\hbar}|M_{fi}|^2 \frac{dN}{dE_0} \ . \tag{1.5.2}$$

Here, the matrix element $|M_{fi}|$ is calculated as seen above (Equation (1.5.1)), while $\rho_f = dN/dE_0$ is the phase-space factor representing the density of available finale states at a given energy.

Despite its success, we now know that Fermi's theory is an effective theory, valid up to an energy scale of approximately ~ 100 GeV [10]. Above this energy, the theory breaks down, as it does not account for the involvement of the $W^\pm$ or Z^0 bosons, which have high masses of 80 and 91 GeV, respectively.

Fermi's theory is, therefore, understood as an approximation of the weak interaction at low energies. In the '50s, experimental evidence showed that weak processes violate parity symmetry, leading to an extension of Fermi's theory. The revised theory incorporated not only vector currents (V, associated to an operator γ^μ) but also axial-vector currents (A, associated to an operator $\gamma^\mu\gamma^5$). The Lagrangian function had a V-A structure:

$$\mathcal{L}_{WEAK} = -\frac{G_F}{\sqrt{2}}(\bar{n}\gamma^\mu(1-\gamma^5)p)(\bar{\nu_e}\gamma_\mu(1-\gamma^5)e) \ . \tag{1.5.3}$$

This Lagrangian (1.5.3) is a first step towards the development of the Standard Model. Although it still has limitations, such as being non-renormalizable, it accurately describes all weak interaction processes at low energies. Further refinements were necessary to incorporate the W and Z bosons and address renormalization issues, leading to the full formulation of the electroweak theory within the nowadays well established Standard Model framework.

1.6 Neutrinos in the Standard Model

In the '60s, the Glashow-Weinberg-Salam (GWS) model was developed to describe weak interactions as a gauge theory. Together with Quantum Chromodynamics (QCD), which governs the strong interaction, forms the theory of the Standard Model of particle physics [11].
The interactions involving neutrinos are described by two components in the Lagrangian:

$$\mathcal{L}_\nu = \mathcal{L}^\nu_{cc} + \mathcal{L}^\nu_{nc} \tag{1.6.1}$$

where:

- **Charged current (CC) interactions**:

$$\mathcal{L}^\nu_{cc} = -\frac{g}{4\sqrt{2}} \sum_{\alpha=e,\mu,\tau} \left(\bar{\nu}_\alpha \gamma^\mu (1-\gamma^5) l_\alpha W^+_\mu + \bar{l}_\alpha \gamma^\mu (1-\gamma^5) \nu_\alpha W^-_\mu\right)$$

  These V-A currents describe the interaction of neutrinos with their corresponding charged leptons (electron, muon, tau) via the exchange of $W^\pm$ bosons.

- **Neutral current (NC) interactions**:

$$\mathcal{L}^\nu_{nc} = -\frac{g}{cos\theta_W} \sum_{\alpha=e,\mu,\tau} \bar{\nu}_\alpha \gamma^\mu (1-\gamma^5) \nu_\alpha Z_\mu$$

  These neutral currents, which were not included in Fermi's theory, describe the interaction of neutrinos via exchange of a Z_0 boson.

1.7 Neutrino Cross Sections

Neutrinos are studied across various energy scales, as shown in Figure 1.15, which highlights the importance of different energy ranges for various neutrino sources.

- **Thresholdless processes: $E_\nu \sim$ 0-1 MeV**
  - **Coherent scattering**: this involves a neutral current (NC) interaction where the neutrino interacts coherently with an entire nucleus:

$$\nu + A^Z_N \rightarrow \nu + A^{Z*}_N.$$

    At low energies, the cross-section is expected to scale with the square of the atomic number (A^2) since the interaction is coherent across all nucleons. Coherence occurs when the momentum transfer Q is much smaller than the

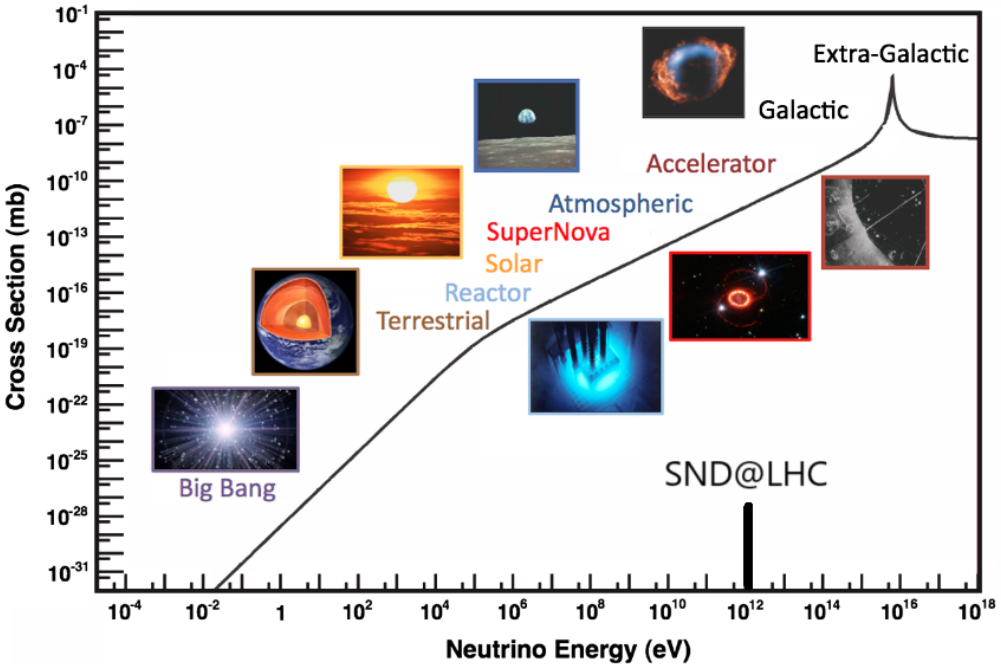

Figure 1.15: Representative example of various neutrino sources across decades of energy. The electroweak cross section for $\bar{\nu}_e + e^- \to \bar{\nu}_e + e^-$ scattering on free electrons as a function of neutrino energy (for a massless neutrino) is shown for comparison. The peak at 10^{16}eV is due to the W resonance [12].

inverse of the nuclear radius R (i.e., $QR \ll 1$). Although this interaction has not yet been experimentally observed, advances in recoil detection technology (often used in dark matter experiments [12]) have been proposed for its detection.

– **Neutrino capture on radioactive nuclei**: this process, sometimes referred to as enhanced or stimulated beta decay occurs when a neutrino interacts with a target nucleus:

$$\nu_e + A^Z_N \to e^- + A^{Z+1}_{N-1}$$

This reaction could be useful to detect cosmological neutrinos, though it has yet to be observed.

- **Low-energy nuclear processes: $E_\nu \sim$ 1-100 MeV**
As neutrino energy increases, it becomes possible to probe smaller scales within the nucleus. At low energies, the nucleus behaves like a single entity in interactions, but at higher energies, individual nucleons can be resolved. The simplest nuclear interaction that can be studied is antineutrino-proton scattering, also known as

inverse beta decay:

$$\bar{\nu_e} + p \rightarrow e^+ + n.$$

This reaction is typically measured using neutrinos produced from fission in nuclear reactors. It has an important role in understanding supernova explosion mechanisms [12].

- **Intermediate energy cross sections:** $E_\nu \sim$ **0.1-20 GeV**
Increasing further the energy, the complexity of interactions grows, and several types of neutrino scattering processes become significant:

  – **Elastic and quasi-elastic scattering**: neutrinos can scatter elastically off nucleons liberating a nucleon from the target. The difference between elastically and quasi-elastically lies in the process itself: a charged current process is referred to as a quasi-elastic scattering, while a neutral current process is referred to as an elastic scattering. For energies up to $\sim$ 2 GeV, neutrino-hadron interactions are dominant as quasi-elastic, in this case, the neutrino scatters off the entire nucleon rather than partons [12].

$$\nu_l \; n \rightarrow l^- \; p \qquad \bar{\nu}_l \; p \rightarrow l^+ \; n$$

  It is also possible that neutrinos scatter elastically with the nucleons:

$$\nu \; n \rightarrow \nu \; n \qquad \bar{\nu} \; n \rightarrow \bar{\nu} \; n$$

$$\nu \; p \rightarrow \nu \; p \qquad \bar{\nu} \; p \rightarrow \bar{\nu} \; p$$

  – **Resonance production**: in this region, neutrinos can excite the nucleon up to a resonance state (Δ, N^*), which quickly decays into mesons, nucleons, and pions or kaons.

  – **Deep inelastic scattering**: neutrino can also resolve the individual quark constituents of the nucleon, resulting in the creation of an hadronic shower.

The total neutrino and antineutrino cross-sections for these intermediate energies show a linear energy dependence, as illustrated in Figure 1.16. At the lower energies, measurements suffer from low statistics, and antineutrino cross-sections are generally less well measured due to higher background contamination.

- **High energy processes:** $E_\nu \sim$ **20-500 GeV**
In this energy regime the most common scattering is the **deep inelastic**. At these energies, neutrinos scatter off individual quarks within nucleons, as shown in Figure 1.17.

This scattering has long been used to validate the Standard Model and to probe nucleon structure. It also help to measure cross-sections, electroweak parameters, coupling constants, nucleon structure functions [12].

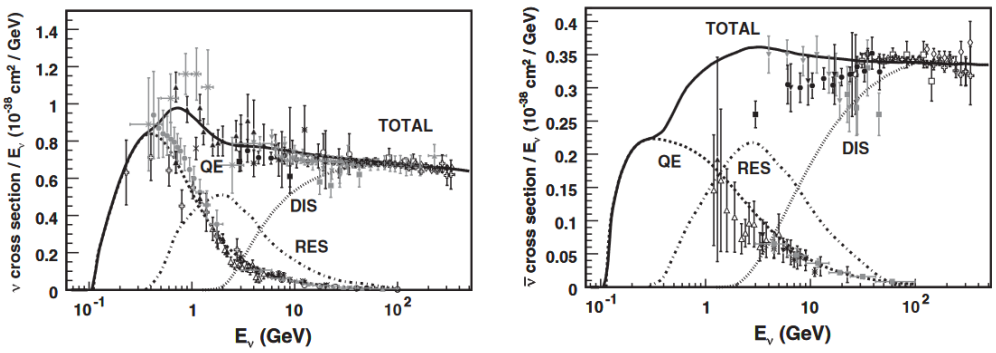

Figure 1.16: Total neutrino (on the left) and antineutrino (on the right) per nucleon CC cross sections divided by neutrino energy and plotted as a function of energy. Also shown are the various contributing processes: quasi-elastic (dashed), resonance production (dot-dashed) and deep inelastic scattering (dotted) [12].

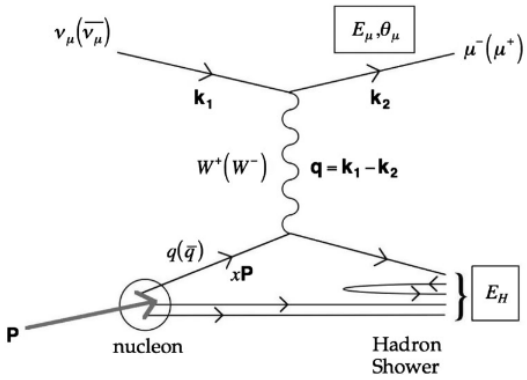

Figure 1.17: First order Feynman diagram of a Charged Current neutrino deep inelastic scattering (DIS) process. In the case of Neutral Current DIS, the outgoing lepton is instead a neutrino and the exchange particle is a Z boson [12].

- **Ultra high energy neutrinos: 0.5 TeV - 1 EeV**
  Data on neutrinos at this extreme energy scale are quite limited. Various astrophysical objects and mechanisms become accessible, offering information that complements existing data from electromagnetic or hadronic observations. However, a notable feature at these energies occurs when the neutrino undergoes resonant enhancement through the formation of an intermediate W boson in $\bar{\nu_e} + e^-$ interactions [12]. This resonance occurs at

$$E_{res} = \frac{M_W^2}{2m_e} \simeq 6.3 \text{ PeV}$$

  and is the dominant neutrino interaction up to 10^{21} eV as reported in Figure 1.18.

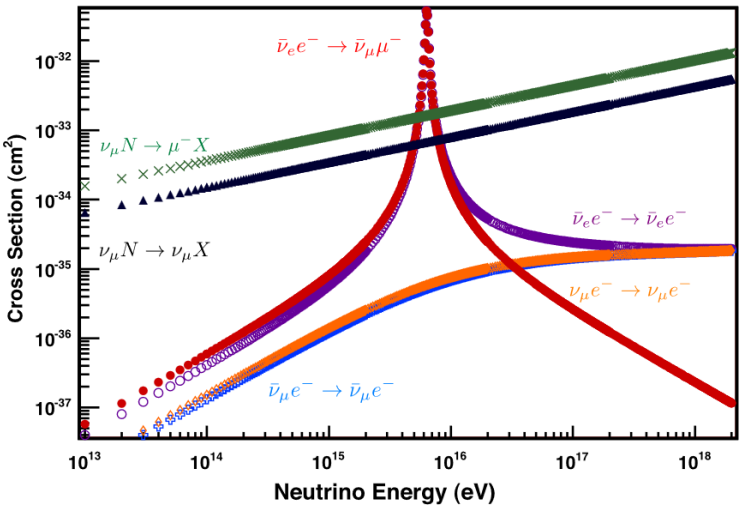

Figure 1.18: Neutrino electron and nucleon scattering in the ultra high energy regime. The leptonic W resonance channel is clearly evident with red circles and purple ones [12].

The SND@LHC experiment is currently investigating the lower end of this energy region for the first time in laboratory, using neutrinos generated in proton-proton collisions at the CERN Large Hadron Collider.

1.8 Neutrino oscillations

Neutrinos in the Standard Model are massless. The first to mention neutrino flavor oscillations were Maki, Nakagawa, and Sakata, who proposed that neutrinos possess mass and that the observed neutrinos are superpositions of different mass eigenstates. This concept is schematically represented in Figure 1.19. Due to their different masses, the neutrinos evolve differently over time and space, leading to oscillations in flavor [13].

- **Dirac mass**
  The Dirac mass term for neutrinos can be introduced by extending the Standard Model as follows

$$\mathcal{L}^D_{Mass} = -m\bar{\nu}_{\alpha L}\nu_{\alpha R} - m\bar{\nu}_{\alpha R}\nu_{\alpha L}$$

  where L and R denote left- and right-handed components [11]. In this extended model, three right-handed neutrinos are added to the theory right-handed neutrinos can also be called sterile, in fact they would interact with matter just through

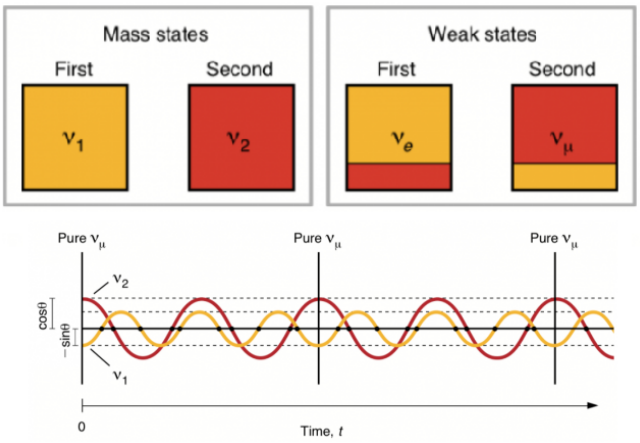

Figure 1.19: Schematic representation behind the idea of neutrino flavor oscillation, considering a simplified 2 flavor model.

gravitational interactions.
Neutrinos, therefore, gain mass like other particles:

$$m_i = \frac{y_i^\nu v}{\sqrt{2}} \quad (\mathrm{i} = 1, 2, 3) \tag{1.8.1}$$

where y_i^ν is the Yukawa coupling and v is the Higgs vacuum expectation value [14]. The unresolved aspect of this mechanism is why the Yukawa coupling for neutrinos must be much smaller compared to other leptons.

- **Majorana Neutrinos**
If we consider that ψ_L and ψ_R are not independent, even a massive fermion can be described using a two-component spinor rather than the usual four-component spinor. Majorana introduced a relationship between these two fields, expressed as:

$$\psi_R = C\bar{\psi}_L^T \tag{1.8.2}$$

where C is the charge conjugation matrix. From equation 1.8.2, it follows that to satisfy the Dirac equations [15]:

$$\begin{cases} i\gamma^\mu \partial_\mu \psi_L = m\psi_R \\ i\gamma^\mu \partial_\mu \psi_R = m\psi_L \end{cases} \tag{1.8.3}$$

The condition that must be satisfied is:

$$\psi_L^C = C\bar{\psi}_L^T \tag{1.8.4}$$

where ψ_L^C is the charge conjugate field. Thus, the Majorana field can be written as:

$$\psi = \psi_L + \psi_L^C = \psi^C \tag{1.8.5}$$

The equation 1.8.5 implies that the particle is identical to its antiparticle, so only neutral fermions can be described by a Majorana field. Neutrinos are the only known neutral particles that can be described in this way. The distinction between Dirac and Majorana neutrinos arises only if neutrinos have mass. To determine whether neutrinos are Dirac or Majorana, it is necessary to observe a mass-related effect. This effect cannot be kinematic, as the kinematics of Dirac and Majorana neutrinos are identical, such as those observed in neutrino oscillations. One method to distinguish Majorana neutrinos is by searching for neutrinoless double β-decay [16].

- **Heavy Neutral Leptons**
  The seesaw mechanism [17] is a model that explains why neutrino masses are so small. It introduces the existence of several electroweak-singlet (sterile) neutrino states, without specifying how many exist. Neutrinos with much higher masses than eV are called "Heavy Neutral Leptons" (HNLs) [17]. The Neutrino Minimal Standard Model (νMSM) extends the Standard Model by adding three right-handed neutrinos $N_{1,2,3}$. In particular, the scenario considers a lighter neutrino N_1 with a mass around keV as a potential Dark Matter candidate, while N_2 and N_3 have masses around GeV. These heavier neutrinos can be produced at the LHC through the decay of hadrons or W bosons resulting from proton-proton collisions, decaying into Standard Model particles [17], as shown in Figure 1.20. The SND@LHC experiment aims to search for these Heavy Neutral Leptons (HNLs) via their possible decays.

Now that we have discussed how neutrinos can acquire mass, let's define the weak eigenstates:

$$|\nu_\alpha\rangle = \sum_{i=1}^{3} U_{\alpha i}^* |\nu_i\rangle \tag{1.8.6}$$

with Greek indices for flavor neutrinos and Latin indices for mass eigenstates. The matrix U appearing in Equation (1.8.6) is called PMNS-matrix (Pontecorvo, Maki, Nakagawa and Saka).

A unitary $N \times N$ matrix can be parameterised by $\frac{N(N-1)}{2}$ angles and $\frac{(N-1)(N-2)}{2}$ complex phases. Thus, the PMNS-matrix involves three mixing angles and one phase as

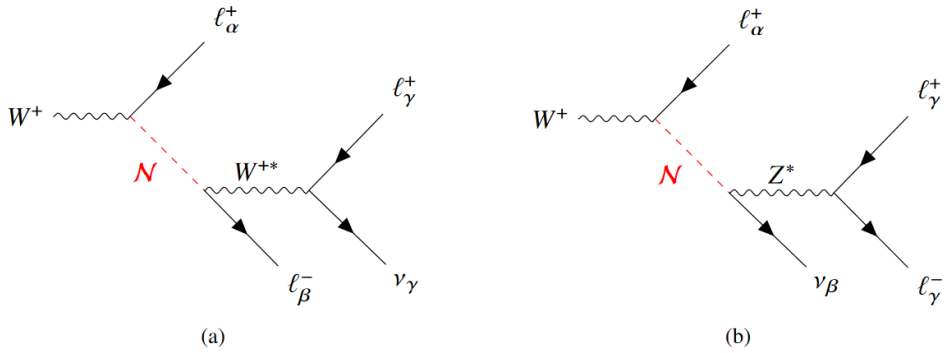

Figure 1.20: Feynman diagrams for the HNL production and decay modes into SM particles. The flavors of the leptons in the diagrams, labeled by α, β, and γ, are either muons or electrons. If the charged leptons in the HNL decay have the same flavor, then both the diagrams with the virtual W (a) and virtual Z (b) contribute to the process. Equivalent processes are also valid for an initial state W^--boson.

following:

$$\begin{pmatrix} c_{12}c_{13} & s_{12}c_{13} & s_{13}e^{-i\delta_{CP}} \\ -s_{12}c_{23} - c_{12}s_{13}s_{23}e^{i\delta_{CP}} & c_{12}c_{23} - s_{12}s_{13}s_{23}e^{i\delta_{CP}} & c_{13}s_{23} \\ s_{12}s_{23} - c_{12}s_{13}c_{23}e^{i\delta_{CP}} & -c_{12}s_{23} - s_{12}s_{13}c_{23}e^{i\delta_{CP}} & c_{13}c_{23} \end{pmatrix}$$

where the phase $\delta_{CP} \in [0, 2\pi]$, c_{ij} stands for $cos\theta_{ij}$ and s_{ij} for $sen\theta_{ij}$ and the mixing angles θ_{ij} can be taken in $\theta_{ij} \in [0, \pi/2]$. If the neutrino is its own antiparticle (i.e. a Majorana particle), the PMNS matrix can include an additional term:

$$\begin{pmatrix} e^{i\eta_1} & 0 & 0 \\ 0 & e^{i\eta_2} & 0 \\ 0 & 0 & 1 \end{pmatrix}$$

where η_1 and η_2 are Majorana phases, but these phases can be absorbed into the neutrino states, reducing the number of phases to one [11].

Returning to Equation (1.8.6), neutrinos are produced in weak-eigenstates, propagate in mass-eigenstates and are detected in weak-eigenstates. As each mass-eigenstate evolves over time, their differing phases lead to neutrino oscillations. The probability of oscillation over a distance L between the source and the detector, given an energy E is:

$$\langle \mathcal{P}_{\alpha\beta} \rangle = \frac{\int dE \frac{d\Phi}{dE} \sigma(E) P_{\alpha\beta}(E) \epsilon(E)}{\int dE \frac{d\Phi}{dE} \sigma(E) \epsilon(E)} \tag{1.8.7}$$

where $\sigma(E)$ is the cross section for the interaction process with the detector material and $\epsilon(E)$ represents the detection efficiency, both of which are experiment-dependent. In many cases, results can be expressed in terms of dominant oscillation, assuming two-neutrino states driven by a single $\Delta m^2 = m_i^2 - m_j^2$. Under this assumption, Equation (1.8.7) simplifies to:

$$\mathcal{P}(\alpha \to \alpha) = 1 - sen^2(2\theta) sen^2\Big(1.267 \frac{\Delta m^2[\text{eV}^2] L[\text{m}]}{E[\text{MeV}]}\Big)$$

$$\mathcal{P}(\alpha \to \beta) = sen^2(2\theta) sen^2\Big(1.267 \frac{\Delta m^2[\text{eV}^2] L[\text{m}]}{E[\text{MeV}]}\Big)$$

It's important to note that while experiments can provide information on the difference in mass values (i.e., Δm^2), they can not determine the absolute mass of the neutrino states. Furthermore, experiments can not reveal whether m_i is larger in mass than m_j, as the oscillation probability remains unchanged if $\Delta m^2 \to -\Delta m^2$. Another crucial factor in oscillation experiments is the ratio between L and E. Experiments can be specifically designed to maximize the probability of oscillation by ensuring:

$$1.267 \Delta m^2 \frac{L}{E} = \frac{\pi}{2} \implies \frac{\Delta m^2 L}{2E} \simeq 1 \ .$$

1.9 Neutrino physics in SND@LHC

For the SND@LHC experiment, the neutrino energies are approximately 1 TeV, and the detector is situated just 480 m away from the production point.
Given the measured values $\Delta m_{21} \simeq 10^{-5}$ eV^2 and $\Delta m_{31} \simeq 10^{-3}$ eV^2, the ratio L/E would be approximately $1/2000 \ll 1$.

Therefore, in the SND@LHC experiment, the neutrinos observed in the detector retain the flavors that the neutrinos have when produced in pp collisions. This has an important impact on the physics program of the experiment, for instance, high-energy electron neutrinos can be directly associated with the production and decay of c quarks [18].

By measuring charmed hadrons, the SND@LHC experiment can assess open charm production within the same rapidity window as the detected neutrinos.
Due to the linear correlation between the parent charm quark and the resulting hadron, this measurement provides valuable insights into charm quark production. At the LHC, the dominant partonic process for producing charm involves gluon-gluon scattering, which generates a $c\bar{c}$ pair [19].

The SND@LHC detector probes gluon interactions at an average minimum momentum fraction of approximately 10^{-6}, a region where the gluon parton distribution function (PDF) is currently unknown. Mapping the gluon PDF at these low x values could help

reduce uncertainties in Quantum Chromodynamics (QCD) predictions, which is essential for future hadron collider experiments.

Moreover, since SND@LHC is capable of identifying all three neutrino flavors, it allows for testing lepton flavor universality in the neutrino sector. This is achieved by measuring the ratios of ν_e/ν_τ and ν_e/ν_μ interactions.
The experiment also facilitates a direct search for feebly-interacting particles (FIPs), such as dark scalars, heavy neutral leptons, and dark photons [20].

The SND@LHC setup can differentiate between scattering events from massive FIPs and those from neutrinos, with the sensitivity of the results depending on the particle's mass.

Chapter 2

The SND@LHC Experiment

Proton-proton collisions at the Large Hadron Collider (LHC) produce a high-intensity neutrino beam in the far-forward direction, with an intensity of approximately 10^{12} neutrinos and energies reaching up to a few TeV. SND@LHC is a compact, standalone experiment located in the TI18 tunnel, positioned 480 m downstream of the ATLAS Interaction Point (IP). This setup enables the identification of interactions for all three neutrino flavors in the pseudorapidity region $7.2 < \eta < 8.4$ [21].

2.1 The SND@LHC detector

The SND@LHC apparatus consists of different key components: first of all a veto system, then a target region and at the end a hadronic calorimeter paired with a muon identification system (Figure 2.1). The target region weighs approximately 830 kg and it contains five Emulsion Cloud Chambers (ECC) walls, each wall is followed by a Scintillating Fibre (SciFi) plane [21].

The Emulsion Cloud Chamber (ECC) technology leverages emulsion films to achieve sub-micrometric tracking resolution. These films are alternated with tungsten layers, which act as the target for neutrino interactions.

The SciFi planes provide position and timestamp information for reconstructed tracks. Together, emulsion target and target tracker serve also as a sampling electromagnetic calorimeter, with an overall thickness of 85 radiation lengths X_0, and 1.5 interaction lengths, λ_{int}.

The veto system, emulsion target, and tracker are enclosed within a box made from 30% borated polyethylene and acrylic to stabilize temperature and humidity, to maintain optimal conditions for emulsion films. It serves also as a shield from low-energy neutrons. This is reported in Figure 2.2.

Positioned downstream of the target, the hadronic calorimeter and muon identification

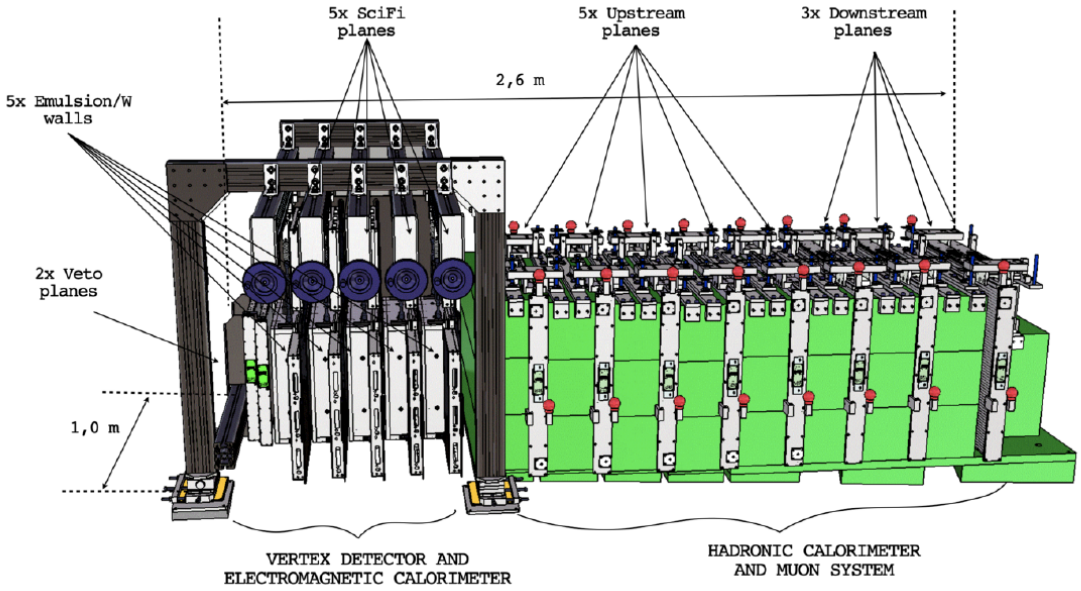

Figure 2.1: Layout of the SND@LHC apparatus: veto planes followed by a target region and a hadronic calorimeter and muon system

system include eight iron slabs, each 20 cm thick, yielding a combined 8 λ_{int}. After each slab, one or two planes of 1 cm, as better described in section 2.1.2, thick scintillating bars are placed.

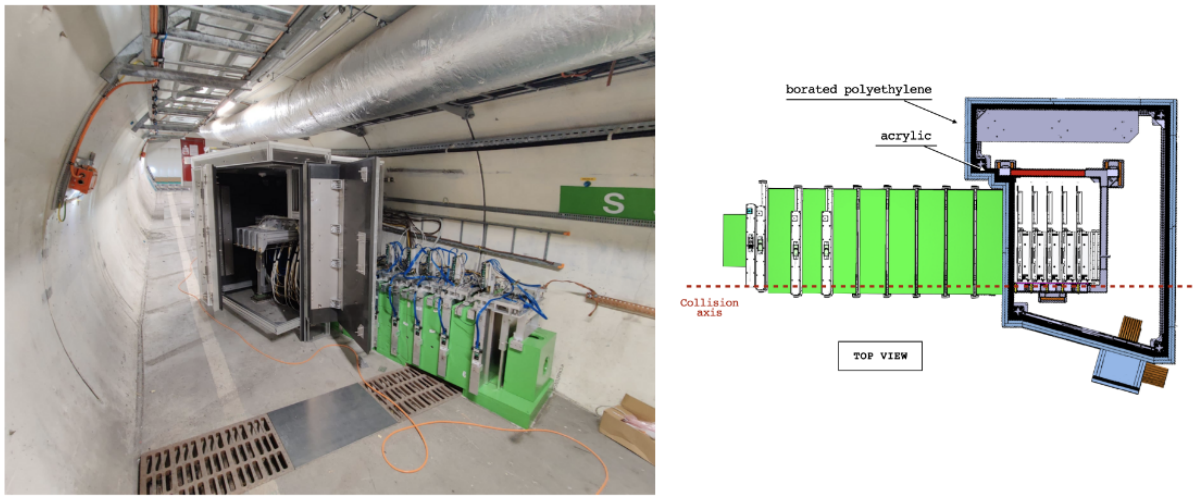

Figure 2.2: On the left a global view of the detector in TI18, on the right the top view of the shield around the target region.

2.1.1 Emulsion Target

The emulsion target is arranged in five walls, each one has a sensitive transverse area of 384×384 mm^2 [21]. Each of these walls is composed by four bricks as shown in Figure 2.3.
The brick is made of 60 emulsion films that have a transverse size of 192×192 mm^2 and are interleaved with 59 tungsten plates, each 1 mm-thick. Tungsten was chosen as

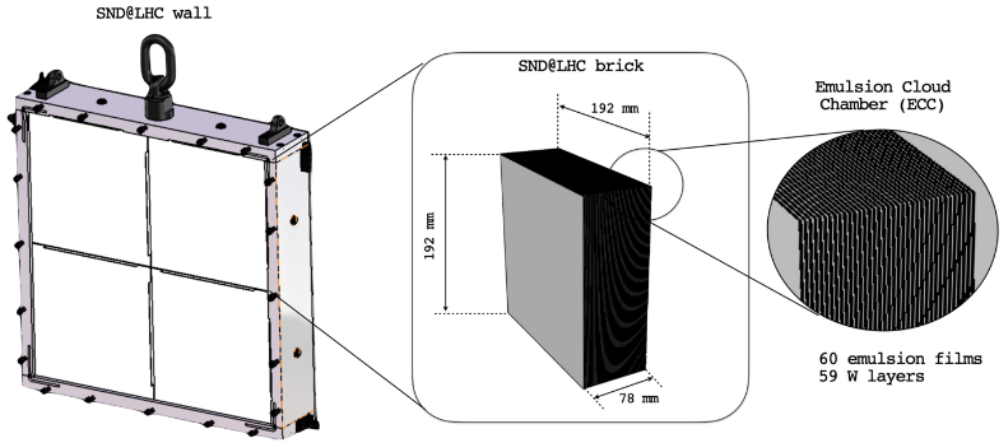

Figure 2.3: An SND@LHC emulsion wall composed of four bricks, each consisting of 60 emulsion films interleaved with 59 tungsten layers

the target material due to its high density, which maximizes the interaction rate within the compact volume. Additionally, its low radioactivity makes it a suitable choice for an emulsion-based detector.

When a charged particle crosses an emulsion, it leaves trails of micro-tracks on it. The track segments left by passing particles in consecutive films enable vertex reconstruction with precision at the micron level. Each nuclear emulsion film has two sensitive layers, each 70 μm thick, on either side of a transparent plastic core that is 170 μm thick.
By connecting the two segments, the slope of the track can be measured with milliradian precision.

The emulsion target is replaced every ~ 20 fb^{-1} of data collected to prevent an unmanageable amount of combinatorics during track reconstruction [22]. Then, emulsion films are developed and analyzed by fully automated optical microscopes.

2.1.2 Electronic Detector

The first component of the electronic detector is the veto system, which has to reject all charged particles entering in the fiducial volume of the detector.

It comprises 3 parallel planes of seven $1 \times 6 \times 42$ cm^3, stacked scintillating bars read out on both ends by 8 SiPMs each [21]. Bars are wrapped in aluminized Mylar foil to ensure opacity and isolate them from light in adjacent bars.

Since 2024 the number of veto planes increased from 2 to 3 [23], the upgrade is reported in Figure 2.4.

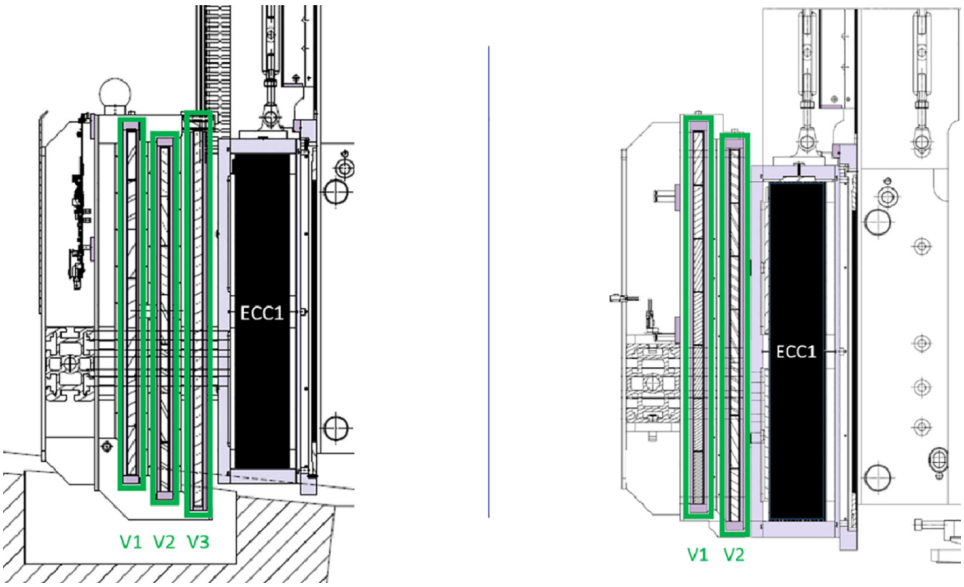

Figure 2.4: On the left, it is possible to see the upgraded veto system, which includes the addition of the third veto plane. On the right, is reported the veto system used until 2023.

Following the veto system, the SciFi detector provides critical timing and energy measurements for neutrino interactions reconstructed within the ECC walls.
The functions of SciFi include: assignment of a timestamp to collect events and a measurement of the energy of electromagnetic showers generated in these interactions occuring in the target region.
Additionally, when combined with the scintillating bars of the muon detector, SciFi serves as a non-homogeneous hadronic calorimeter. This combined system allows for the energy measurement of hadronic jets resulting from neutrino interactions and as a tracking system in the target, SciFi is also used to match emulsion and electronic data.
Each SciFi station consists of two 40×40 cm^2 planes, each constructed with alternating X and Y oriented mats.
Each mat consists of six densely packed, staggered layers of polystyrene-based scintillating fibers, each of 250 μm diameter, and read out by arrays of SiPM.
The SciFi station achieves a spatial resolution of approximately ~ 150 μm per view for single particle, and a time resolution of around ~ 250 ps when particles cross both X

and Y mats within a single plane [24].

The muon system and hadronic calorimeter constitute the final component of the electronic detector, divided into two sections: the UpStream (US) and DownStream (DS) segments.
The US segment comprises the first five stations, while the DS segment includes the final three stations. Both segments are designed to ensure light-tightness with each scintillator bar encased in aluminized Mylar foil. Each US station consists of 10 horizontal scintillator bars stacked vertically, with dimensions of $1 \times 6 \times 82.5$ cm^3. This configuration provides a coarse Y-axis view, similar to the design of the veto detector as shown in Figure 2.5. Each end of a US bar is observed by eight SiPMs, six of which are larger

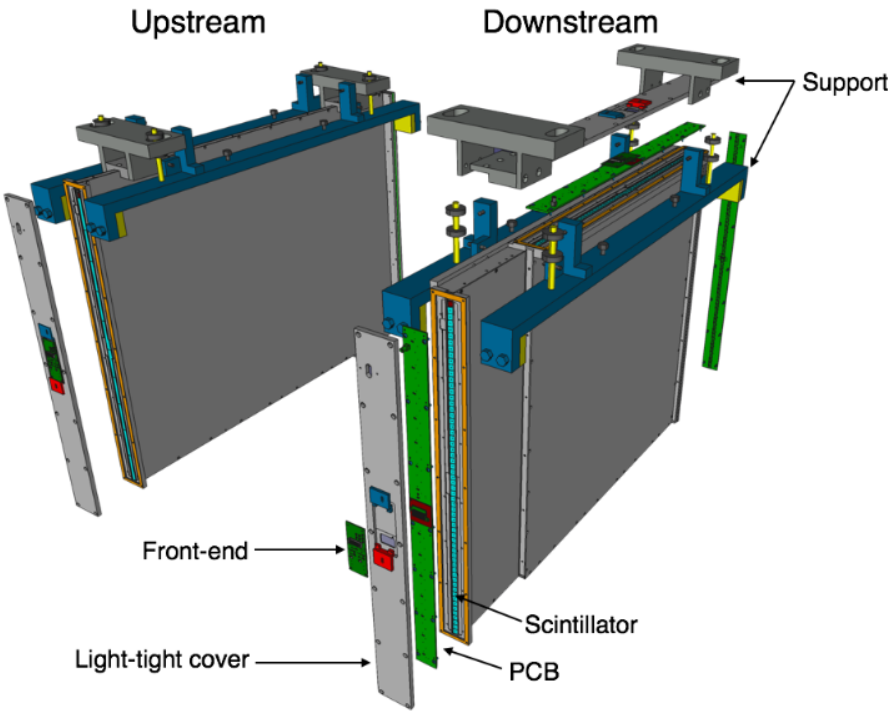

Figure 2.5: Illustration of an upstream and a downstream plane. The downstream plane presents a double layer to perform both measurements in the X and Y directions.

6×6 mm^2 with a 50 μm pitch, while the remaining two are smaller 3×3 mm^2 with a 10 μm pitch [21].
In the DS segment, each station consists of two layers of 60 thinner bars, each $1 \times 1 \times 82.5$ cm^3, arranged alternately in the X and Y directions. This configuration provides spatial resolution below 1 cm along each axis, enabling precise particle localization.
Each horizontal DS bar end is read by a single small SiPM, while vertical bars are read from only the top. The time resolution for a single DS bar is approximately ~ 120 ps.

The DS segment spatial resolution allows to identify and track exiting muon tracks with high precision.
The eight scintillator planes of the muon system are interleaved with 20 cm thick iron blocks, which contribute to the calorimeter functionality by increasing the hadronic energy absorption.

2.1.3 Event Reconstruction

The identification of neutrino flavor in charged-current interactions relies on recognizing the type of charged lepton produced at the primary interaction vertex, as shown in Figure 2.6.

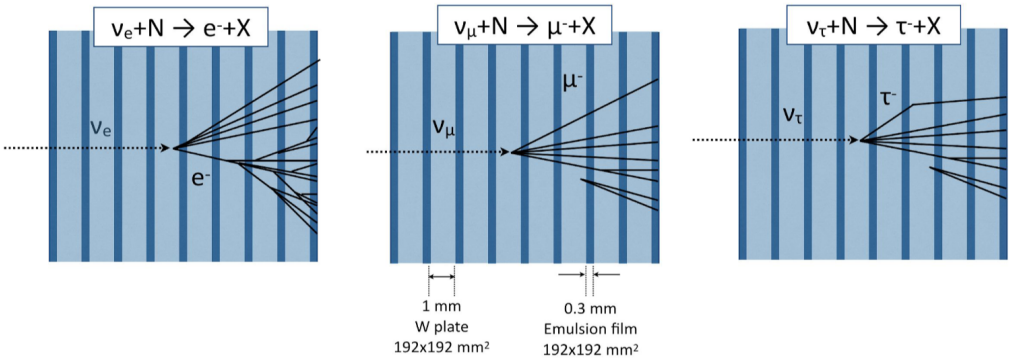

Figure 2.6: Event signatures for different neutrino flavors, identified by the lepton produced at the primary vertex. ν_e produces an electromagnetic shower, ν_μ produces a muon detected by the muon system, ν_τ results in a tau decay in the ECCs.

Electron neutrinos (ν_e) are identified by the production of an electromagnetic shower. The micrometric precision and dense sampling of the ECC allow for effective separation of electrons from neutral pions, as photon conversions occuring downstream of the neutrino interaction vertex can be detected with high accuracy.

Muon neutrinos (ν_μ) are recognized by the presence of a muon and a hadronic shower, which is identified by its penetrating track through the entire muon detection system.

Tau neutrinos (ν_τ) are detected through the distinct topological signature of tau decay in the ECCs, where the decay products of the tau lepton are observed [21].

2.1.4 Background sources

At the detector location, muons constitute the primary source of background. In neutrino searches, backgrounds from machine-induced sources generally decrease with increasing distance from the interaction point and with greater separation from the beam line [21].

Muons, originating from upstream interaction in the rock separating IP and the detector, can mimic neutrino signals through two distinct mechanisms: they can directly enter into the target, undetected by the veto system and then generate showers in the target both via bremsstrahlung or deep inelastic scattering, or they can make secondary interactions with the surrounding materials producing neutral particles that can enter in the target region and mimic neutrino events [22].
The background from muons is estimated using both the muon flux expected within the fiducial volume and the inefficiency rate of the detector's veto planes. The predicted muon flux, based on Monte Carlo simulations, is approximately 1.69×10^4 fb/cm^2. Data collected during 2022 run confirmed this flux prediction [25].

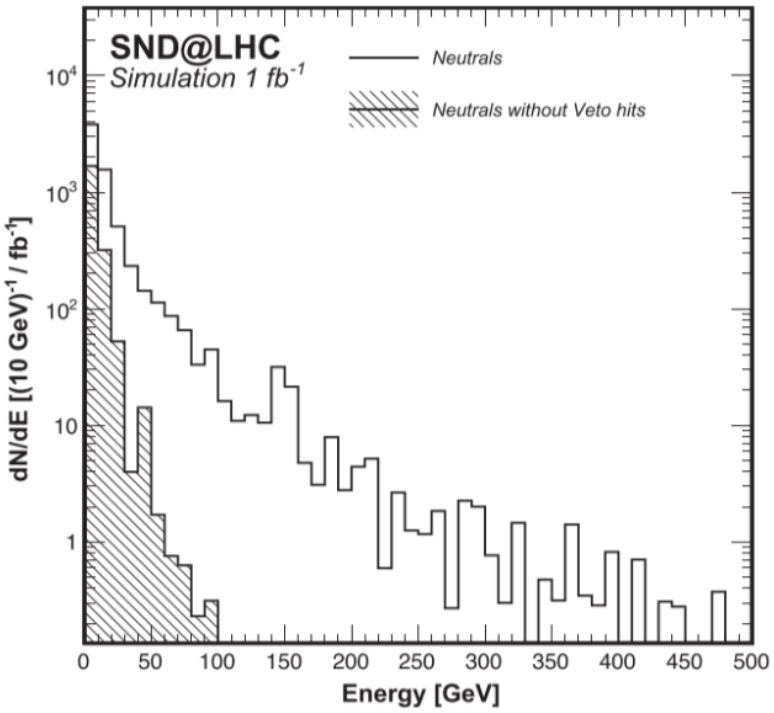

Figure 2.7: Energy spectrum of neutral hadrons entering in SND@LHC detector acceptance. The shaded area shows the spectrum after rejecting events with hits in the veto system using only 2 planes [21].

Neutral particles, such as neutrons and K_L^0 mesons, pose an additional background.
These particles can be produced when primary muons interact with the surrounding rock and concrete and may create showers in the target if they enter undetected by the electronic detectors.
However, such events are largely mitigated by the veto system, which detects accompa-

nying charged particles generated during the primary muon interaction.
Simulations of the energy spectrum of neutral hadrons within the fiducial volume further validate this mitigation, demonstrating the effectiveness of the veto system in excluding such particles from the neutrino signal as shown in Figure 2.7

2.2 Test beam

A comprehensive test beam campaign was conducted to characterize the performance of the SciFi tracker and Muon system, designed as a non-homogeneous hadronic calorimeter with an effective interaction length of approximately 11 λ_{int} [26].
The detector configuration used in the test beam setup is reported in Figure 2.8. The

Figure 2.8: Picture of the test beam setup. The SciFi detector is on the right, and the backward section includes the US stations.

target region was composed of three 10 cm thick iron walls, designed to replicate the interaction lengths found in the SND@LHC experiment.
Four 13×13 cm^2 SciFi planes, smaller replicas of the detectors used in SND@LHC, were installed between the iron slabs.
Each SciFi station contained one horizontal and one vertical plane of fibers, allowing for precise measurement of particle positions in both the X and Y coordinates.

The test beam setup comprised five US stations of large scintillating bars, forming the sensitive part of the HCAL. Each station included ten plastic scintillator bars, each 60 mm wide, 830 mm long, and 10 mm thick, arranged horizontally.
These bars were wrapped in 20 μm thick aluminized Mylar foil to ensure light containment, and framed between two 2 mm thick aluminum sheets. For readout, SiPMs were installed at both ends of each bar, with each US station equipped with 60 large and 20 small SiPMs, providing high-resolution data on particle interactions.

Additionally, a DS station with two planes of thin scintillating bars was positioned beyond the HCAL. This station consisted of 60 bars, each 10 mm wide, arranged horizontally in the first plane and vertically in the second. This configuration enabled precise detection of particle showers and provided further spatial resolution.

While the target's size was reduced compared to that in SND@LHC, this setup effectively captured the primary characteristics of hadronic shower development, provided the beam was centered within the SciFi acceptance, as reported in Figure 2.9.
Data were collected with hadron beams across five distinct energy levels: positive hadron beams (protons and pions, collectively referred to as the π^+ beam) were delivered at 100, 140, and 180 GeV, while π^- were tested at 240 and 300 GeV, utilizing the SPS H8 beamline [21].

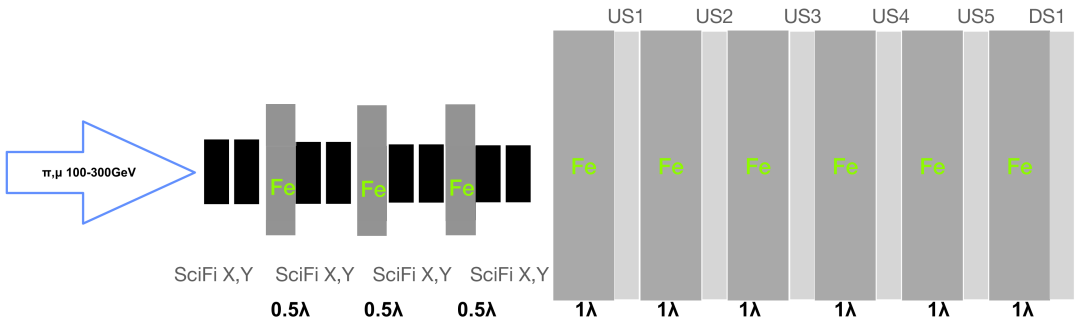

Figure 2.9: Sketch of the test beam setup.

Chapter 3

Analysis

The reconstruction of the direction of hadronic showers plays a crucial role in the study of neutrino interactions. Precise knowledge of the shower position and direction is critical because it allows to correlate the observed hadronic activity with the incident neutrino, thereby enabling a more accurate determination of neutrino energy. The work presented in this thesis is based on the analysis of Test Beam data, where the energy and direction of incoming particles are well-defined and known.
By studying the performance of the detector under these controlled conditions, it becomes possible to evaluate how accurately the shower direction can be reconstructed in the SND@LHC experiment installed in the TI18 tunnel. This analysis provides valuable insight into the associated uncertainties and systematic errors, which are relevant for interpreting results from TI18 and for improving the overall accuracy of neutrino energy reconstruction. For this purpose, 5 million events were analyzed for each of the following runs at the specified energies, as reported in Table 3.1.

Energy (GeV)	Particle	Run Number	Run Number	Run Number
100	π^+	100630	100632	-
140	π^+	100633	100674	-
180	π^+	100635	100636	100671
240	π^-	100672	100646	100647
300	π^-	100639	100642	100643

Table 3.1: Run collected for different values of energy.

3.1 Centroid reconstruction

The core of this study is based on the analysis of the digitized-integrated-charge QDC signals collected by the detectors. Charge-to-digital converters (CDC) are electronic devices designed to convert analog signals, in the form of electric charge, into digital values (QDC), thus providing a numerical representation of the amount of charge collected by a detector.
A CDC operates by measuring the electric charge generated within a defined time interval (known as the gate time) and outputs a digital value proportional to the integrated charge. The charge typically results from the integration of current pulses generated by a sensor, which detects the energy deposited by charged particles or photons. In Figure 3.1, the QDC values collected (only in SciFi) as a function of the system clock cycles are shown, where a single clock cycle corresponds to 6.25 ns.
The majority of the QDC is recorded within a clock cycle, as highlighted by the red bars in the Figure 3.1, centered around the reference time, defined as the moment when the maximum amount of QDC is registered by the collection system.

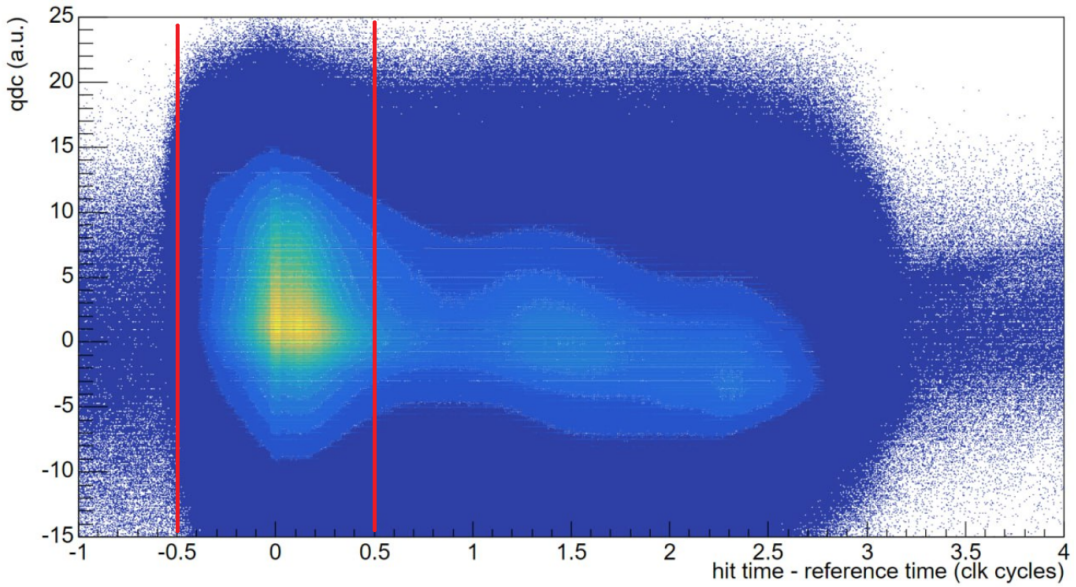

Figure 3.1: QDC collected in SciFi as a function of clock cycles. The majority of the QDC is collected within one clock cycle centered around the reference time, which is the moment when the most QDC is collected, set at 0.

The QDC data are then analyzed plane by plane. Figure 3.2 shows the QDC collected by the four SciFi detector planes within the defined time window. In this example, a shower event caused by a 240 GeV pion is displayed. Late QDC signals are due to noise and have been excluded from the analysis to focus on the physical signal.

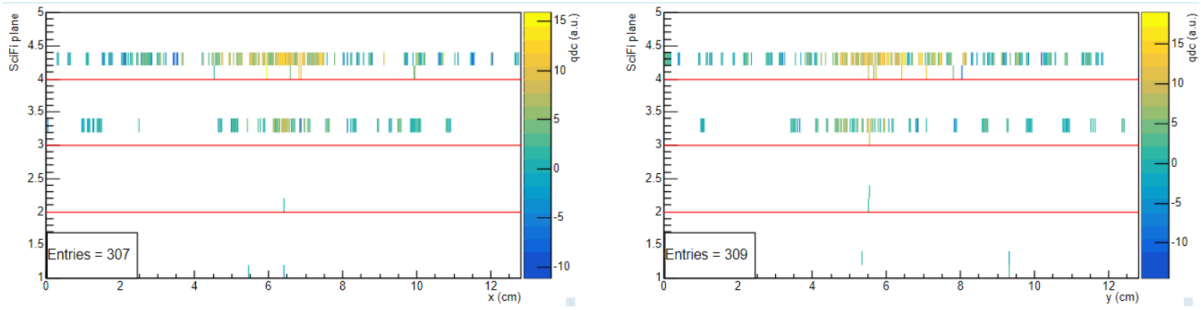

Figure 3.2: QDC collected for each of the four planes (red horizontal lines) in the SciFi detector. The data correspond to a shower event of a 240 GeV pion. Late QDC signals have already been excluded.

The next step in the analysis involves using the positions of individual hits, each associated with a specific QDC value, to compute a weighted average and determine the midpoint of the shower for each detector plane. This midpoint is referred to as the *centroid*. The position of the centroid is calculated by considering only the hits with positive QDC values. Negative QDC values can occur due to the threshold chosen during data acquisition, as very low signals, such as those from a passing MIP or noise, can result in negative QDC values. For each SciFi plane, the centroid position is defined as:

$$x_{centroid} = \frac{\sum_i QDC_i \cdot x_i}{\sum_i QDC_i}$$

where QDC_i represents the charge recorded for the i-th hit, and x_i is its geometric position in the detector. The same formula is applied to calculate the y coordinate of the centroid. This weighted approach ensures that hits with higher QDC values, which correspond to larger energy deposits, exert a stronger influence on the centroid position. By reconstructing the centroid for each plane, it is possible to trace the development of the shower across the detector.

This information is crucial for reconstructing the direction of the shower, directly linked to determining the energy and trajectory of the primary particle that initiated the shower. To estimate the shower direction, a linear fit is performed on the centroid positions across the detector planes as a function of their depth (z coordinate).

Figure 3.3 shows the geometry of the test beam setup implemented in the simulation, including the arrangement of the SciFi planes in x and y directions and their interleaving with iron layers, as described in Section 2.2.

A shower tagging algorithm (ShowerStart) was implemented to identify the plane where the shower begins. This algorithm requires at least 36 out of 128 channels window in a plane to be active. By employing this tagging system, it is possible to determine the

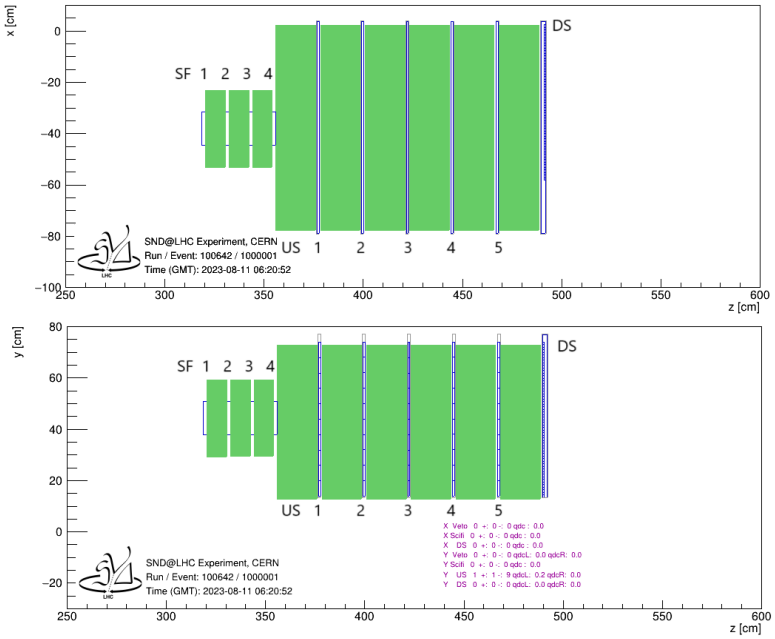

Figure 3.3: Test beam geometry implemented in the software, showing the arrangement of SciFi planes in x and y directions and the interleaved iron layers. It is also present the five US planes and the DS plane are also present.

starting plane of the shower.

For example, a ShowerStart value of 2 indicates that the shower begins in the first layer of iron and is observed from the second SciFi plane. Similarly, a ShowerStart value of 3 means that the shower starts in the second iron layer and is observed in the third SciFi plane. Below, the distribution of the shower centroid positions across the different planes is shown for ShowerStart = 2 for the 100 GeV in Figure 3.4, while plots for the other energies are in the Appendix (Figure A.1 for 140 GeV, Figure A.2 for 180 GeV, Figure A.3 for 240 GeV, and Figure A.4 for 300 GeV).

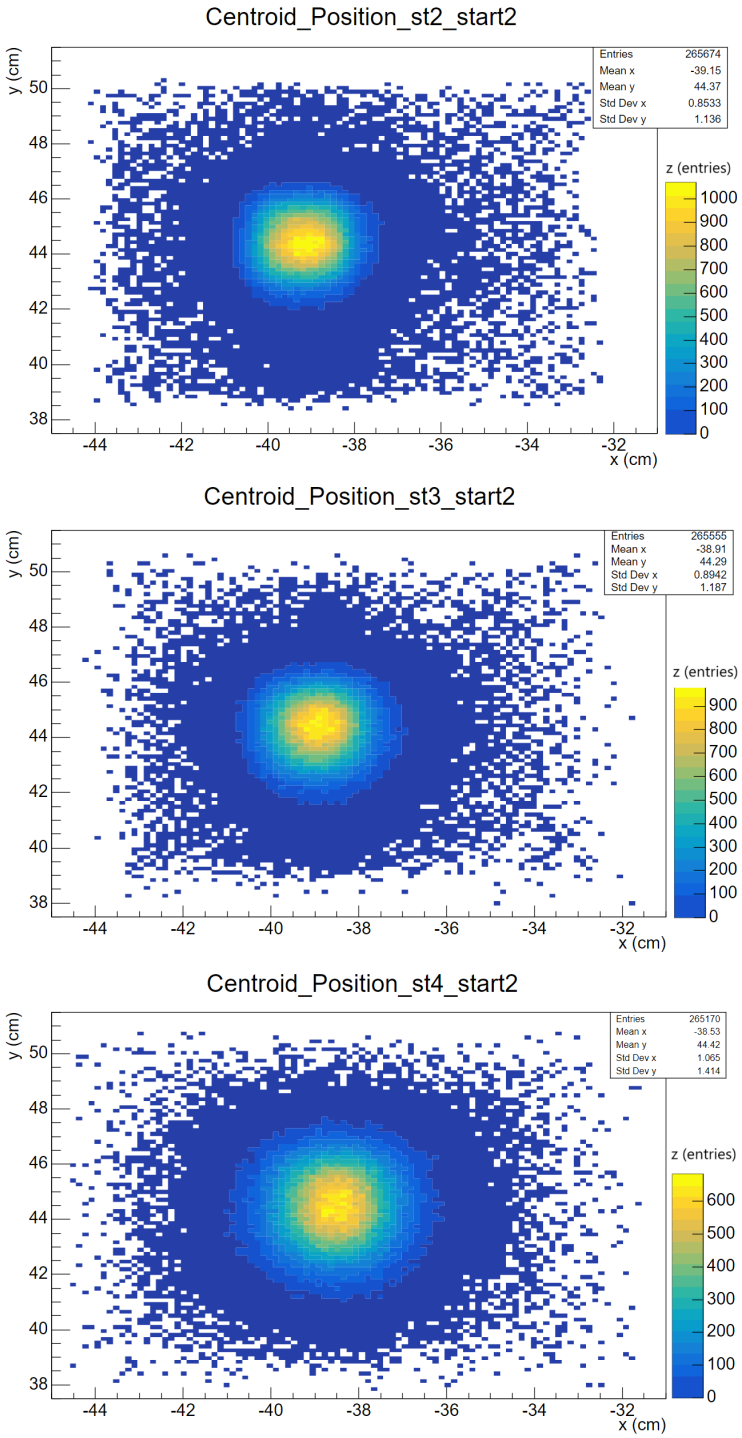

Figure 3.4: Display of the development of the centroid positions for 100 GeV pion beams, in events tagged with ShowerStart = 2. The centroid positions in SciFi stations 2 (top), 3 (middle), and 4 (bottom) are shown.

Linear fits of the centroid positions were performed separately for the x and y directions as a function of the z coordinate of the planes. The fit was performed when more than two centroids were identified, and both x and y coordinates were available in the same plane. Errors assigned to the centroid positions were 0.025 cm in both x and y directions, corresponding to the diameter of a scintillating fiber in SciFi, while in z, the error was taken as six times this value. This is due to the detector's design as depicted in Figure 3.5.
Individual channels are read separately in x and y, while in z each SiPM is placed in such a way to receive light from all the 6 layers of fibers. The slopes of the linear fits,

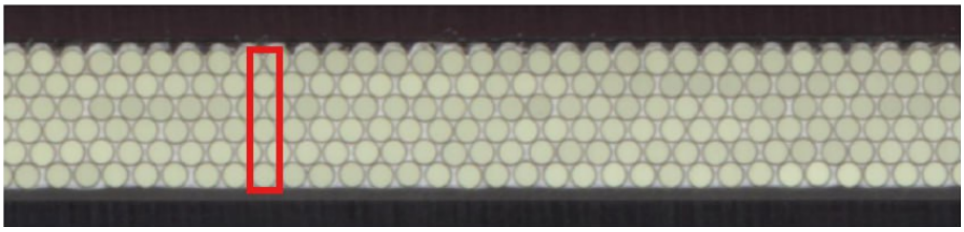

Figure 3.5: Channels in SciFi planes. Each SiPM reads 6 fibers simultaneously, as shown in the red box.

representing the shower's direction in xz and yz plane, were analyzed for different energy configurations. To summarize and provide a comprehensive comparison of all energy configurations, the slopes for each energy setting were normalized and presented together in Figure 3.6. Specifically, the number of entries for each bin were scaled by the total number of entries for the respective energy configuration. This normalization ensures that all graphs are displayed on the same scale, allowing for a direct and meaningful comparison. The single plots, instead, are reported in the Appendix (Figure A.5 for 100 GeV, Figure A.6 for 140 GeV, Figure A.7 for 180 GeV, Figure A.8 for 240 GeV, Figure A.9 for 300 GeV).

The results are reported in the following Table 3.2.
The values are all approximately consistent with zero, as expected, given that the pion beams were directed as perpendicular as possible to the detector. The next section focuses on studying the resolution with which position and direction of hadronic showers can be reconstructed.

3.2 Resolution

To validate the precision and implementation of the method, we verified whether the reconstructed shower positions obtained from our method are consistent with the positions where the pion beam strikes the first plane of the SciFi detector, which is not preceded

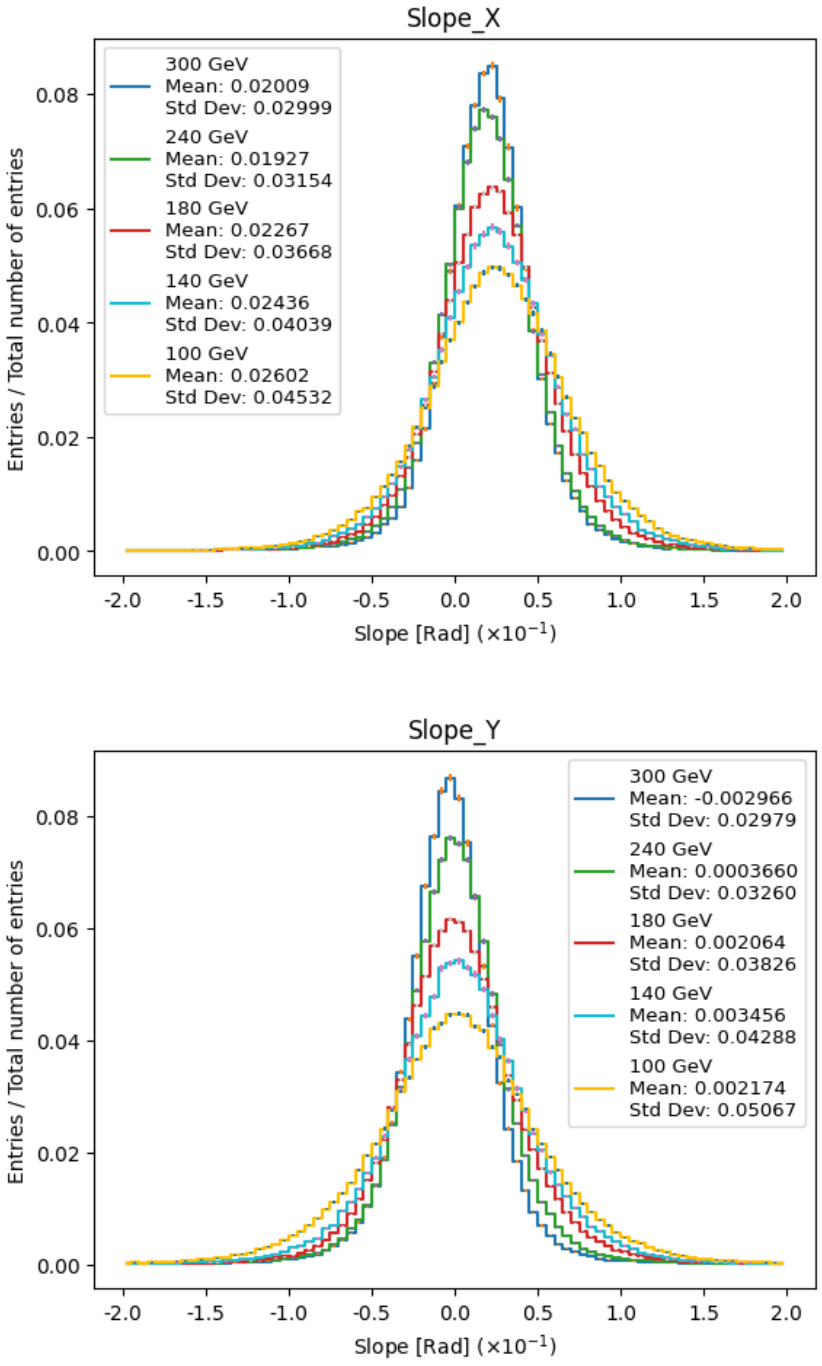

Figure 3.6: Global visualization of slopes for all energy configurations in x and y directions. Data are normalized to the total number of entries for each configuration.

	Slope X (Rad·10^{-2})	Slope Y (Rad·10^{-2})
100 GeV	2.6 ± 4.5	0.2 ± 5.1
140 GeV	2.4 ± 4.0	0.3 ± 4.3
180 GeV	2.3 ± 3.7	0.2 ± 3.8
240 GeV	1.9 ± 3.2	0.0 ± 3.3
300 GeV	2.0 ± 3.0	-0.3 ± 3.0

Table 3.2: Summarizing Table with all the Slopes in x and y direction at the different energy configurations.

by an absorber. Specifically, we analyzed the positions of the beam hits on the first plane in both the x and y coordinates. The selection criteria for reporting the beam hits are as follows: hits must fall within the temporal window described previously and a shower must be observed in the following planes.
The hit distributions in the first SciFi plane show the beam profiles superimposed to a uniform distribution of random noise hits. In Figure 3.7 are reported the hits for the beam at 100 GeV, the other energy configurations are reported in the Appendix (Figure A.10 for 140 GeV, Figure A.11 for 180 GeV, Figure A.12 for 240 GeV, Figure A.13 for 300 GeV).
To evaluate the reconstructed positions derived using our method, the intersection of the fitted trajectory with the first SciFi plane was computed using the following equations:

$$Y_{first} = slope_y \cdot z_y + intercept_y$$

$$X_{first} = slope_x \cdot z_x + intercept_x$$

where $z_y = 319.3$ cm and $z_x = 319.9$ cm are the z coordinates of the first plane, and the slope and intercept are the parameters obtained from the fit.

Figure 3.8 shows the distributions of the reconstructed positions in the first SciFi plane for different energy configurations. These plots are normalized to the number of entries to facilitate comparison across energy levels.
The vertical green bars indicate the edges of the SciFi plane.

Figure 3.9 summarizes the results obtained for the mean positions and dimensions of the beam and reconstructed distributions.
In particular, 3.9a shows the fitted beam positions and dimensions, while 3.9b shows the reconstructed beam positions and dimensions.
The reconstructed beam positions and dimensions are in good agreement with the beam setup parameters, demonstrating the validity of our method.
To quantify the method's resolution, we calculated the displacement between the *true* beam position and the reconstructed position for each event. The *true* beam position

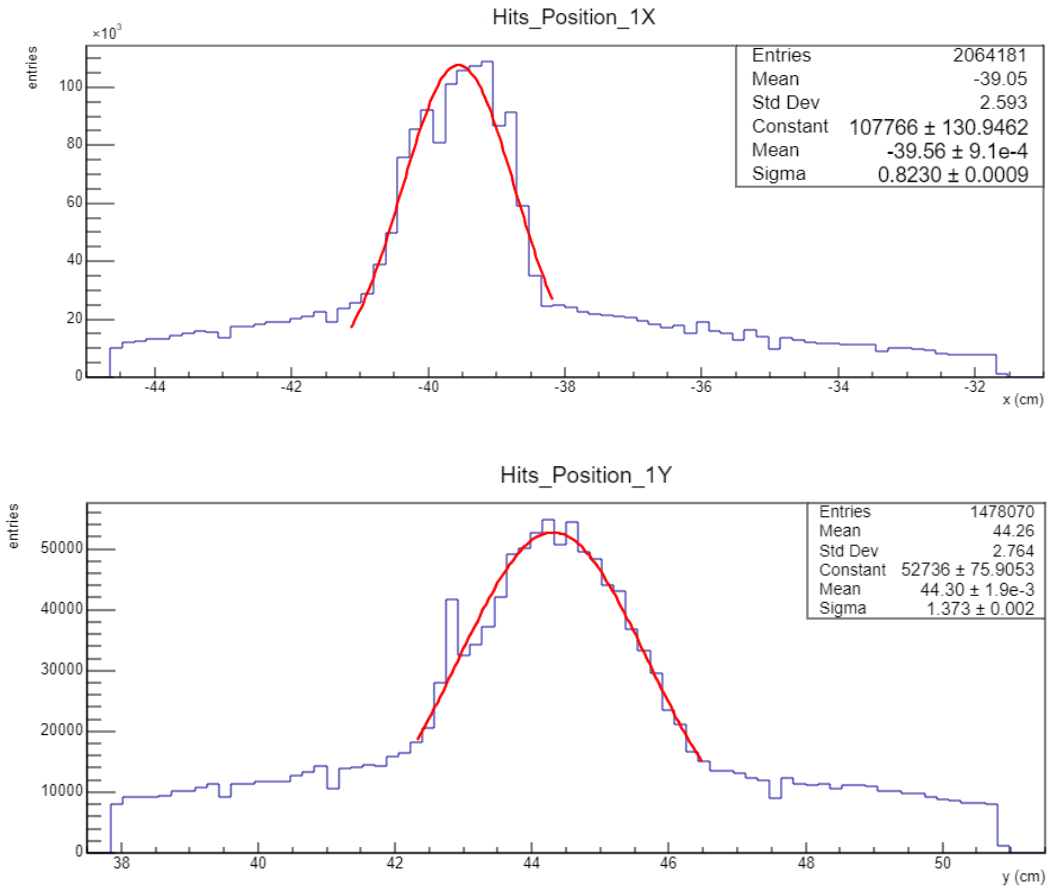

Figure 3.7: Hits position in the first x and y plane of SciFi at 100 GeV.

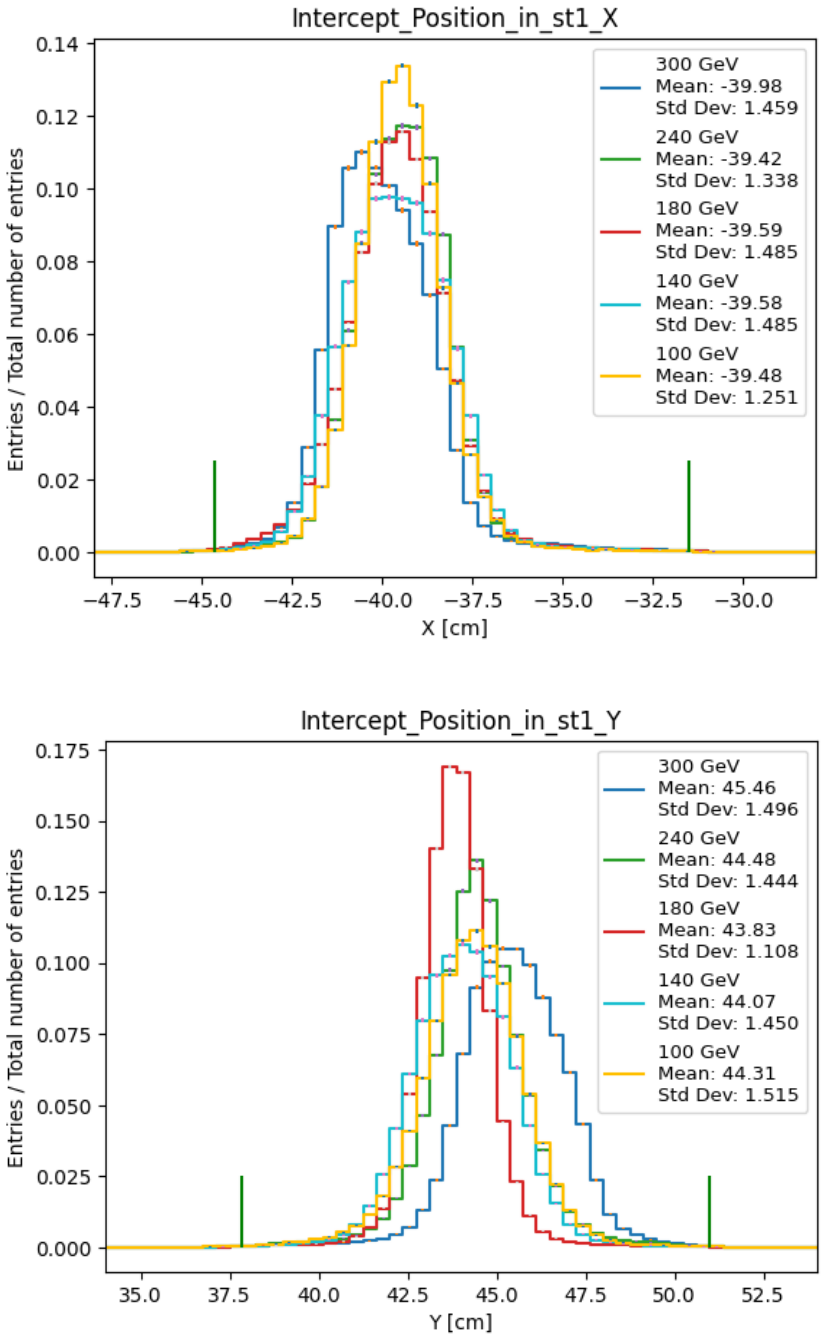

Figure 3.8: Extrapolated hit positions in the first layer of SciFi from the reconstructed shower centroids and shower axis directions. The vertical green bars indicate the edges of the SciFi plane.

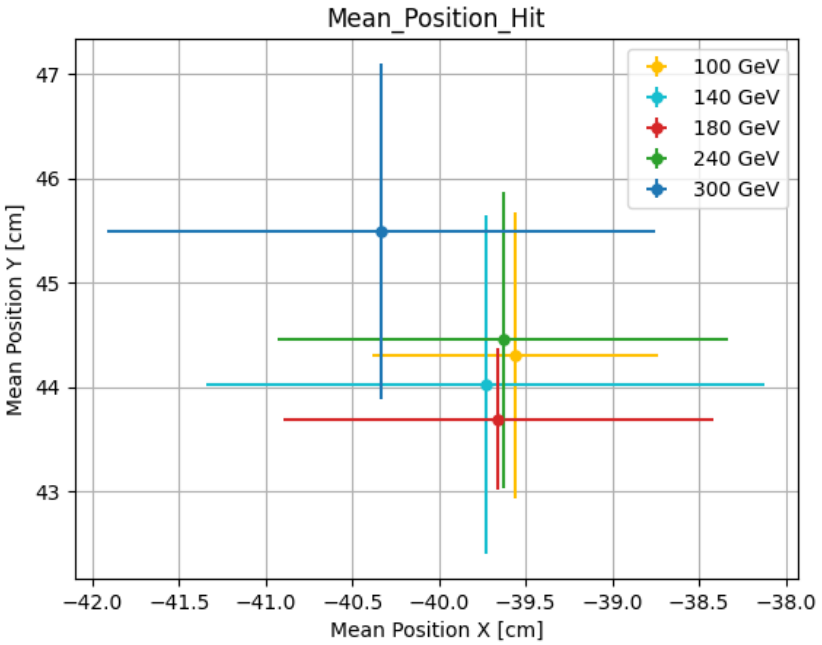

(a)

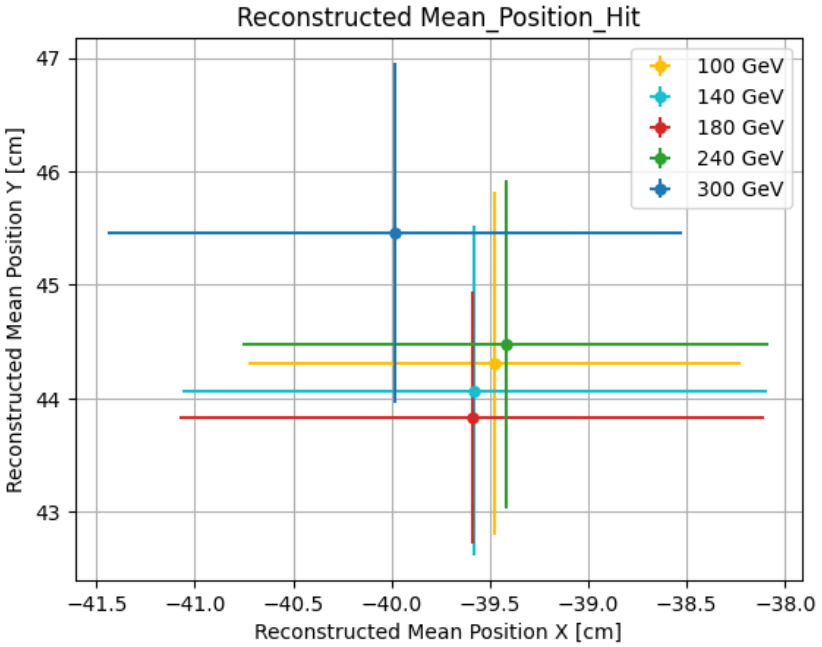

(b)

Figure 3.9: Pion beam parameters, in (a) are reported the positions and beam dimensions, while in (b) the reconstructed ones through the hadronic shower centroids.

was determined using a series of filtering steps: the hit positions in the first SciFi plane must have a positive QDC, then if multiple clusters of hits (consecutive series of hits) were present, only the largest cluster was selected. The mean position of the selected hits in first plane of SciFi was used as the *true* position.
The filtered hit positions in first plane of SciFi are shown for the 100 GeV configuration in Figure 3.10, while the others are reported in Appendix (Figure A.14 for 140 GeV, Figure A.15 for 180 GeV, Figure A.16 for 240 GeV, Figure A.17 for 300 GeV).

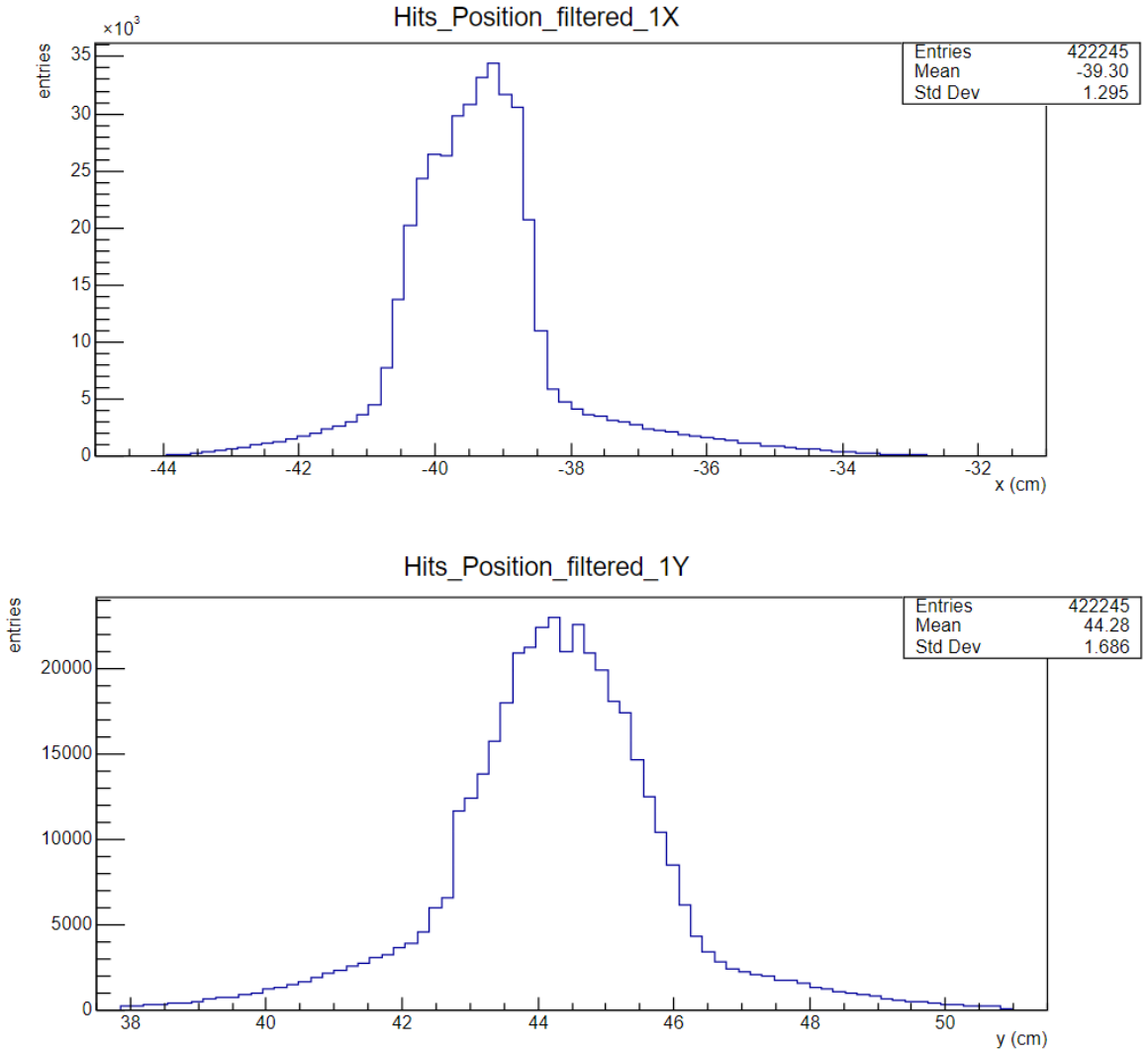

Figure 3.10: Filtered hits position in the first x and y plane of SciFi at 100 GeV.

The event-by-event displacement between the *true* position and the reconstructed posi-

tion is presented in Figure 3.11 for 100 GeV, while all the others energy configurations are in Appendix (Figure A.18 for 140 GeV, Figure A.19 for 180 GeV, Figure A.20 for 240 GeV, Figure A.21 for 300 GeV).
In Table 3.3 are summarized the differences between the *true* values and the reconstructed .

	Δx (mm)	Δy (mm)
100 GeV	0.6 $\pm$ 10.0	-0.5 $\pm$ 10.2
140 GeV	0.3 $\pm$ 9.0	-0.3 $\pm$ 9.1
180 GeV	0.0 $\pm$ 8.1	-0.9 $\pm$ 8.0
240 GeV	-0.6 $\pm$ 6.5	-0.4 $\pm$ 6.4
300 GeV	-1.0 $\pm$ 6.2	-0.1 $\pm$ 5.6

Table 3.3: Summarizing table with the Δ difference between the *true* value of the hit and the reconstructed one with shower direction in x and y direction at the different energy configurations.

The results indicate that the method achieves a resolution in reconstructing the pion position that ranges from 5 to 10 mm, depending on the energy of the incoming beam.

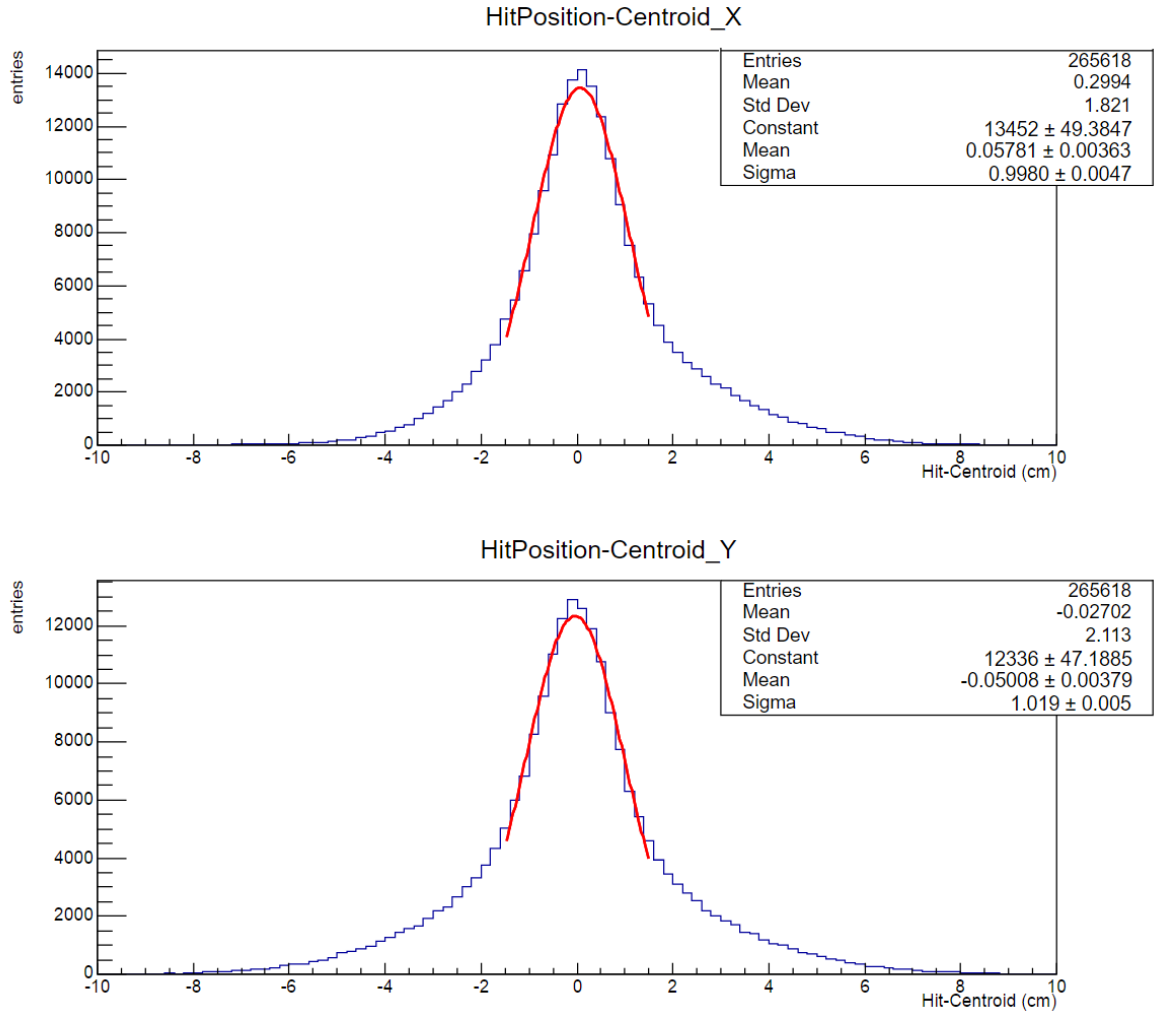

Figure 3.11: Difference between the *true* value of the hit and the reconstructed one with shower direction in first plane of SciFi at 100 GeV.

3.3 US tracking

Following the success achieved, the US detector was also included for tracking showers. This allowed for the inclusion of showers that do not end in SciFi, as well as those that start developing from the third plane of SciFi (ShowerStart = 3).
Since the US, as previously explained in Section 2.1.2, consists of directional bars read only horizontally, a different approach was required to calculate the centroid position along the x and y directions. Reference is made to Figure 3.12.

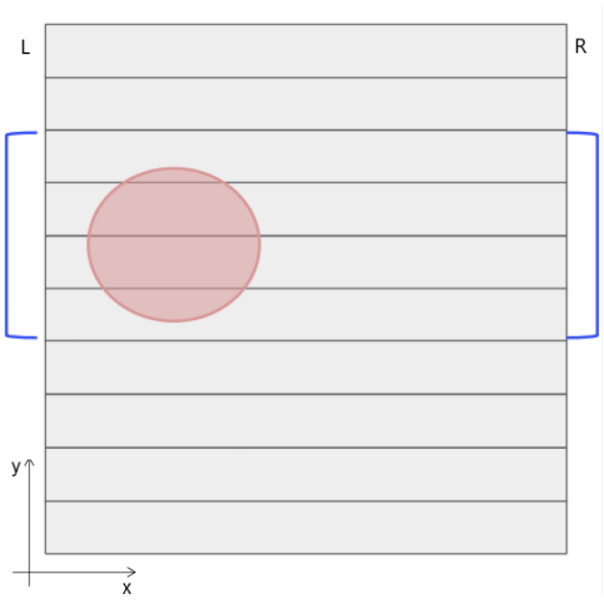

Figure 3.12: Schematic representation of a shower profile in US, where only horizontal bars are present.

To calculate the centroid in the y direction, a weighted average similar to that used for SciFi was employed. This was done by selecting only hits with positive QDC values and computing the weighted mean using the total QDC collected by each bar relative to the total QDC collected in US:

$$y = \sum_{N_{bars}} \frac{y_{bar} \cdot QDC_{bar}}{QDC_{total}}$$

where y_{bar} is the mean position of the bars in y direction.
For the x direction, a weighted mean was calculated based on the endpoints of each bar, where the weights were the total QDC collected on the left and right sides of the bar:

$$x = \frac{QDC_{left} \cdot x_{left} + QDC_{right} \cdot x_{right}}{QDC_{left} + QDC_{right}}$$

where x_{left} and x_{right} are the endpoint positions of the bar, in the x direction.
Points corresponding to US were then added to the fit.
Given the low spatial resolution of the US detector, errors assigned to these points were treated as measurements from a uniform distribution.
Specifically, the errors were calculated as $6/\sqrt{12}$ cm for y and $40/\sqrt{12}$ cm for x, where 6 and 40 are the dimension of the bars in y and half the dimension of the bars in x, respectively. Additionally, a ShowerEnd algorithm was implemented to exclude downstream planes from the fit if a centroid could not be determined in both x and y directions for a given plane.
The algorithm stops considering the shower if the total number of hits is less than 15.
This step was introduced to avoid including background noise or other spurious signals when calculating the shower direction.

The values obtained by incorporating US into the tracking for showers tagged with ShowerStart = 2 are reported in Table 3.4.

	Slope X (Rad·10^{-2})	Slope Y (Rad·10^{-2})
100 GeV	1.8 ± 4.2	0.2 ± 5.4
140 GeV	1.8 ± 3.8	0.4 ± 4.0
180 GeV	1.8 ± 3.5	0.2 ± 3.7
240 GeV	1.6 ± 3.1	0.0 ± 3.2
300 GeV	1.8 ± 3.0	-0.3 ± 3.0

Table 3.4: Slopes in x and y direction at the different energy configurations of showers tagged as ShowerStart = 2 after including US.

Comparing Table 3.4 with Table 3.2, the slope values are closer to zero, and the resolution (except for the 100 GeV case) has improved, indicating better accuracy. Then, showers tagged with ShowerStart = 3 were also analyzed, and the results are shown in Table 3.5.

The slope values are all consistent with zero and comparable to the ShowerStart = 2 case.
The resolution gets slightly worse but consistently, which is attributed to the increased influence of US and its low resolution.
This is more pronounced for ShowerStart = 3 since in these showers, only two SciFi planes can be used and the shower spans more deeply into US.
To verify the position reconstruction for ShowerStart = 3, a similar approach to the previous case was followed. Hits in the second SciFi plane were filtered using the same methodology: only hits with positive QDC values were considered, and if multiple clusters were present, only the one with the highest QDC was used.

	Slope X (Rad·10^{-2})	Slope Y (Rad·10^{-2})
100 GeV	0.9 ± 4.6	0.5 ± 4.7
140 GeV	1.3 ± 4.7	0.2 ± 4.7
180 GeV	1.9 ± 4.5	-0.1 ± 4.6
240 GeV	2.2 ± 4.2	-0.1 ± 4.0
300 GeV	2.4 ± 4.0	-0.4 ± 4.0

Table 3.5: Slopes in x and y direction at the different energy configurations of showers tagged as ShowerStart = 3.

The mean position of the largest cluster, after filtering (as described before), was used to determine the *true* pion position in the second SciFi plane.
To ensure consistency, the displacement between the *true* hit positions in the first and second planes was checked.
If this displacement was less than 0.5 cm in both the x and y directions, the difference between the *true* position and the reconstructed position in the second SciFi plane was calculated. Here, the reconstructed position refers to the intersection of the shower direction with the second SciFi plane.
The measured differences between *true* and reconstructed for ShowerStart = 3 across different energy configurations are summarized in Table 3.6 and in Figure 3.13 can be seen for 100 GeV configuration, while all the others are reported in Appendix (Figure A.22 for 140 GeV, Figure A.23 for 180 GeV, Figure A.24 for 240 GeV, Figure A.25 for 300 GeV).

	Δx (mm)	Δy (mm)
100 GeV	1.1 ± 11.5	0.2 ± 11.4
140 GeV	0.7 ± 10.3	-0.2 ± 10.3
180 GeV	0.8 ± 9.5	-0.9 ± 10.0
240 GeV	0.9 ± 8.5	-0.2 ± 8.9
300 GeV	0.4 ± 8.2	-0.5 ± 8.3

Table 3.6: Summarizing table with the difference between *true* and measured positions by the hadronic shower reconstruction method in x and y direction at the different energy configurations, for ShowerStart = 3.

The mean displacement values in both x and y directions are consistently close to zero, indicating no bias in the reconstruction method. Furthermore, the standard deviations show a clear trend of improvement with increasing energy, reflecting the reduced uncertainty in position determination at higher energies.

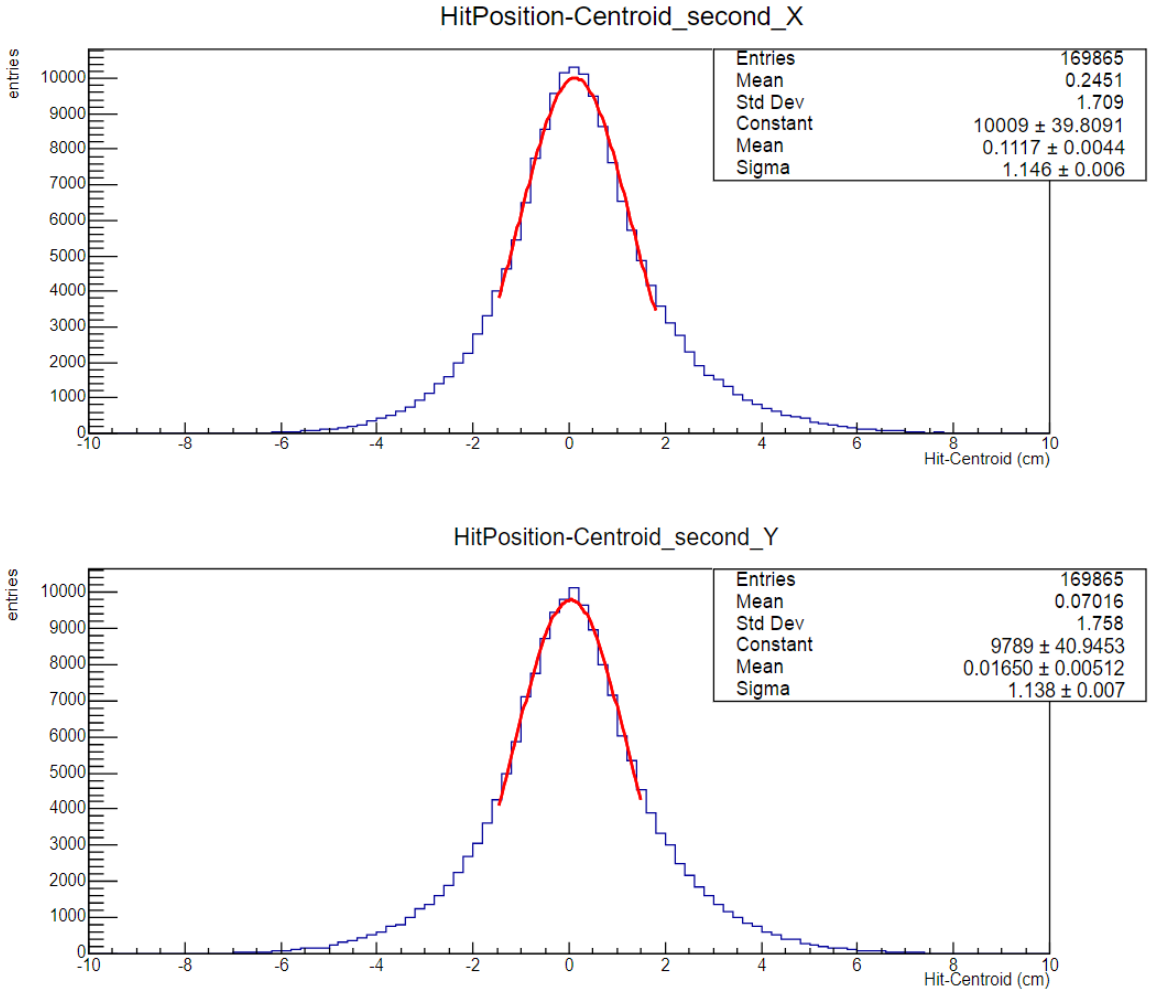

Figure 3.13: Difference between the *true* value of the hit and the reconstructed one with shower direction in second plane of SciFi at 100 GeV.

These results validate the methodology's robustness and its ability to achieve precision, below the centimeter, in shower position reconstruction, even considering the inclusion of US, which inherently has a lower spatial resolution.

The achieved spatial accuracy of the reconstruction method ranges up to 11 mm. So, considering a positional uncertainty of approximately 10 mm, the resulting uncertainty in the slope is estimated to be around 30 mRad.
This value derives from the ratio between the uncertainty in the transverse plane (xy) and the shower depth, which can be approximated to the 30 cm length of the detector used for tracking the shower centroids.

The energy of the incoming neutrino can be derived through the relation:

$$E_\nu \simeq E_{shower}\left(1 + \frac{\theta_{shower}}{\theta_\mu}\right)$$

where θ_{shower} and θ_μ are the directions of the shower and of the muon relative to the incoming neutrino direction, under the small-angle approximation.
The impact of the results can be further quantified by evaluating the uncertainty in the energy resolution of the neutrino as follows:

$$\delta E_\nu \simeq \frac{E_{shower}}{\theta_\mu}\delta\theta_{shower}$$

This resolution depends both on the energy measurement of the hadronic shower and on the precision in determining the muon direction.

Overall, these findings confirm that the adopted reconstruction approach provides reliable and precise information about the pion position, paving the way for accurate directional analyses of hadronic showers. This is significant for improving the understanding of detector performance, with direct implications for the neutrino energy reconstruction capabilities in the SND@LHC experiment.

Conclusions

The SND@LHC experiment, located in the TI18 tunnel, aims to study all three neutrino flavors in an unprecedented energy range up to 1 TeV, opening a new window of exploration in high-energy neutrino physics.

The primary goal of this thesis work was to analyze and reconstruct hadronic showers using test beam data, focusing on characterizing their direction and position, evaluating the accuracy of the reconstruction methods. The achieved spatial accuracy of the reconstruction method ranges from 5 mm to 11 mm, depending on the shower energy. Considering a positional uncertainty of approximately 1 cm, the resulting uncertainty in the slope is estimated to be around 30 mRad.

While these results are promising, they represent a preliminary study that requires further validation and refinement through Monte Carlo simulations.

In conclusion, this work provides an important first step in understanding the performance of hadronic shower reconstruction for SND@LHC. The developed methods and obtained results lay the groundwork for future studies. This will be essential for fully exploiting the detector capabilities, enhancing the precision of neutrino energy and direction measurements in this energy regime.

Appendix A

Appendix

The following section presents all the additional plots that were omitted from the main text to enhance readability. These plots provide further insights and complement the analyses discussed in the thesis.

Centroid positions

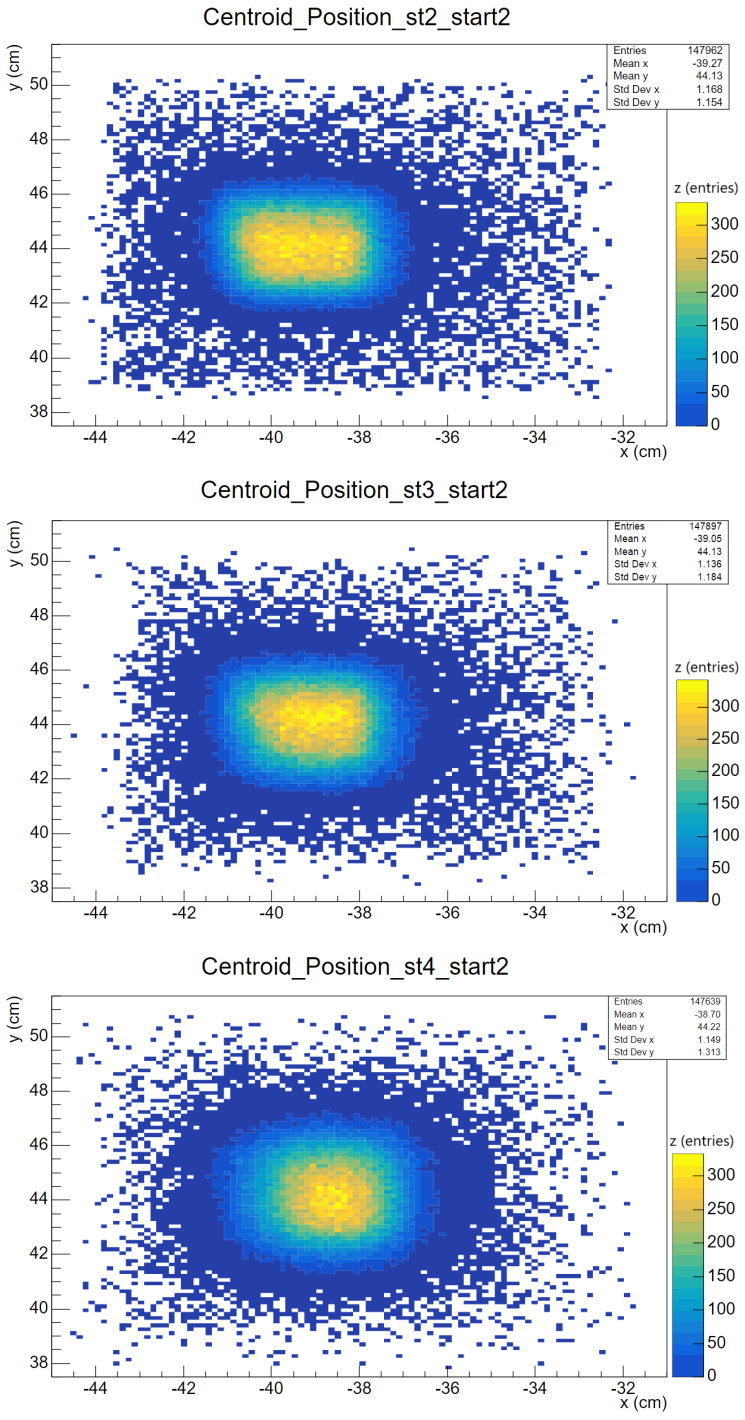

Figure A.1: Display of the development of the centroid positions for 140 GeV pion beams, in events tagged with ShowerStart = 2. The centroid positions in SciFi stations 2 (top), 3 (middle), and 4 (bottom) are shown.

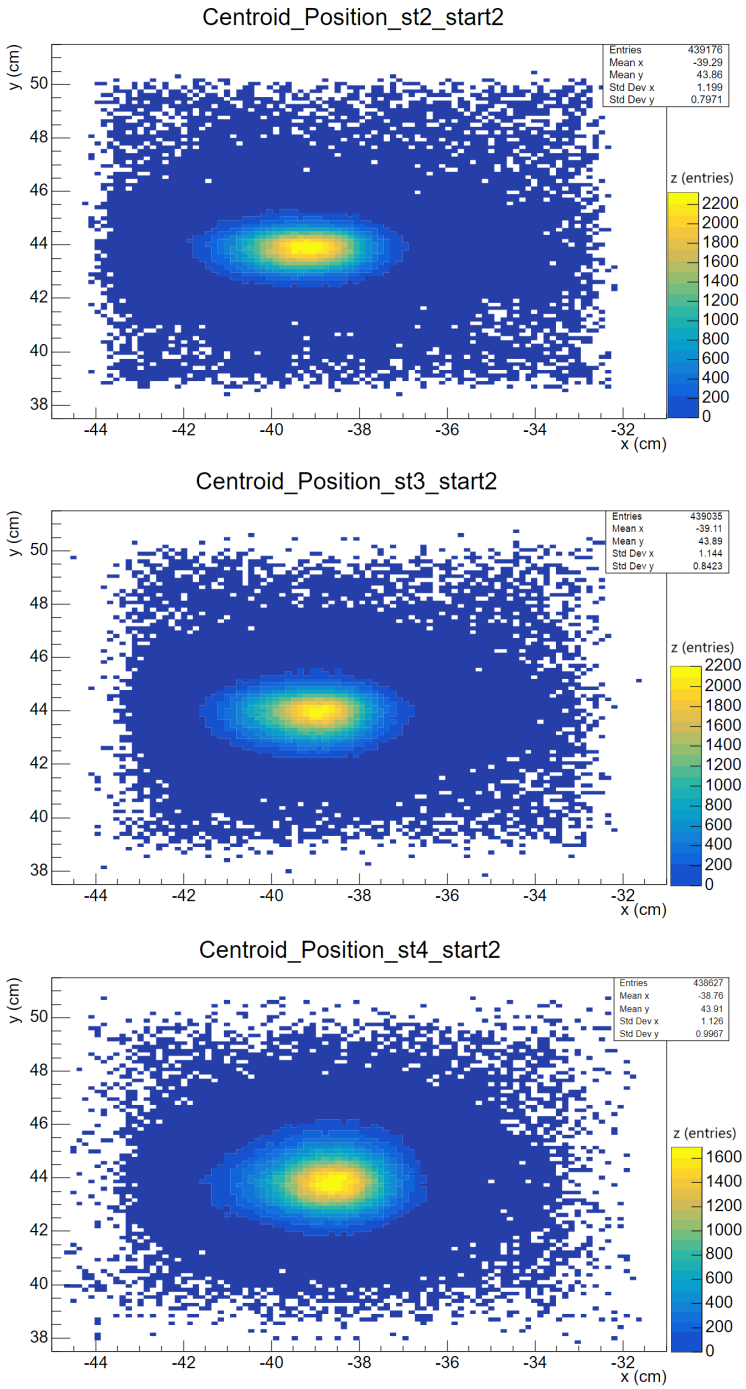

Figure A.2: Display of the development of the centroid positions for 180 GeV pion beams, in events tagged with ShowerStart = 2. The centroid positions in SciFi stations 2 (top), 3 (middle), and 4 (bottom) are shown.

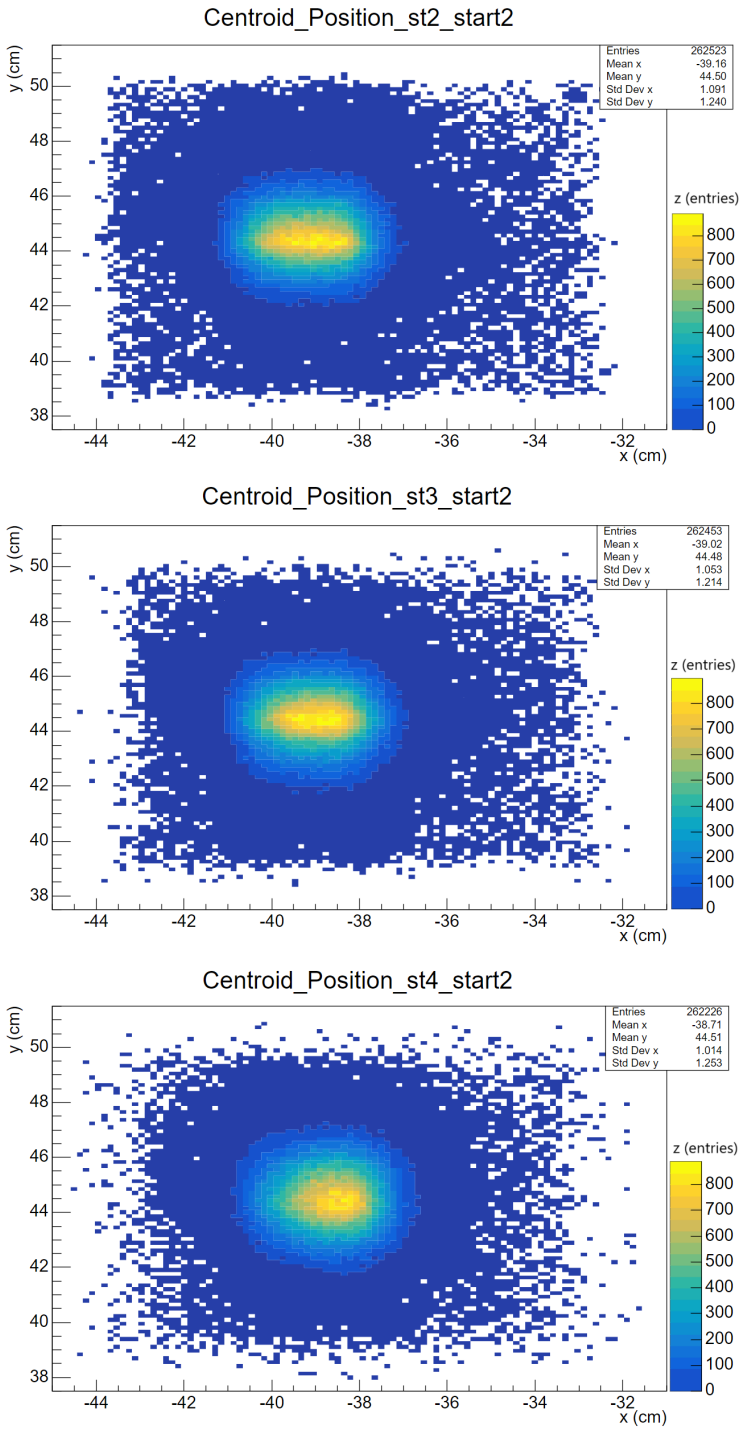

Figure A.3: Display of the development of the centroid positions for 240 GeV pion beams, in events tagged with ShowerStart = 2. The centroid positions in SciFi stations 2 (top), 3 (middle), and 4 (bottom) are shown.

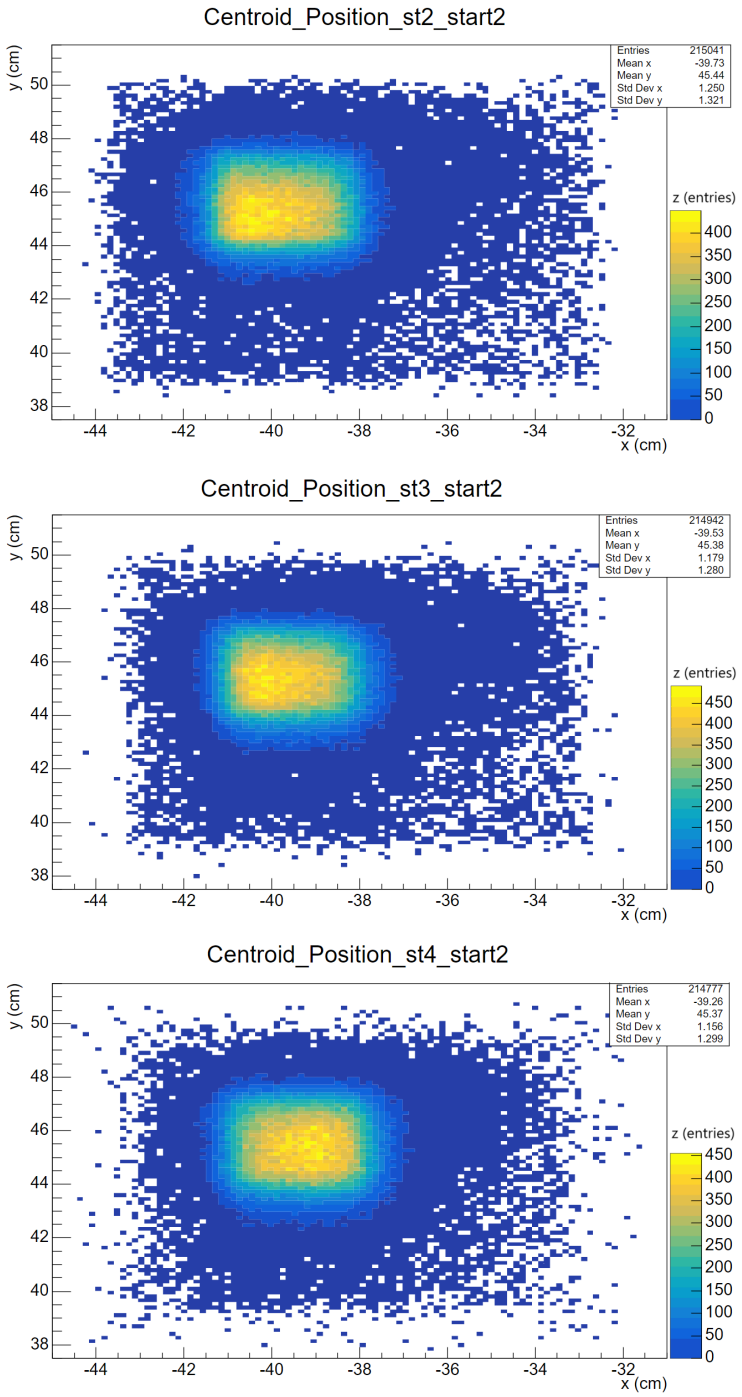

Figure A.4: Display of the development of the centroid positions for 300 GeV pion beams, in events tagged with ShowerStart = 2. The centroid positions in SciFi stations 2 (top), 3 (middle), and 4 (bottom) are shown.

Slope

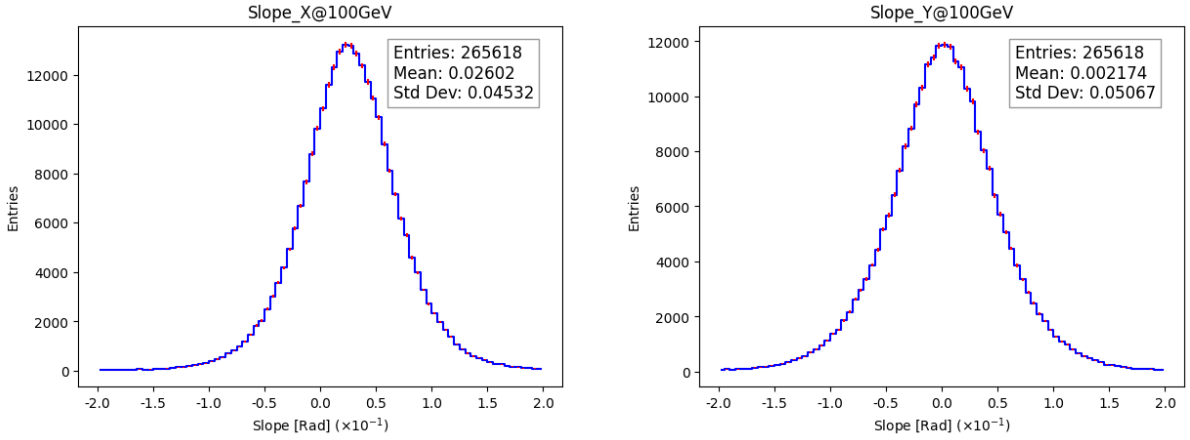

(a) (b)

Figure A.5: Slope at 100 GeV, in (a) x-direction, in (b) y-direction.

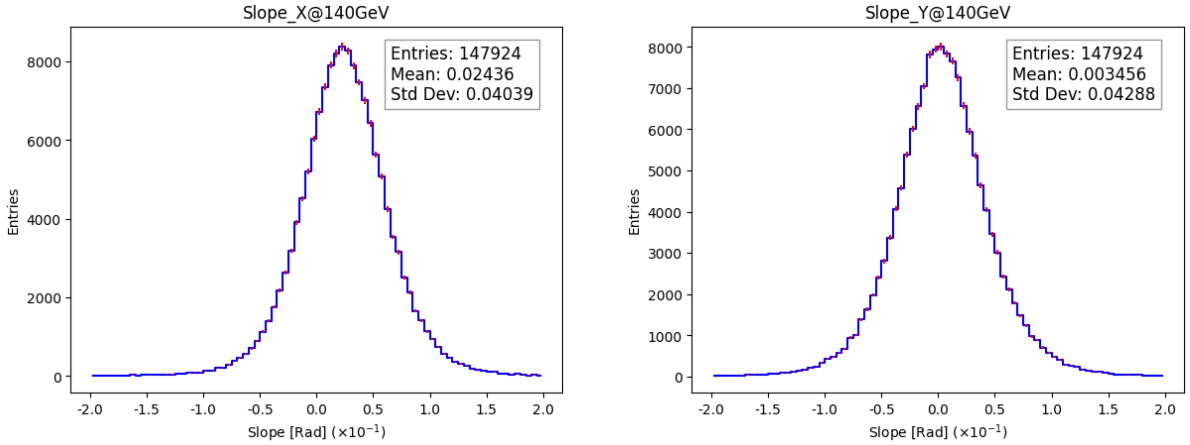

(a) (b)

Figure A.6: Slope at 140 GeV, in (a) x-direction, in (b) y-direction.

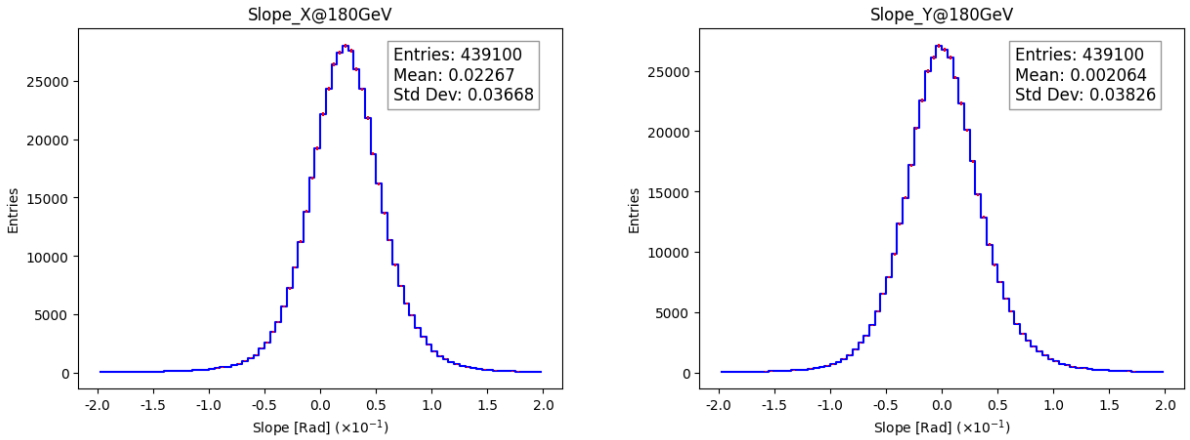

(a) (b)

Figure A.7: Slope at 180 GeV, in (a) x-direction, in (b) y-direction.

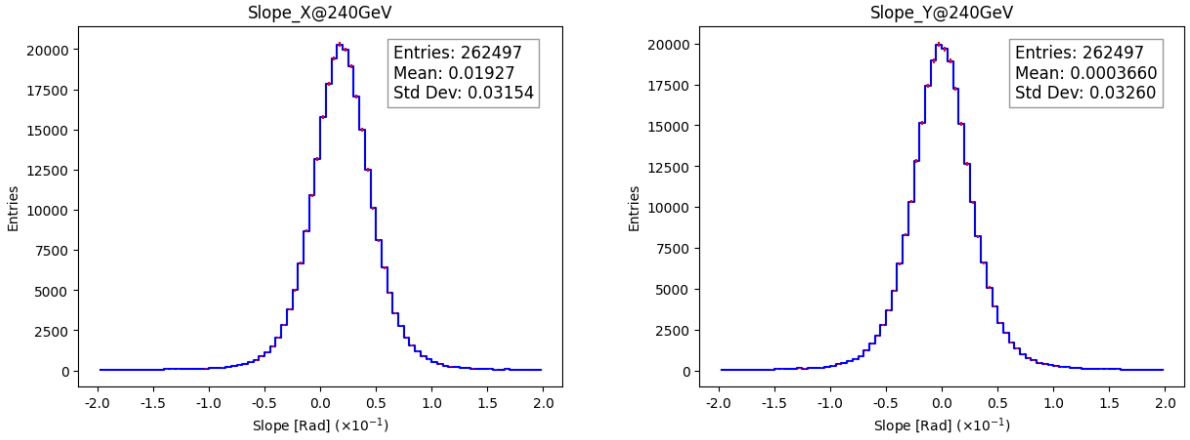

(a) (b)

Figure A.8: Slope at 240 GeV, in (a) x-direction, in (b) y-direction.

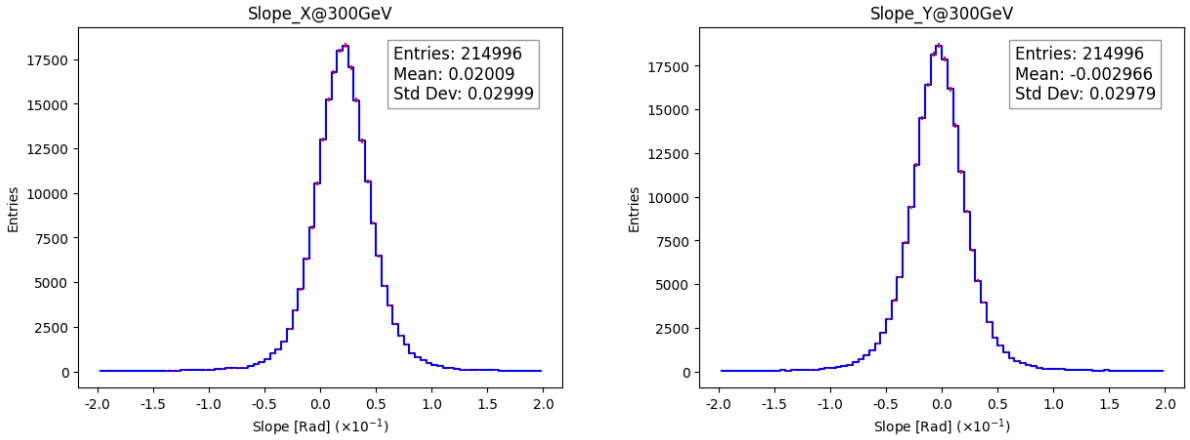

(a) (b)

Figure A.9: Slope at 300 GeV, in (a) x-direction, in (b) y-direction.

Hits position in first plane of SciFi

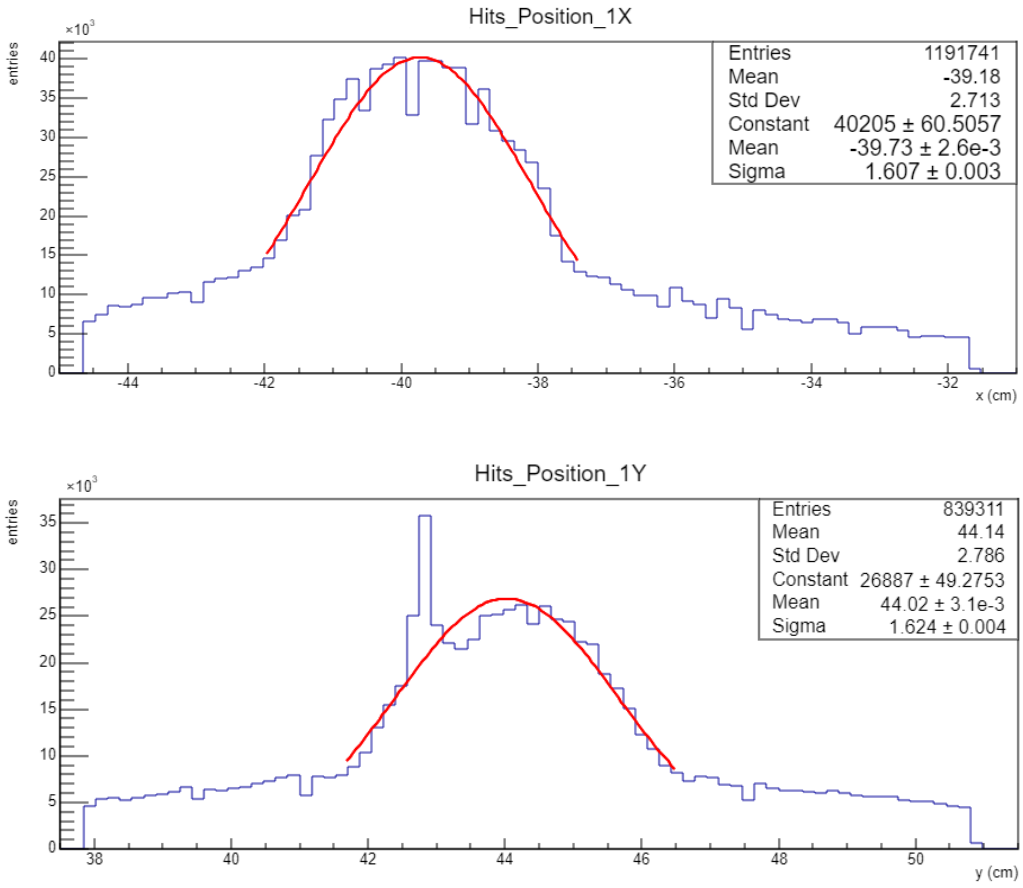

Figure A.10: Hits position in the first x and y plane of SciFi at 140 GeV.

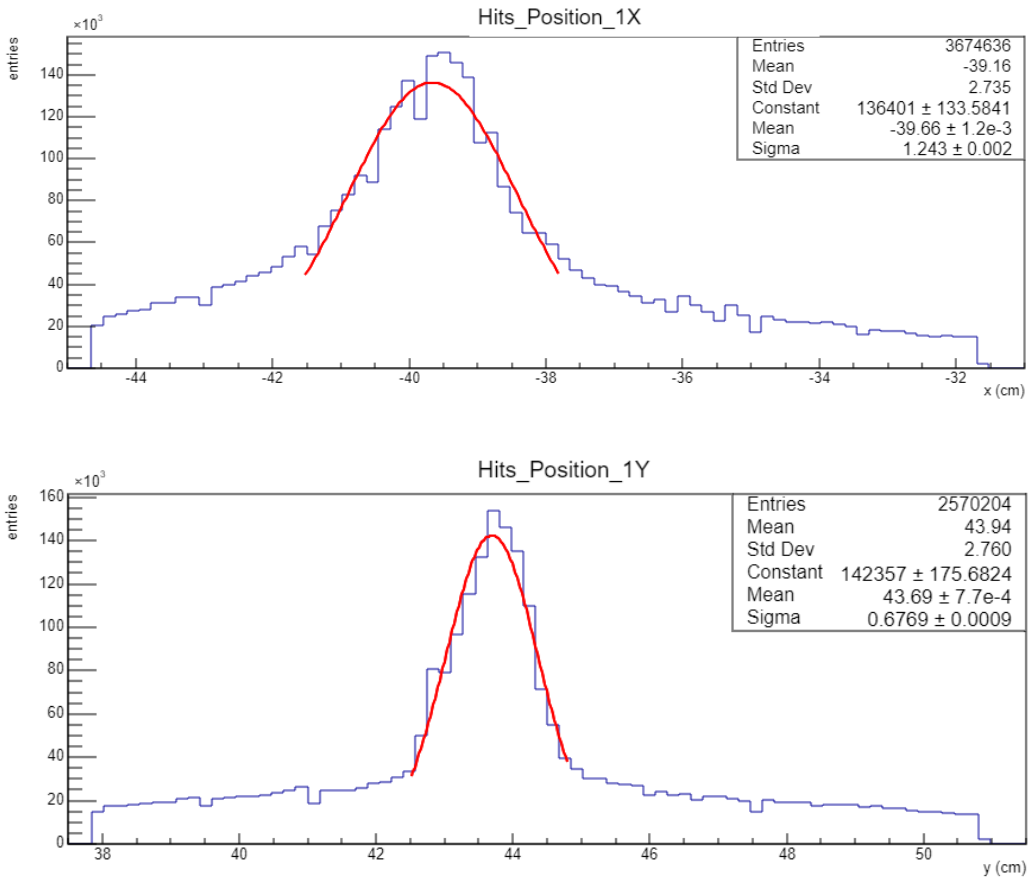

Figure A.11: Hits position in the first x and y plane of SciFi at 180 GeV.

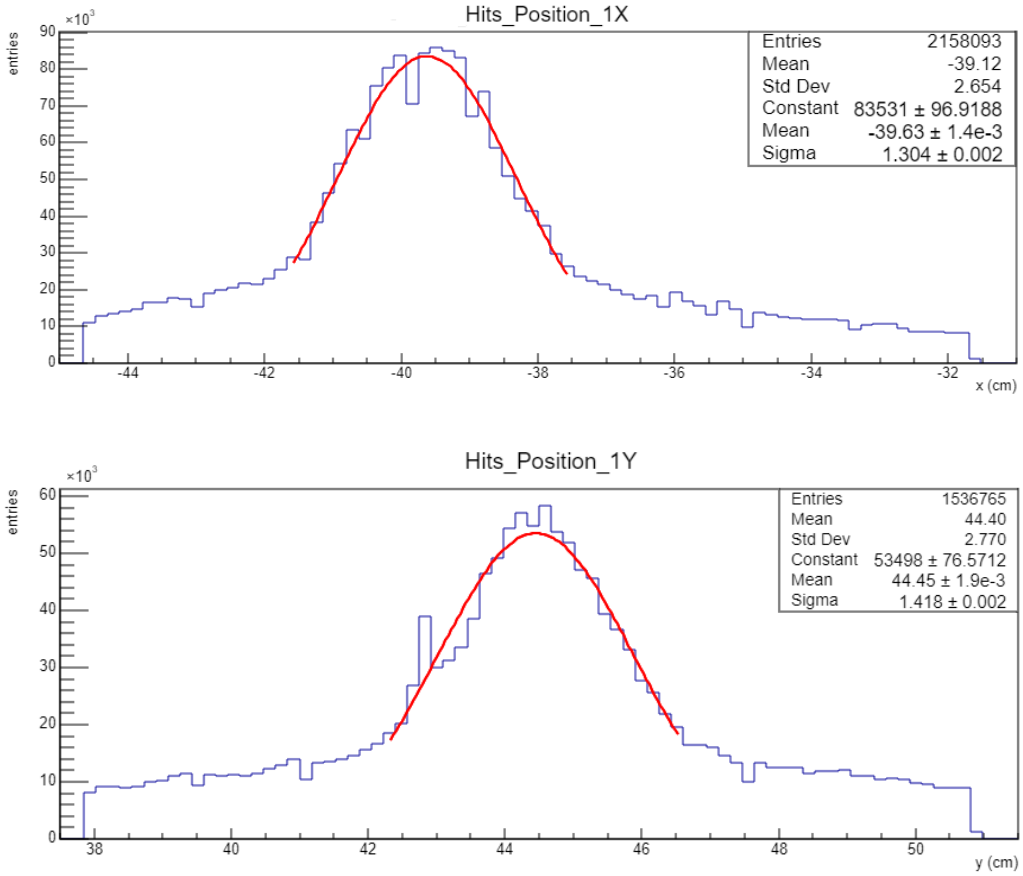

Figure A.12: Hits position in the first x and y plane of SciFi at 240 GeV.

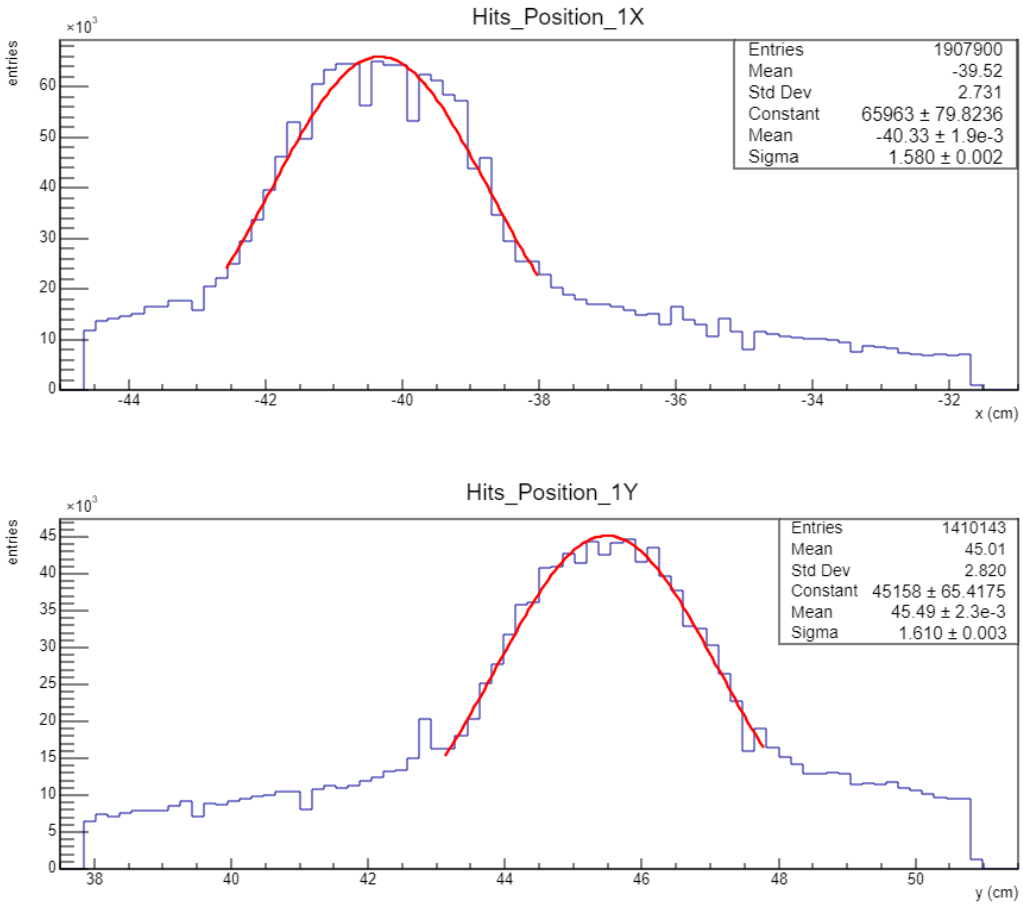

Figure A.13: Hits position in the first x and y plane of SciFi at 300 GeV.

Filtered hits in first SciFi plane

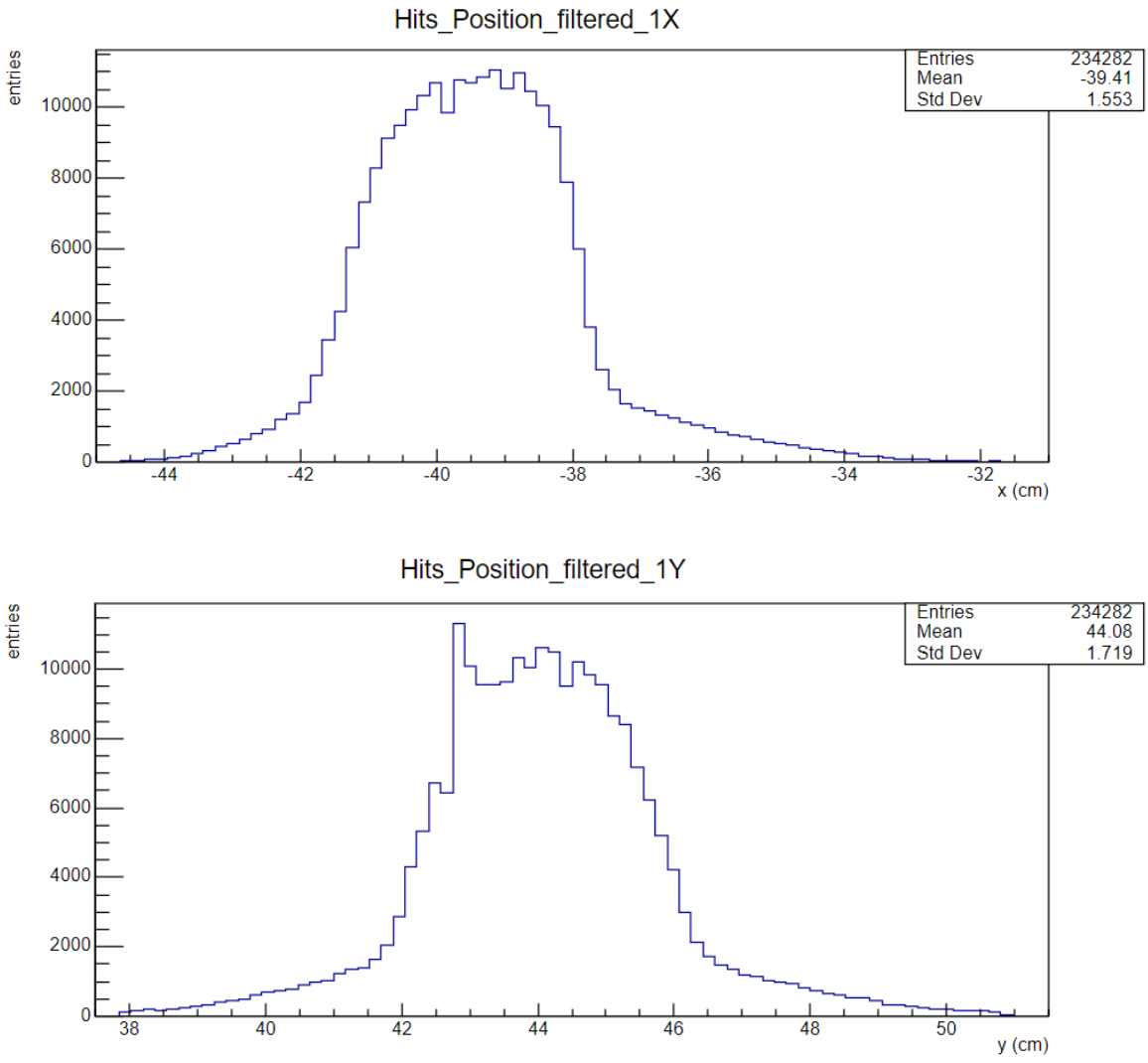

Figure A.14: Filtered hits position in the first x and y plane of SciFi at 140 GeV.

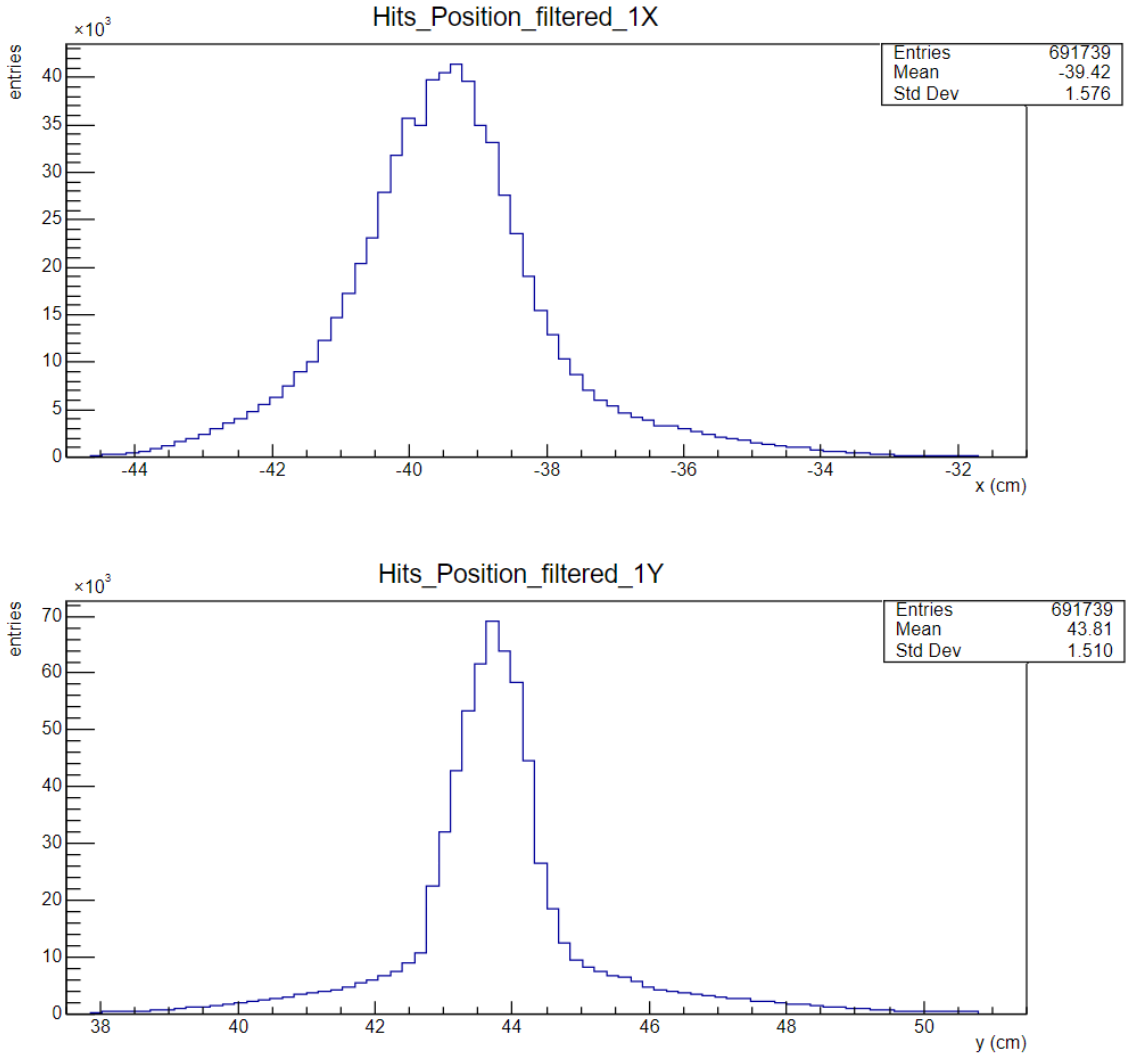

Figure A.15: Filtered hits position in the first x and y plane of SciFi at 180 GeV.

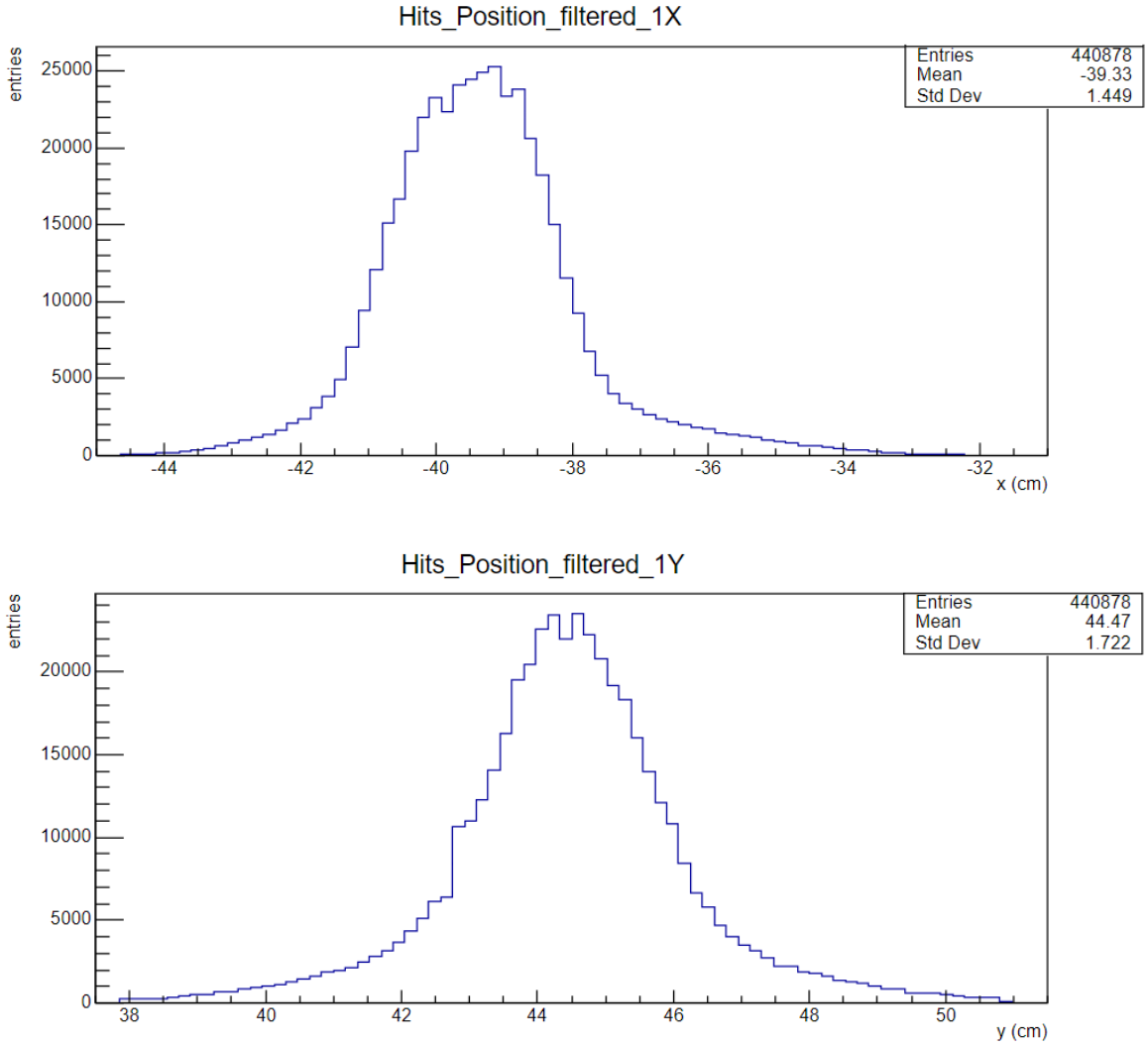

Figure A.16: Filtered hits position in the first x and y plane of SciFi at 240 GeV.

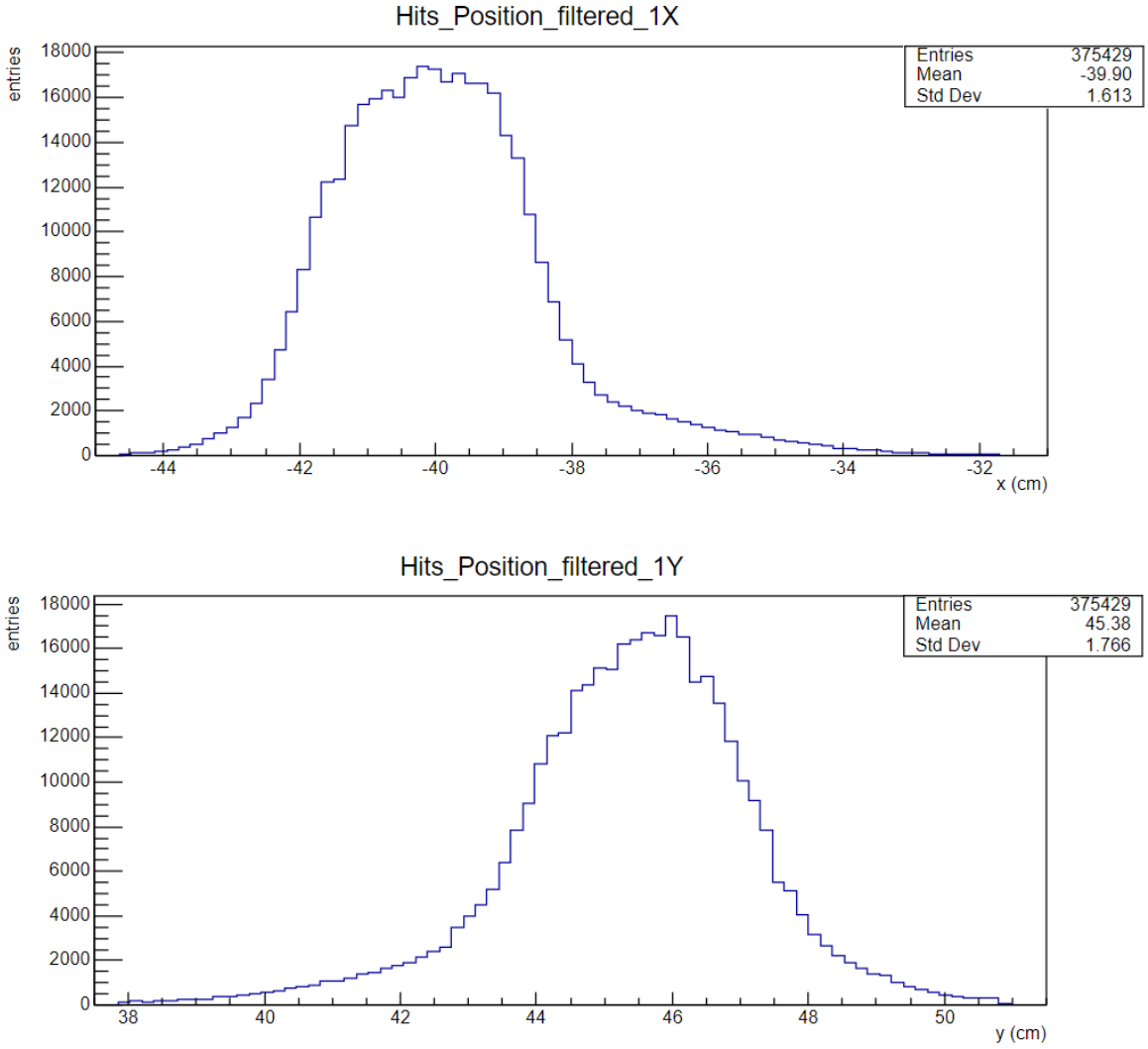

Figure A.17: Filtered hits position in the first x and y plane of SciFi at 300 GeV.

Difference *true* value and reconstructed in first SciFi plane

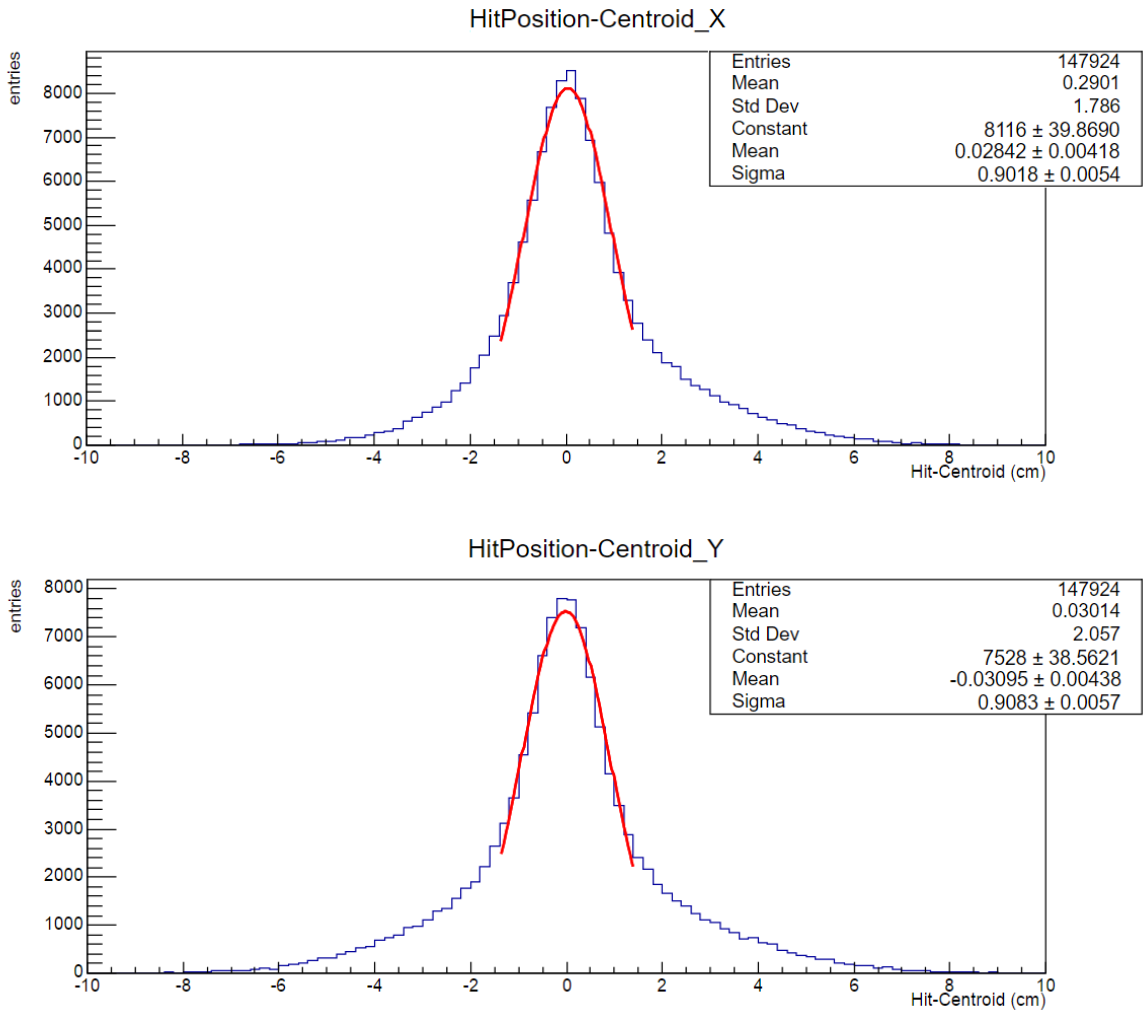

Figure A.18: Difference between the *true* value of the hit and the reconstructed one with shower direction in first plane of SciFi at 140 GeV.

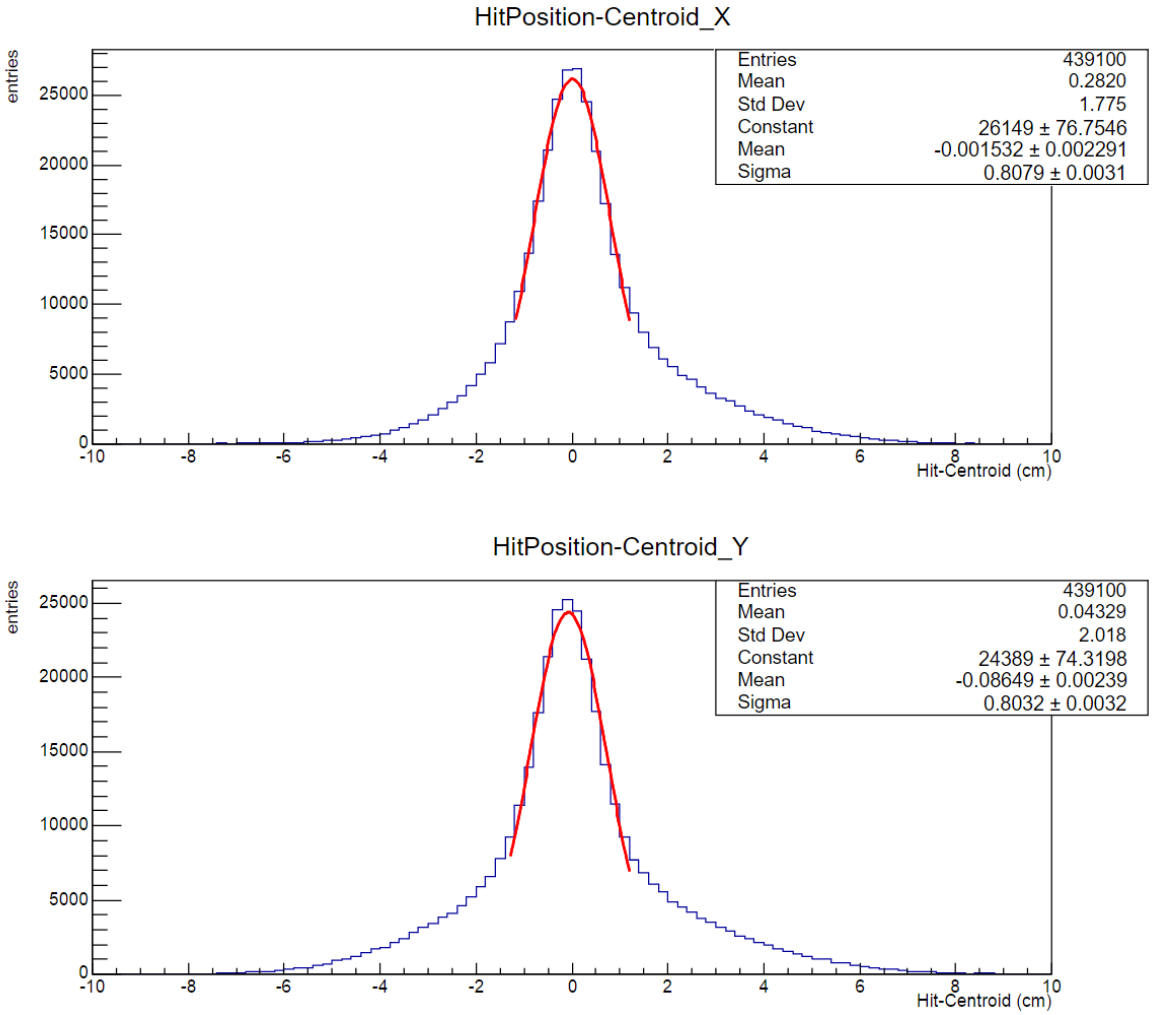

Figure A.19: Difference between the *true* value of the hit and the reconstructed one with shower direction in first plane of SciFi at 180 GeV.

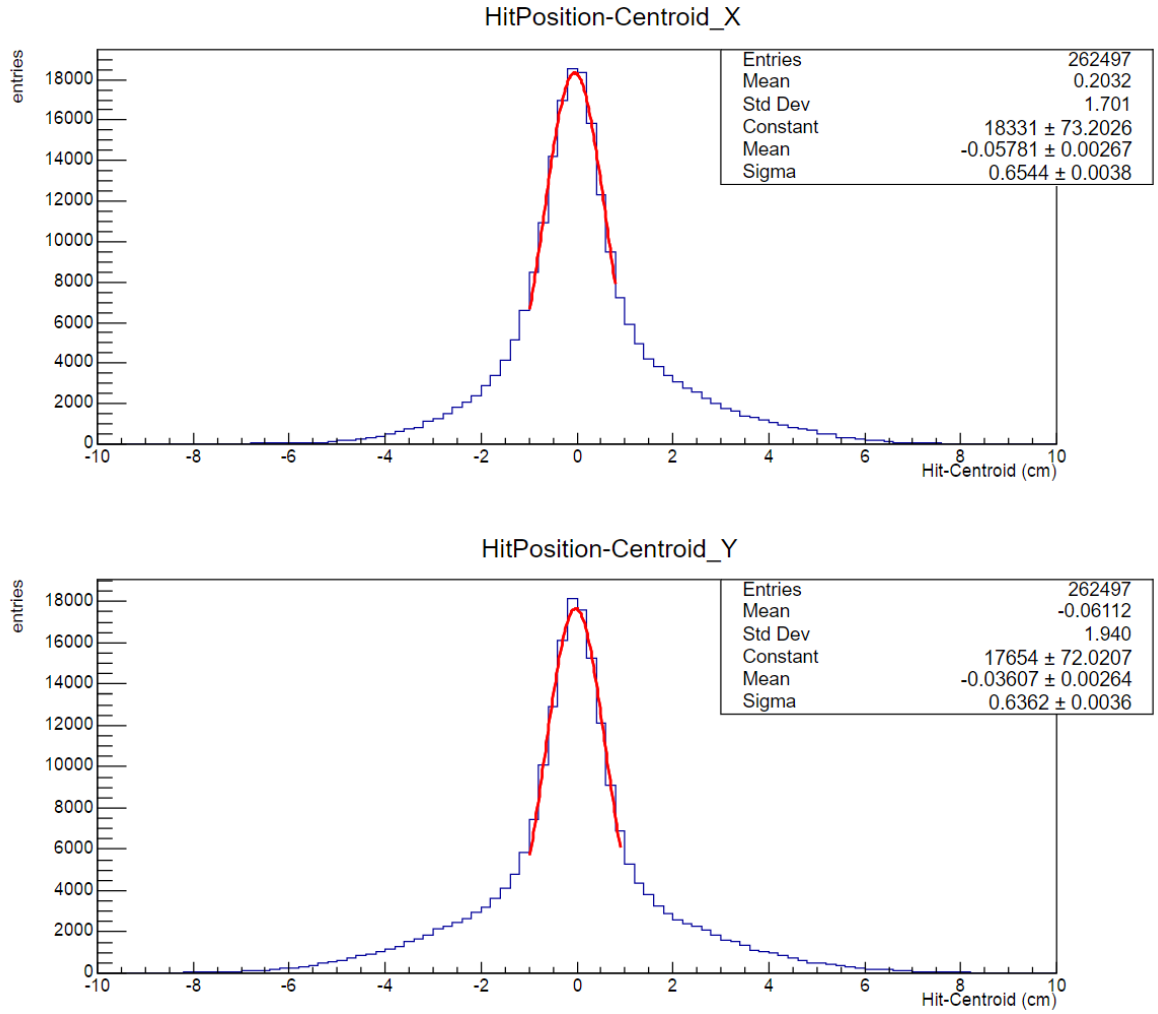

Figure A.20: Difference between the *true* value of the hit and the reconstructed one with shower direction in first plane of SciFi at 240 GeV.

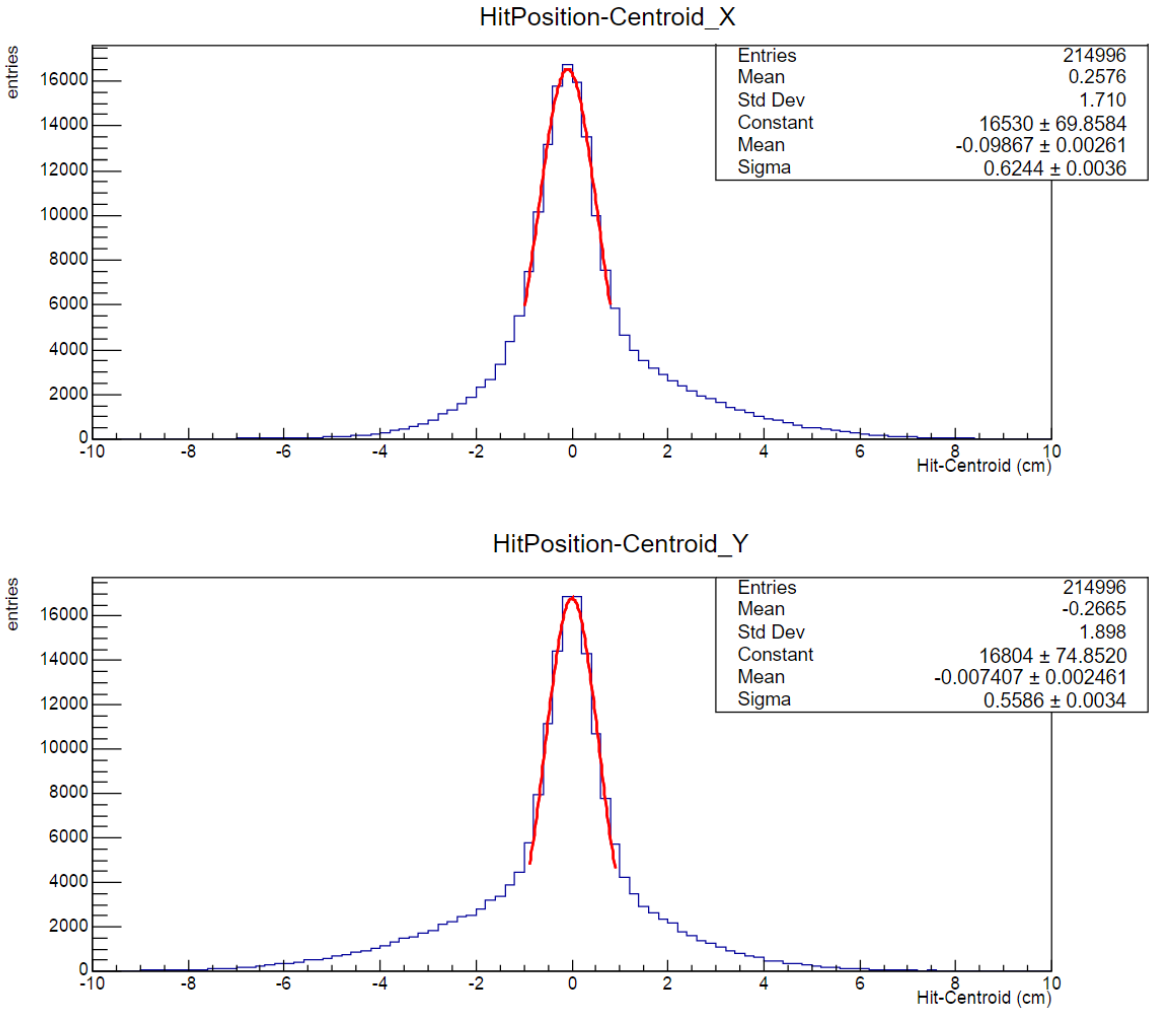

Figure A.21: Difference between the *true* value of the hit and the reconstructed one with shower direction in first plane of SciFi at 300 GeV.

Difference *true* value and reconstructed in second SciFi plane

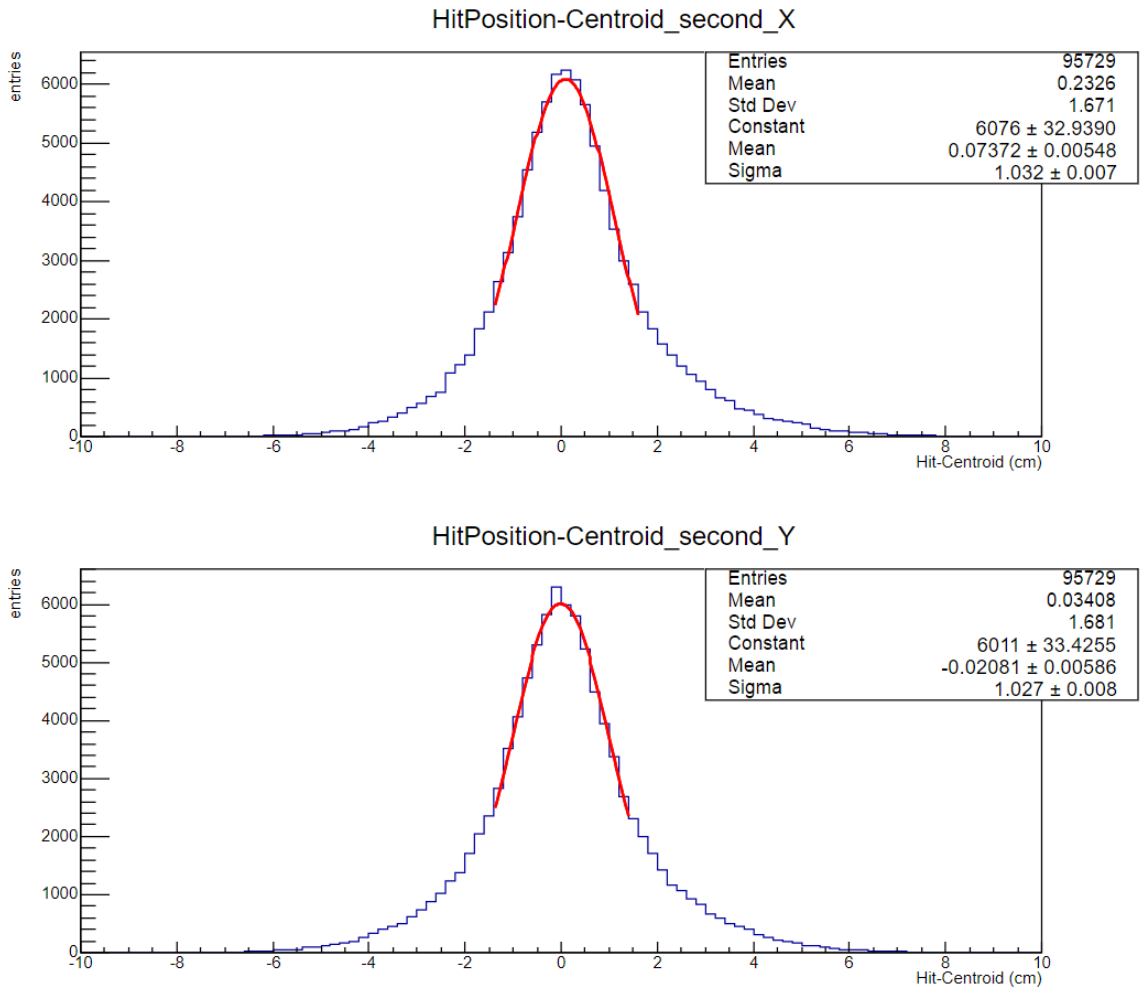

Figure A.22: Difference between the *true* value of the hit and the reconstructed one with shower direction in second plane of SciFi at 140 GeV.

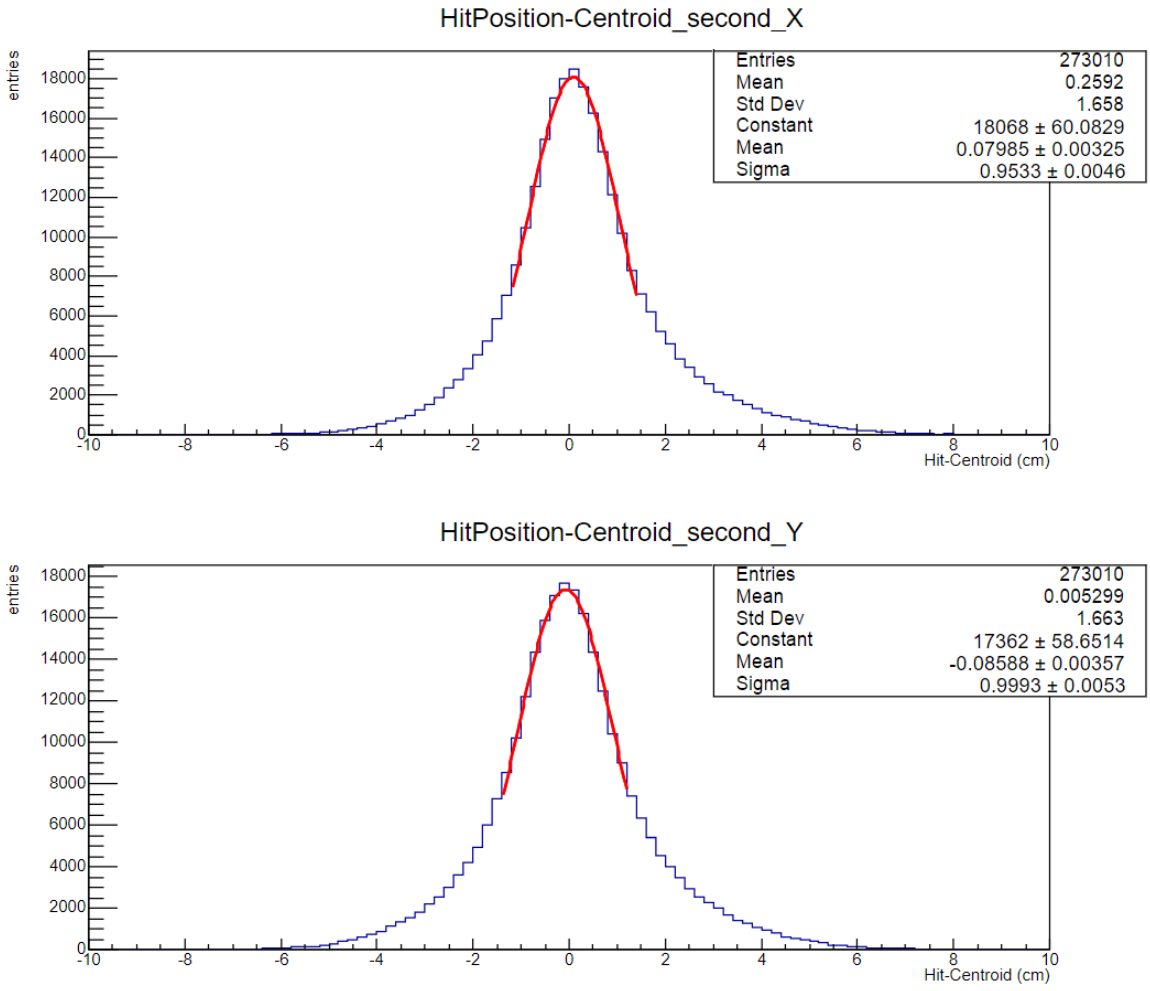

Figure A.23: Difference between the *true* value of the hit and the reconstructed one with shower direction in second plane of SciFi at 180 GeV.

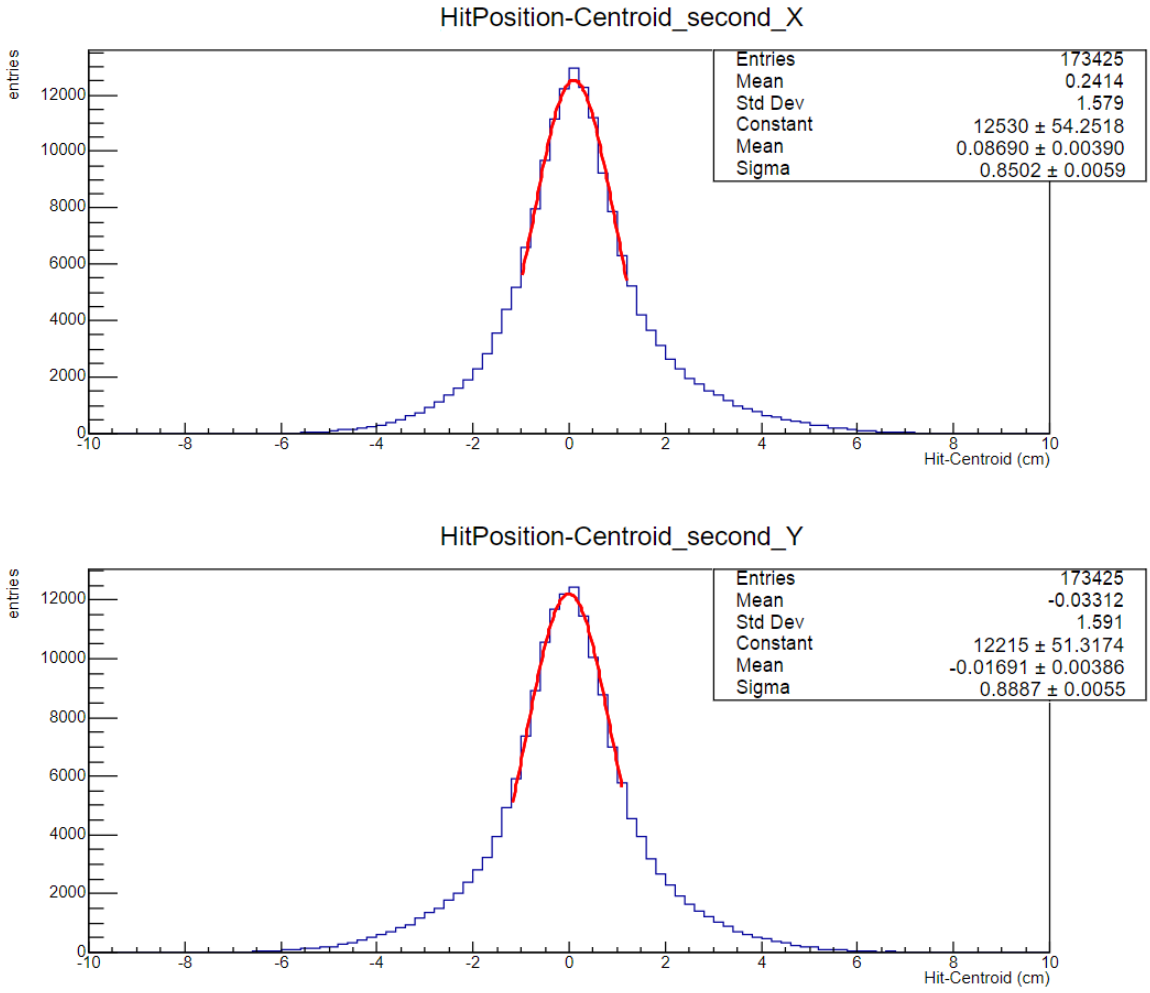

Figure A.24: Difference between the *true* value of the hit and the reconstructed one with shower direction in second plane of SciFi at 240 GeV.

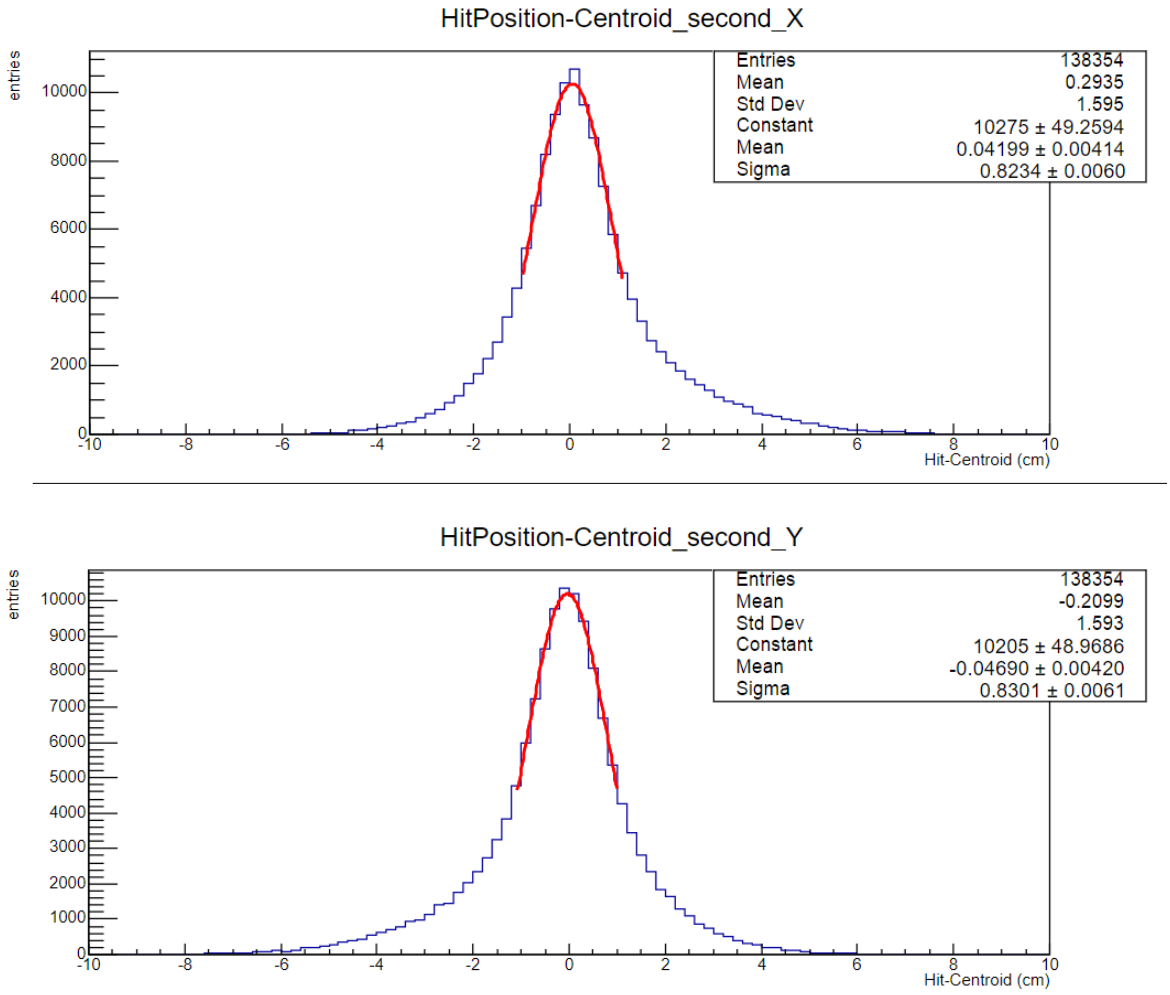

Figure A.25: Difference between the *true* value of the hit and the reconstructed one with shower direction in second plane of SciFi at 300 GeV.

Bibliography

[1] W. Pauli. "Dear radioactive ladies and gentlemen". In: *Phys. Today* 31N9 (1978), p. 27. URL: https://inspirehep.net/literature/45177.

[2] C. L. Cowan et al. "Detection of the Free Neutrino: a Confirmation". In: *Science* 124.3212 (1956), pp. 103–104. DOI: 10.1126/science.124.3212.103. URL: https://www.science.org/doi/abs/10.1126/science.124.3212.103.

[3] M. Goldhaber, L. Grodzins, and A. W. Sunyar. "Helicity of Neutrinos". In: *Phys. Rev.* (1958). DOI: 10.1103/PhysRev.109.1015. URL: https://link.aps.org/doi/10.1103/PhysRev.109.1015.

[4] Giorgio Bendiscioli. "Fenomeni radioattivi. Dai nuclei alle stelle". In: (2012). URL: https://link.springer.com/book/10.1007/978-88-470-5453-0.

[5] Francesco Renga. "Experimental searches for muon decays beyond the Standard Model". In: (2019). DOI: https://doi.org/10.1016/j.revip.2019.100029. URL: https://www.sciencedirect.com/science/article/pii/S2405428318300601.

[6] INFN-Roma. "Neutrini". In: (). URL: https://www.roma1.infn.it/people/longo/fnsn/capitolo6c.pdf.

[7] T. Thompson. "Discovery of the Muon Neutrino". In: (). URL: https://indico.cern.ch/event/402462/attachments/806290/1104933/JournalClub.pdf.

[8] K. Kodama et al. "Observation of tau neutrino interactions". In: (2001). DOI: 10.1016/s0370-2693(01)00307-0. URL: http://dx.doi.org/10.1016/S0370-2693(01)00307-0.

[9] N. Agafonova et al. "Final Results of the OPERA Experiment on ν_τ Appearance in the CNGS Neutrino Beam". In: *Phys. Rev. Lett.* 120 (21 May 2018), p. 211801. DOI: 10.1103/PhysRevLett.120.211801. URL: https://link.aps.org/doi/10.1103/PhysRevLett.120.211801.

[10] Matthew D. Schwartz. "Quantum field theory and the Standard Model". In: (2014).

[11] M.C. Gonzalez-Garcia and M. Yokoyama. "Neutrino Masses, Mixing, and Oscillations". In: (2019). URL: https://pdg.lbl.gov/2019/reviews/rpp2019-rev-neutrino-mixing.pdf.

[12] J. A. Formaggio and G. P. Zeller. "From eV to EeV: Neutrino cross sections across energy scales". In: (2012). DOI: 10.1103/RevModPhys.84.1307. URL: https://link.aps.org/doi/10.1103/RevModPhys.84.1307.

[13] SLAC-NATIONAL-ACCELERATOR-LABORATORY. "Neutrino Physics". In: (). URL: https://sites.slac.stanford.edu/neutrino/research/neutrino-oscillations.

[14] Carlo Giunti and Chung W. Kim. "Fundamentals of Neutrino Physics and Astrophysics". In: (2007). DOI: 10.1093/acprof:oso/9780198508717.003.0006. URL: https://doi.org/10.1093/acprof:oso/9780198508717.003.0006.

[15] Andreas Aste. "Weyl, Majorana and Dirac Fields from a Unified Perspective". In: (2016). DOI: 10.3390/sym8090087. URL: https://www.mdpi.com/2073-8994/8/9/87.

[16] Frank T. Avignone, Steven R. Elliott, and Jonathan Engel. "Double beta decay, Majorana neutrinos, and neutrino mass". In: *Rev. Mod. Phys.* 80 (2 Apr. 2008), pp. 481–516. DOI: 10.1103/RevModPhys.80.481. URL: https://link.aps.org/doi/10.1103/RevModPhys.80.481.

[17] Asli M Abdullahi et al. "The present and future status of heavy neutral leptons". In: (2023). DOI: 10.1088/1361-6471/ac98f9. URL: http://dx.doi.org/10.1088/1361-6471/ac98f9.

[18] Ubaldo Dore and Lucia Zanello. *Bruno Pontecorvo and neutrino physics*. 2010. URL: https://arxiv.org/abs/0910.1657.

[19] Tanju Gleisberg et al. "SHERPA 1., a proof-of-concept version". In: (2004). DOI: 10.1088/1126-6708/2004/02/056. URL: https:dx.doi.org/10.1088/1126-6708/2004/02/056.

[20] Boyarsky et al. "Searches for new physics at SND@LHC". In: (2022). DOI: 10.1007/JHEP03(2022)006. URL: https://doi.org/10.1007/JHEP03(2022)006.

[21] G. Acampora et al. "SND@LHC: the scattering and neutrino detector at the LHC". In: (2024). DOI: 10.1088/1748-0221/19/05/p05067. URL: http://dx.doi.org/10.1088/1748-0221/19/05/P05067.

[22] N Beni et al. "Physics potential of an experiment using LHC neutrinos". In: (2019). DOI: 10.1088/1361-6471/ab3f7c. URL: https://dx.doi.org/10.1088/1361-6471/ab3f7c.

[23] Giulia Paggi. "Vetoing charged particles for neutrino detection at the LHC". In: *Nuclear Instruments and Methods in Physics Research Section A: Accelerators, Spectrometers, Detectors and Associated Equipment* (2024). DOI: https://doi.org/10.1016/j.nima.2024.169928. URL: https://www.sciencedirect.com/science/article/pii/S0168900224008544.

[24] R. Albanese et al. “Observation of Collider Muon Neutrinos with the SND@LHC Experiment”. In: *Phys. Rev. Lett.* (2023). DOI: 10.1103/PhysRevLett.131.031802. URL: https://link.aps.org/doi/10.1103/PhysRevLett.131.031802.

[25] Simona Ilieva Ilieva. “Measurement of the muon flux at SND@LHC”. In: (2023). URL: http://cds.cern.ch/record/2859193.

[26] D Abbaneo et al. “Results and Perspectives from the First Two Years of Neutrino Physics at the LHC by the SND@ LHC Experiment”. In: *Symmetry* (2024). DOI: https://doi.org/10.3390/sym1010000.